

**Characterizing and Modelling the Strain Rate-Dependent
Constitutive Response of a Unidirectional Non-Crimp Fabric
Composite Material**

by
Khizar Rouf

A thesis
presented to the University of Waterloo
in fulfilment of the
thesis requirement for the degree of
Doctor of Philosophy
in
Mechanical and Mechatronics Engineering

Waterloo, Ontario, Canada, 2023

© Khizar Rouf 2023

Examining Committee Membership

The following served on the examining committee for this thesis. The decision of the examining committee is by majority vote.

Supervisor	John Montesano, Ph.D. Associate Professor, University of Waterloo
Co-Supervisor	Michael J. Worswick, Ph.D. Professor, University of Waterloo
External Examiner	Mauricio Vicente Donadon, Ph.D. Professor, Instituto Tecnológico de Aeronáutica
Internal Member	Adrian Gerlich, Ph.D. Professor, University of Waterloo
Internal Member	Kaan Inal, Ph.D. Professor, University of Waterloo
Internal-external Member	Daniel Lacroix, Ph.D. Assistant Professor, University of Waterloo

Author's Declaration

This thesis consists of material all of which I authored or co-authored (see Statement of Contributions included in the thesis). This is a true copy of the thesis, including any required final revisions, as accepted by my examiners. I understand that my thesis may be made electronically available to the public.

Statement of Contributions

I would like to acknowledge my co-authors who contributed to this thesis.

Professor John Montesano: Supervision, Funding acquisition, Conceptualization, Review, Editing Resources and Project administration.

Professor Michael Worswick: Supervision, Funding acquisition, Conceptualization, Review, Editing Resources and Project administration.

Professor Jeff Wood: Appendix A – Conceptualization, Review, and Editing.

Jose Imbert-Boyd: Appendix A & B – Guidance for experimental work, Appendix A – Review and Editing

Aaditya Suratkar: Appendix A – Original Draft and Experimental work (Sections 2.2 and 2.4).

The balance of the research work is my own work.

Abstract

Liquid molded composite materials comprising heavy-tow non-crimp fabric reinforcements are increasingly being used for primary load-bearing structures in the automotive sector due to their excellent specific mechanical properties, high anisotropic tailorability, and comparatively lower cost in contrast to the other fabric reinforced composite material systems. Automotive structures may be subject to impact loads during their service life; therefore, a thorough comprehension of the constitutive behavior of non-crimp fabric composites at different strain rates is required. This study focuses on characterizing the strain rate-dependent deformation response of a unidirectional non-crimp fabric (UD-NCF) composite, comprising PX35 UD-300 carbon fiber fabric and TRAC 06150 snap cure epoxy, through physical and virtual experiments. A constitutive model is also developed and implemented for predicting the strain rate-dependent pre-peak deformation response of the same material system.

The anisotropic strain rate-dependent deformation and failure response of the UD-NCF carbon fiber/snap-cure epoxy composite was characterized through physical experiments, including transverse tension, transverse compression, longitudinal compression, and in-plane shear. Hydraulic testing machines were used for performing quasi-static and intermediate strain rate tests, while tensile and compressive split Hopkinson bar apparatuses were used for the high strain rate tests. The stress-strain response for the in-plane shear and transverse compression modes was initially linear, followed by a nonlinear response at all strain rates. The yield stress and ultimate strength for the transverse compression mode were found to increase by 54% and 50%, respectively, with an increase in strain rate from 0.003 s^{-1} to 260 s^{-1} . For the in-plane shear mode, the yield stress and ultimate strength were found to increase by 60% and 61%, respectively, with an increase in axial strain rate from 0.003 s^{-1} to 315 s^{-1} . The stress-strain response for the longitudinal compression and transverse tension modes was approximately linear until failure. The longitudinal compression strength increased by 35% with an increase in strain rate from 0.001 s^{-1} to 70 s^{-1} . Inter-tow splitting, delamination, and localized fiber kinking was observed on the corresponding failure surface, which is distinct from that typically observed in UD tape composites. The transverse tensile strength increased by 20% with an increase in strain rate from 0.1 s^{-1} to 126 s^{-1} , with the fracture surface revealing pull-out of supporting glass fibers and local matrix plastic deformation.

A dual-scale computational modelling framework was developed for predicting the strain rate-dependent nonlinear deformation response of the UD-NCF composite. For the micro-scale finite element model, the elastic-plastic response of the epoxy was captured using the linear Drucker-Prager model, while the carbon fibers were treated as linear elastic and transversely isotropic. For the mesoscale finite element model, Hill's anisotropic yield function was used for modelling the effective elastic-plastic response of the impregnated tow. The Johnson-Cook model was used to capture the strain rate dependency of the epoxy

and impregnated tow. The predicted and experimentally measured stress-strain response at quasi-static strain rates was found to be in good agreement. Slight discrepancies were found between the experimental and predicted stress-strain response at high strain rates at higher applied strains, which may be due to the fact that the existing material models do not consider the viscoelastic material behavior. The in-plane and out-of-plane shear stress-strain responses were found to be strongly dependent on the applied strain rate.

An invariant-based constitutive model was developed and implemented as a user-defined subroutine in the commercial finite element software LS-DYNA to predict the strain rate-dependent elastic-inelastic deformation response of the UD-NCF composite. The model is calibrated using data obtained from the physical and virtual tests and verified for different cases. The model accurately captured the strain rate-dependent elastic and inelastic response. The first step validation of the model is performed for a $[\pm 45]_{2s}$ laminate at quasi-static and high strain rates using a single element. A very good agreement was observed between the predicted and experimental results. The model is also validated with a single element for an IM7-8552 UD tape composite by simulating the axial compression response for 15° , 30° , 45° , 60° , 75° and 90° off-axis laminas at quasi-static and high strain rates. Overall, a good agreement between the predicted and experimental results was observed at both quasi-static and high strain rates.

The main outcomes of this research work include a new dataset for the strain rate-dependent deformation response and fracture behaviour of the UD-NCF carbon fiber/snap-cure epoxy composite material system. In addition, the developed invariant-based constitutive model accurately captures the pre-peak strain rate-dependent deformation response of the UD-NCF composite and will be further developed in future work for use in impact simulations of automotive structures.

Acknowledgements

Above all else, I want to acknowledge God's blessings for granting me abundant opportunities, wisdom, and assistance during my doctoral voyage. Furthermore, I would like to express my profound gratitude to Professor John Montesano, my supervisor, for affording me the captivating opportunity to contribute to this project and for including me in his esteemed research team. Professor Montesano has been an extraordinary guide, offering me invaluable direction, motivation, and unwavering backing throughout this endeavor. I am also appreciative of his understanding regarding my personal commitments and his provision of sufficient time for my recovery following a complex surgery in 2022.

Additionally, I extend my gratitude to my co-supervisor, Professor Michael Worswick, for his unparalleled technical support and for generously providing me with unrestricted access to the state-of-the-art equipment in his laboratory. This access was crucial in developing novel tests and successfully carrying out this research. His profound knowledge and insightful suggestions regarding experimentation, simulations, and writing were of immeasurable value to me. Furthermore, I would like to acknowledge the members of my examining committee, namely Professor Mauricio Vicente Donadon from the Instituto Tecnológico de Aeronáutica (Brazil) as well as Professor Adrian Gerlich, Professor Daniel Lacroix, and Professor Kaan Inal from the University of Waterloo, for their invaluable feedback on my research work.

The execution of the experimental work in this research project would have been impossible without the assistance of the experienced research staff and technicians of the Forming and Crash Lab. I express my gratitude to Dr. Imbert-Boyd, Amir Zhumagulov, Mike Bustamante, Dr. Brock Watson, Tom Gawel, and Eckhard Budziarek for their unparalleled support throughout the experimental phase. A special note of thanks is owed to Dr. Imbert-Boyd for his guidance in operating various testing equipment and for his invaluable assistance in troubleshooting the testing setup. I am also appreciative of Mark Kuntz and the dedicated staff from the Engineering Student Machine Shop for their aid in developing new test fixtures.

I wish to convey my gratitude for the generous financial support provided by several organizations. The Natural Sciences and Engineering Research Council, Honda Research Institute US, Westlake Epoxy, Zoltek Corp., Laval, and Ontario Advanced Manufacturing Consortium have played a crucial role in funding this research, and I am deeply appreciative of their contributions. I am particularly thankful to the Natural Sciences and Engineering Research Council for their additional support through the Alexander Graham Bell Canada Graduate Scholarship. Additionally, I extend my appreciation to the dedicated staff of the Fraunhofer Innovation Platform for Composites Research at Western University for their assistance in manufacturing the composite panels used in the testing phase.

I want to express my heartfelt appreciation to my beloved parents, Abdul Rouf Anjum and Sajida Parveen, whose unwavering support has been a constant source of strength during the most arduous moments of this journey. I am also deeply grateful to my wife, Kiran Aslam, and my son, Keyaan Rouf, for their understanding, encouragement, and sacrifices that allowed me to focus on my research. To my siblings, Yasir Rouf, Sara Anjum, and Farah Anjum, as well as my brother-in-law, Shaukat Javed, I extend my sincere thanks for their continuous support and belief in my abilities.

I would also like to acknowledge the immense support and encouragement I received from my friends and colleagues at the University of Waterloo. Specifically, I am grateful to Ahmed Hanafy, Muhammad Waqas, Pedram Samadian, Yu Zeng, Victor Shi, Aadytia Suratkar and all other group members for their unwavering support, motivation, and invaluable technical discussions throughout this journey. Their camaraderie has been an essential pillar of strength. To all my friends, colleagues, and family members who have stood by me, offering their support and motivation, I am deeply grateful for your presence in my life.

Finally, I want to express my sincere gratitude to Professor Nancy L. Denton for her exceptional support during my previous studies at Purdue University, which marked the true commencement of my research journey. Additionally, I am deeply appreciative of Dr. Wenbin Yu for his extraordinary mentorship and consistent support throughout my career. The invaluable multiscale modeling experience I gained from his group has been an instrumental guiding force for me.

Dedication

“To all of my family.”

Table of Contents

Examining Committee Membership	ii
Author's Declaration	iii
Statement of Contributions	iv
Abstract	v
Acknowledgements	vii
Dedication	ix
List of Figures	xiii
List of Tables	xvii
Chapter 1: Introduction	1
1.1 Research Motivation	1
1.2 Research Proposal Outline	3
Chapter 2: Background and Literature Review	5
2.1 FRP Composite Materials	5
2.2 Manufacturing Processes for FRP Composite Materials	6
2.3 Characterizing the Strain Rate-Dependent Response of FRPs	7
2.3.1 Experimental methods for different strain rates	7
2.3.2 Strain rate dependency for fibers and matrix	9
2.3.3 Strain rate-dependent mechanical response of unidirectional composites	10
2.4 Multiscale Modelling of NCF Composites	15
2.4.1 Introduction to multiscale modelling	15
2.4.2 Review of relevant literature	18
2.5 Macromechanical Response of FRPs	19
2.5.1 Linear elastic response of composite materials	20
2.5.2 Pre-peak response	22

2.5.3	Failure initiation and damage evolution in FRPs-----	24
2.6	Existing Material Models in Commercial FE Software-----	27
Chapter 3: Research Objectives and Scope-----		31
3.1	Research Objectives-----	31
3.2	Scope of Work-----	33
3.2.1	Task 1-----	33
3.2.2	Task 2-----	33
3.2.3	Task 3-----	34
Chapter 4: Research Results-----		35
4.1	Materials and Manufacturing-----	36
4.2	Task 1: Strain Rate-Dependent Constitutive Characterization-----	37
4.2.1	Development of testing protocol-----	37
4.2.2	In-plane shear testing results-----	41
4.2.3	Transverse tensile testing results-----	45
4.2.4	Transverse compression testing results-----	49
4.2.5	Longitudinal compression testing results-----	53
4.3	Task 2: Development of a Validated Computational Multiscale Model-----	57
4.3.1	Multiscale modelling for homogenization and failure initiation-----	57
4.3.2	Multiscale modelling framework for strain rate dependent non-linear homogenization----	58
4.4	Task 3: Development of a Validated Strain Rate-Dependent Constitutive Model-----	68
4.4.1	Theoretical development and implementation of an elasto-plastic deformation model----	68
4.4.2	Material model calibration, verification, and validation for UD-NCF composite-----	72
4.4.3	Material model verification for UD-NCF composite-----	74
4.4.4	Material model verification, and validation for IM7-8552-----	79
Chapter 5: Conclusions and Recommendations-----		82
5.1	Conclusions-----	82

5.2	Recommendations for Future Work	84
5.2.1	Future experimental work	85
5.2.2	Future multiscale modelling work	85
5.2.3	Future constitutive model development	85
	References	87
	Appendix A	107
	Appendix B	108
	Appendix C	109
	Appendix D	110
	Appendix E	111
	Appendix F	112

List of Figures

Figure 1-1: Fuel efficiency targets and historical performance for major auto markets [1].	1
Figure 1-2: An image of the 2022 BMW <i>iX</i> battery-electric sports activity vehicle	2
Figure 2-1: Image of a unidirectional non-crimp fabric comprising carbon fiber tows,	5
Figure 2-2: Flow diagram of a typical HP-RTM process [27].	7
Figure 2-3: (a) Schematic diagram of a conventional tensile split Hopkinson pressure bar apparatus, (b) Incident, transmitted and reflected wave signals for a typical split Hopkinson pressure bar tensile test.	8
Figure 2-4: Stress-strain response of EPIKOTE™ Resin TRAC 06150 epoxy	10
Figure 2-5: Stress-strain plots for UDTCs tested under different strain rates: (a) Transverse tension [49], (b) In-plane shear [35], and (c) Transverse compression [35].	12
Figure 2-6: Images of the failed specimens tested at: (a) quasi-static strain rate [17], and (b) high strain rate [17]. (c) Stress-strain response for specimens tested in longitudinal compression at quasi-static and high rates [17].	14
Figure 2-7: Flowchart for a hierarchical multiscale modelling approach	17
Figure 2-8: (a) Generalized stress-strain response of an FRP lamina (showing different stages of deformation), (b) An image showing a UD lamina with material axis [122].	20
Figure 2-9: Intralaminar failure modes in unidirectional composites: (a) Fiber tensile mode, (b) Fiber compression mode, (c) In-plane shear mode, (d) Matrix tensile mode, (e) Matrix compression mode, (f) Out-of-plane shear mode.	25
Figure 2-10: An illustration of homogenization of damage [143].	26
Figure 3-1: Schematic showing the proposed research plan.	33
Figure 4-1: Schematics of test specimens with dimensions: (a) Transverse tension, (b) Compression	36
Figure 4-2: (a) Schematic of a compression SHPB showing a pulse shaper at the end of the incident bar, (b) Comparison of an incident bar pulse with and without a copper pulse shaper (without specimen), (c) Comparison of the incident and transmitted bar forces with pulse shaper, (d) Strain-time evolution during a high strain rate transverse compression test.	39
Figure 4-3: Stress–strain response for transverse compression tests, performed at high rate	40
Figure 4-4: (a) Schematic of a tensile SHPB showing a pulse shaper on the incident bar, (b) Comparison of incident bar pulse with and without a lead-tin pulse shaper, (c) Comparison of the incident and transmitted bar forces with pulse shaper.	41
Figure 4-5: Stress-strain plots for in-plane shear tests at strain rates of: (a) 0.003 s^{-1} , (b) 1.8 s^{-1} , and (c) 315 s^{-1} . (d) Average stress-strain plots for indicated strain rates with standard error bars.	43

Figure 4-6: Average in-plane shear properties of the UD-NCF composite for indicated strain rates: (a) Modulus, (b) Yield stress, (c) Ultimate strength.....	44
Figure 4-7: Average in-plane shear yield stress, strength and modulus versus strain rate.....	44
Figure 4-8: (a) An image showing axial strain distribution during a high rate shear test on the C-SHPB, (b) A microscopic image of the failed in-plane shear specimen tested at high strain rate.	45
Figure 4-9: Stress-strain plots for transverse tensile tests performed at applied strain rates of: (a) 0.1 s^{-1} , (b) 16 s^{-1} , and (c) 126 s^{-1} . (d) Average stress-strain plots for indicated strain rates with standard error bars. .	46
Figure 4-10: Average in-plane transverse tensile strength of the UD-NCF composite	47
Figure 4-11: Average transverse tensile strength versus strain rate	48
Figure 4-12: Images of failed transverse tension specimens.....	48
Figure 4-13: Fracture surface images of a transverse tension specimen (taken with a scanning electron microscope): 100x magnification (left) and 500x magnification (right).	49
Figure 4-14: Stress-strain plots for transverse compression tests at strain rates: (a) 0.003 s^{-1} , (b) 1.2 s^{-1} , and (c) 260 s^{-1} . (d) Average stress-strain plots for indicated strain rates with standard error bars.	50
Figure 4-15: Average in-plane transverse compression properties of the UD-NCF composite for indicated strain rates (a) Modulus, (b) Yield stress, (c) Ultimate compression strength.	50
Figure 4-16: Average transverse compression strength, yield stress, and modulus	51
Figure 4-17: Images of failed transverse compression specimens	52
Figure 4-18: Fracture surface images of transverse compression specimens at strain rates: (a) 0.003 s^{-1} ; (b) 1.2 s^{-1} ; (c) 260 s^{-1}	52
Figure 4-19: Fracture surface images of a transverse compression specimen (taken with a scanning electron microscope) showing different failure modes.	53
Figure 4-20: Fixture for the longitudinal compression testing.....	54
Figure 4-21: Stress-strain plots for longitudinal compression tests performed at strain rates: (a) 0.001 s^{-1} , (b) 0.07 s^{-1} , and (c) 70 s^{-1} . (d) Average stress-strain plots for indicated strain rates with standard error bars.	55
Figure 4-22: Average longitudinal compression strength of the UD-NCF composite	56
Figure 4-23: Average longitudinal compression strength vs strain rate	56
Figure 4-24: Image showing (a) A failed specimen (1-fiber direction, 3-through the thickness transverse direction), (b) Edge view of a failed specimen having inclined fracture surface and delamination, (c) A failed specimen having inter-tow splitting (2-in-plane transverse direction).....	57
Figure 4-25: (a) Cross-sectional view of the tows of the UD-NCF composite [29], (b) magnified view of a tow showing fibers [29], (c) 3D RVE model for tows (microscale).....	58
Figure 4-26: (a) Cross-sectional view of the tows of the NCF composite, (b) 3D RVE	59

Figure 4-27: Predicted effective stress-strain response of the UD impregnated tow under a quasi-static strain rate (0.0001 s^{-1}) using microscale RVEs: (a) longitudinal tension, (b) transverse tension, (c) in-plane shear, and (d) out-of-plane shear.....	61
Figure 4-28: Longitudinal tensile response of the UD-NCF composite at quasi-static strain rate: (a) Experimentally measured [25] and predicted stress-strain plot, (b) Contour plot showing plastic strain component for applied strain of 1.2% along the longitudinal direction.....	63
Figure 4-29: Transverse tensile response of the UD-NCF composite at quasi-static strain rate: (a) Experimentally measured [2] and predicted stress-strain plot, (b) Contour plot showing plastic strain component for applied strain of 0.7% along the transverse direction.....	63
Figure 4-30: In-plane shear response of the UD-NCF composite at quasi-static strain rate: (a) Experimentally measured [2] and predicted stress-strain plot, (b) Contour plot showing plastic strain component for applied strain of 5% in the in-plane shear direction.....	64
Figure 4-31: Out-of-plane shear response of the UD-NCF composite at quasi-static strain rate: (a) Predicted stress-strain plot, (b) Contour plot showing plastic strain component for applied strain of 5% in the out-of-plane shear direction.....	64
Figure 4-32: Comparison of the in-plane and out-of-plane shear response obtained	65
Figure 4-33: Predicted effective in-plane shear stress-strain response for UD-NCF composite.....	66
Figure 4-34: Contour plots showing in-plane shear plastic strain component for applied shear strain of 5% at strain rates of: (a) 0.0003 s^{-1} , (b) 1 s^{-1} , (c) 50 s^{-1} and (d) 550 s^{-1}	66
Figure 4-35: Predicted effective out-of-plane shear stress-strain response of UD-NCF composite.....	67
Figure 4-36: Contour plots showing out-of-plane plastic strain component for applied shear strain of 5% at strain rates of: (a) 0.0003 s^{-1} , (b) 1 s^{-1} , (c) 50 s^{-1} , and (d) 550 s^{-1}	67
Figure 4-37: Comparison of the predicted and experimentally measured [29].....	68
Figure 4-38: Schematic stress-strain plot demonstrating the additive split of strain (ε^i , ε^e and ε^f represent the inelastic, elastic and fracture strains, respectively) and the influence of strain rate.....	69
Figure 4-39: Flowchart of VUMAT Subroutine	72
Figure 4-40: Hardening curves for: (a) In-plane shear, (b) Transverse compression.	74
Figure 4-41: Boundary conditions for the single element tests: (a) Transverse tension, (b) Transverse compression (1 represents the fiber direction).	75
Figure 4-42: Comparison of the single element and experiment [194] test results for the transverse tension mode at strain rate of: (a) 0.1 s^{-1} , (b) 16 s^{-1} and (c) 126 s^{-1}	75
Figure 4-43: Comparison of the single element and experiment [194] test results for the transverse compression mode at strain rate of: (a) 0.003 s^{-1} , (b) 1.4 s^{-1} and (c) 260 s^{-1}	75
Figure 4-44: Boundary conditions for the single element tests.....	76

Figure 4-45: Comparison of the single element and experiment [194] test results for the in-plane shear mode at strain rate of: (a) 0.003 s^{-1} , (b) 1.8 s^{-1} and (c) 315 s^{-1}	76
Figure 4-46: Comparison of the single element and scaled experiment [194] test results for the out-of-plane shear mode at strain rate of 0.003 s^{-1}	77
Figure 4-47: Boundary conditions for the single element tests: (a) Longitudinal tension, (b) Longitudinal compression (1 represents the fiber direction).	77
Figure 4-48: Comparison of the single element and experiment [171] test results at 0.001 s^{-1} strain rate for: (a) Longitudinal tension, (b) Longitudinal compression.	78
Figure 4-49: Boundary conditions for the single element tests for the first stage validation.	78
Figure 4-50: Transient velocity curve used for the simulations at high strain rates.	79
Figure 4-51: Comparison of the predicted and experiment test results for $[\pm 45]_2$ s laminate at the: (a) 0.003 s^{-1} , (b) 315 s^{-1}	79
Figure 4-52: Material model verification results for IM7-8552 composite: (a) In-plane shear, (b) Transverse shear, (c) Transverse compression (experimental data was taken from [125]).	80
Figure 4-53: Stress-strain plots showing predicted and experimental results [41] at quasi-static and high strain rate for: (a) 15 degree, (b) 30 degree, (c) 45 degree, (d) 60 degree, (e) 75 degree and (f) 90 degree off-axis laminas	81

List of Tables

Table 3-1: Objectives, gaps, and tasks for the proposed research work	32
Table 4-1: Nominal gauge dimensions and lay-up sequence of specimens used for different tests.	37
Table 4-2: Carbon fiber properties [177, 178].....	59
Table 4-3: Matrix mechanical properties and coefficients [23].....	59
Table 4-4: Yield stress, taken at zero plastic strain, for the homogenized tows.....	62
Table 4-5: Yield stress ratio based on the experimental data (inputs for Hill’s anisotropic yield model) .	62
Table 4-6: Johnson-Cook model parameters for tow.....	62
Table 4-7: Input parameters for the material model for UD-NCF composite material.....	73

Chapter 1: Introduction

1.1 Research Motivation

Rising demands for reduction of CO₂ emissions from the combustion of fossil fuels in the transportation sector to meet strict legislated fuel efficiency targets have put automakers under tremendous pressure in the major global auto-markets (**Figure 1-1**) [1, 2]. Such targets can be achieved by reducing aerodynamic drag, improving powertrain efficiency, and reducing the mass of vehicles [3]. Reducing the body-in-white (BIW) mass is one of the most effective ways to reduce vehicle fuel consumption and achieve high fuel efficiency targets [4]. For example, a 10% decrease in the mass of a vehicle can reduce fuel consumption by 6-8% without affecting its performance [4]. In addition, low-mass BIW structures will enable future long-range battery electric and hydrogen fuel cell vehicles. Based on a study by Joost [4], the driving distance of an electric vehicle (EV) can be increased by 13.7% without increasing its battery capacity if its weight is reduced by 10%.

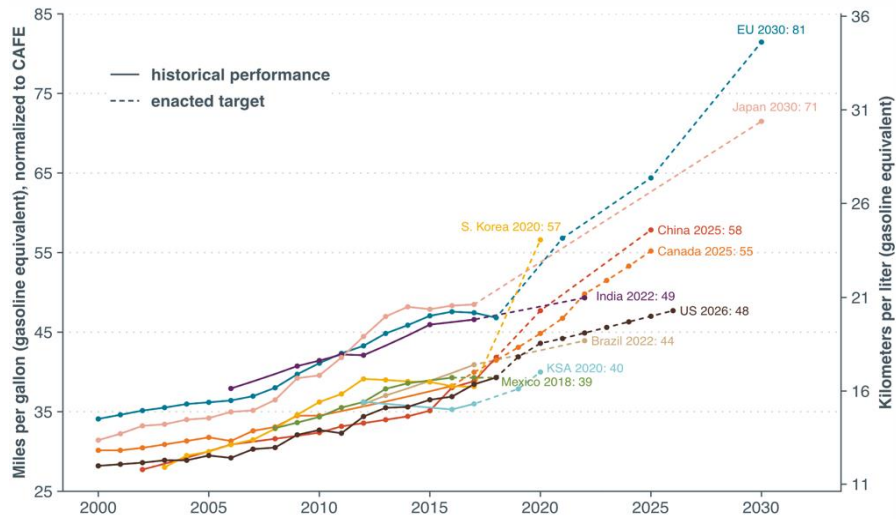


Figure 1-1: Fuel efficiency targets and historical performance for major auto markets [1].

To reduce the BIW mass of current vehicles, car manufacturers have replaced load-bearing metallic structures with structures manufactured from lightweight materials such as fiber reinforced plastic (FRP) composites. FRPs exhibit high specific stiffness and strength as well as excellent specific energy absorption

characteristics, which is important for the crashworthiness and safety of vehicles [5]. However, the use of FRPs has been limited to luxury or so-called supercars, such as the BMW iX battery-electric sports vehicle (**Figure 1-2**) [6] and the Porsche GT4 race car [7], for which high production costs and long cycle times can be tolerated. The full potential for FRPs is not currently being realized for high-volume production vehicles. The recent development of new rapid curing resins, low-cost carbon fiber non-crimp fabrics (NCFs), and automated liquid composite molding processes, such as high-pressure resin transfer molding (HP-RTM), have reduced the production cost as well as the cycle times of FRP composite components from hours to minutes [8]. Ultimately, the advancements in liquid composite molding processing technology may enable the use of NCF carbon fiber/snap-cure epoxy composites in the BIW energy absorbing structures of high-volume production light duty vehicles (LDVs) for which strict crashworthiness requirements must be met.

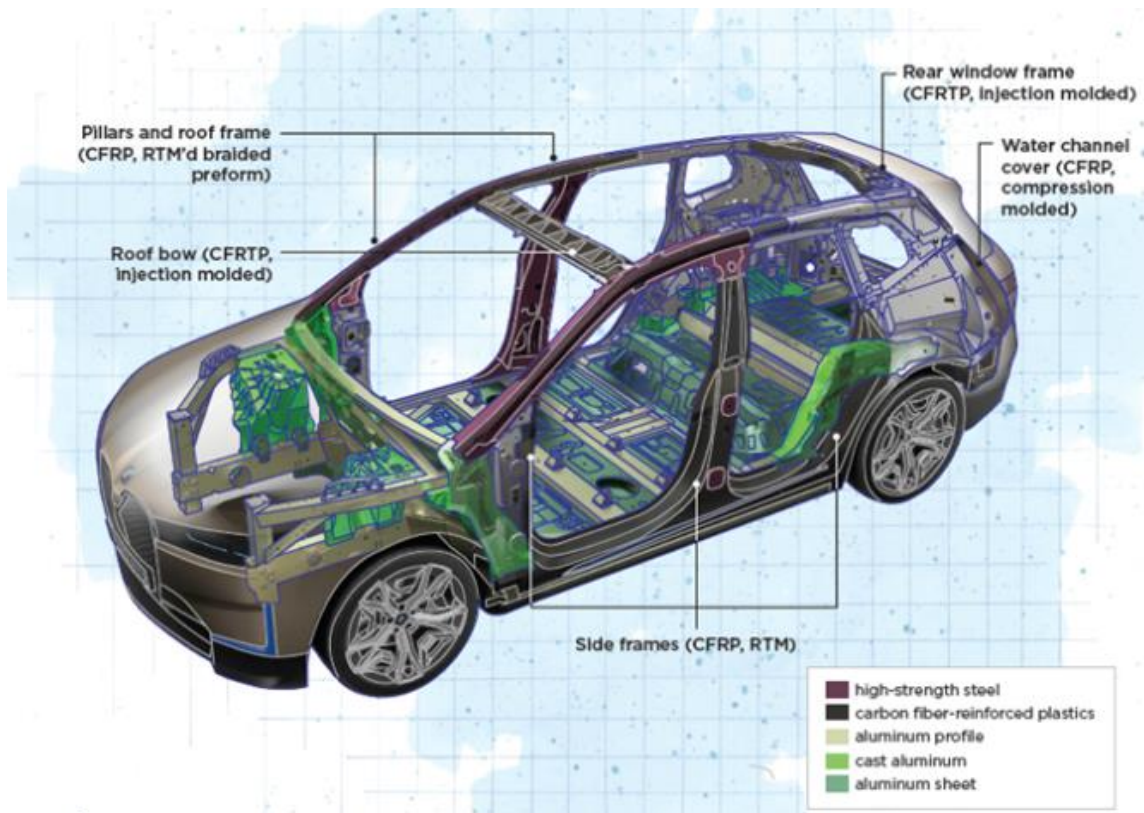


Figure 1-2: An image of the 2022 BMW *iX* battery-electric sports activity vehicle Highlighting parts made from FRPs [6].

Vehicle crashworthiness is typically assessed through full-scale virtual structural analysis followed by crash testing. Virtual structural analysis is a cost-effective and efficient approach to predict the impact performance of structures and is necessary to significantly reduce product development cost and time [5]. Computer-aided engineering (CAE) impact simulation models are developed to simulate a crash event and predict the energy absorption capabilities of a vehicle structure. The accurate prediction of vehicle impact performance ultimately requires calibrated high-fidelity constitutive models. The existing constitutive models for FRP composites are not robust and have limitations that affect their predictive capabilities [8, 9, 10]. The anisotropic response and heterogeneous nature of FRPs results in complex failure processes that involves multiple damage mechanisms, such as fiber rupture, fiber kinking, matrix cracking and delamination [11, 12], which are challenging to capture. As a result, most of the existing constitutive material models used in CAE impact simulations employ non-physical parameters that require a significant effort to calibrate [5]. Some attempts have been made to develop physically-based constitutive material models to reduce the number of non-physical parameters [13]; however, these models often under-predict the structural response [8, 14] since strain rate effects and/or pre-peak softening (inelastic response before failure due to matrix cracking and/or matrix yielding) are not considered. Modelling the strain rate-dependent response of FRP materials requires calibration of the material properties at different strain rates. Previous studies were primarily focused on characterizing the strain rate-dependent response of unidirectional tape composites (UDTCs) [15, 16], and it was reported that varying degrees of strain rate dependency occur in different modes (*e.g.* longitudinal compression, longitudinal tension, transverse tension, transverse compression, in-plane shear, and out-of-plane shear). Conflicting results were also reported for some modes such as for the longitudinal compression mode. Some studies reported a significant increase in the longitudinal compression strength with an increase in strain rate [17], while others reported a negligible change [18]. Moreover, the strain rate-dependent deformation response of NCF composites has not yet been studied for all modes. Owing to their distinct microstructure when compared to UDTCs, the strain rate-dependent response of unidirectional (UD) NCF composites may also be distinct. Therefore, there is a need to characterize and model the strain rate-dependent constitutive response of UD-NCF composites for use in CAE impact simulation models of corresponding structures.

1.2 Research Proposal Outline

This PhD dissertation is written using a manuscript-based format, comprising this synopsis with a number of appended publications. Chapter 2 presents relevant background and a review of the literature pertaining to the strain rate-dependent response, multiscale modelling, and the constitutive modelling of composites. The main objectives and scope of the dissertation are described in Chapter 3. Chapter 4 provides a summary of the main results of the research work performed during the PhD degree. Conclusions

and recommendations for the future work are outlined in Chapter 5. The remainder of the dissertation comprises five appendices, each of which includes a published or submitted peer-reviewed research article that serve to detail the research results.

Chapter 2: Background and Literature Review

2.1 FRP Composite Materials

High performance FRPs are mainly composed of high-strength continuous fibers embedded in a polymer matrix. The most widely used are carbon, glass and aramid fibers. Polymer matrices used in FRPs are generally divided into two broad categories: thermosets and thermoplastics. In FRPs, fibers act as a reinforcement and provide stiffness and strength, while the polymer matrix maintains the position and orientation of the fibers and allows for load transfer through the fiber/matrix interface [19]. The stiffness and strength of continuous FRPs highly depend on the fiber orientation; therefore, individual plies (laminae) are often stacked with different orientations to tailor their anisotropic stiffness and strength properties. A multidirectional stack of plies is termed as a “laminate”. There are several types of continuous FRPs used in practice, including UDTC, UD-NCF composites, two dimensional (2D) woven or braided fabric composites, and three dimensional (3D) fabric composites.

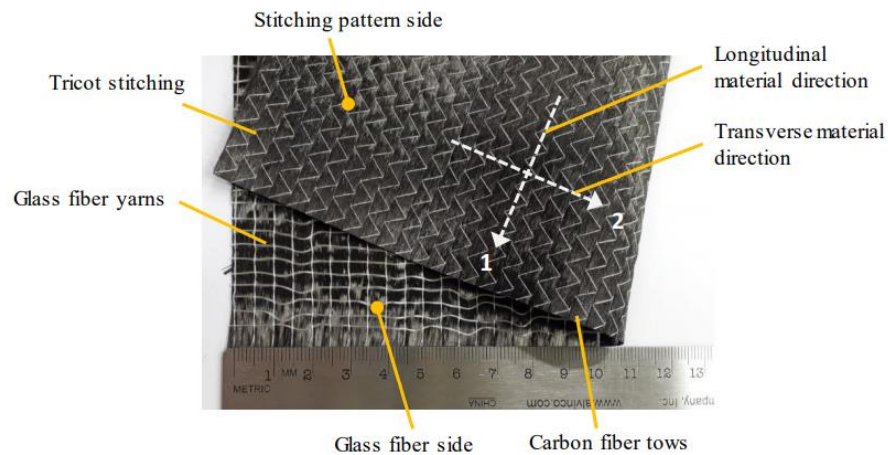


Figure 2-1: Image of a unidirectional non-crimp fabric comprising carbon fiber tows, supporting glass fiber yarns and polyester stitching as indicated [20].

UD-NCF composites typically comprise a UD-NCF reinforcement and a thermosetting matrix. UD-NCF reinforcements contain a single layer of evenly spaced aligned fiber tows, which are supported by low density glass fiber yarns in the transverse direction (**Figure 2-1**) and stitched with one another using a polyester thread with a prescribed stitching pattern (*e.g.* pillar, cord, satin and tricot). The presence of stitches causes local in-plane fiber tow misalignment, which can negatively influence the in-plane

mechanical properties of UD-NCF composites [21]. The mechanical properties of UD-NCF composites also depend on the stitching pattern [22]. Moreover, snap-cure epoxy systems that consist of a highly reactive thermosetting epoxy resin and a curing agent (hardener) with catalysts or accelerators are often used to achieve fast curing cycles under high temperatures [23, 24]. Snap-cure epoxy systems have low viscosity when compared to standard epoxies, which allows faster impregnation of the preform. Generally, fast-curing epoxy tends to have lower glass transition temperature when compared to typical epoxies, which may limit the service temperature of associated FRP composite components [25].

2.2 Manufacturing Processes for FRP Composite Materials

Several manufacturing processes have been developed for continuous FRP components, which can be classified based on the type of mold, namely open molding processes (*e.g.* prepreg lay-up by hand or automated ply placement, wet lay-up and filament winding) and closed molding processes (*e.g.* resin transfer molding, compression molding, vacuum infusion, and pultrusion) [26]. Most processes produce parts that have quality issues and/or shape limitations. For instance, the wet lay-up process produces parts that may have non-uniform thickness, dry spots and excessive voids, while the pultrusion process produces straight parts that are limited to having a constant cross-section. A common limitation associated with most open and closed mold processes is long production times. The development of rapid curing resins and automation has led to variations of these processes that provide notably reduced cycle times. Recently, the HP-RTM process (**Figure 2-2**) has gained notable attention in the automotive industry since high quality parts with complex geometries can be manufactured at significantly higher production rates by rapidly injecting snap-curing resin at high pressures into a closed mold containing a fiber preform [27]. The HP-RTM process is considered a suitable manufacturing method for the automotive industry since it provides a balance between cost, quality, and cycle time [28, 29]. As a result of automation and rapid production, manufacturing-induced defects may manifest in FRP composite materials. Typical defects observed in NCF composites fabricated from the HP-RTM process include variation in the fiber dispersion within the tows, variation in the relative position and shape of the tows, slight out-of-plane tow crimping, non-uniform part thickness, micro-void formation, and dry spots [28, 30]. The presence of tow misalignment and crimp may reduce the stiffness and strength of UD-NCF composites, depending on the type of stitch [31, 32]. A decrease of up to 20% in longitudinal stiffness and 36% in longitudinal strength have been reported in the previous studies [31, 32, 33]. The presence of voids and dry spots also affect the mechanical properties of the NCF composites [30]. An increase of 0.5% void content can reduce the flexural strength by 8% [30]. Voids content in parts manufactured with HP-RTM process can be as low as in parts manufactured with prepregs in an autoclave ($< 0.05\%$); however, the size and percentage of the void contents highly depend on the processing parameters [34].

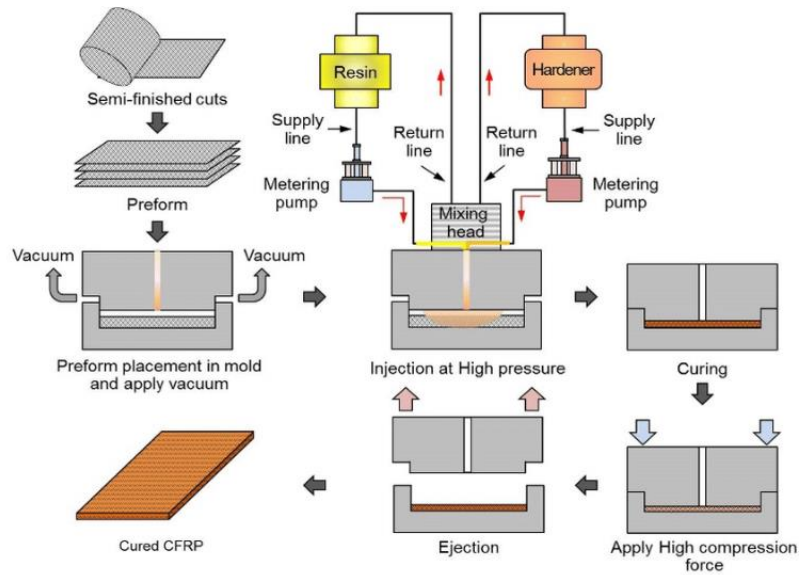


Figure 2-2: Flow diagram of a typical HP-RTM process [27].

2.3 Characterizing the Strain Rate-Dependent Response of FRPs

The strain rate-dependent mechanical response of continuous FRPs has been investigated by several research groups [11, 18, 35, 36, 37, 38, 39, 40, 41, 42]. The degree of strain rate dependency is distinct for different deformation modes and is influenced by the properties of the constituents as well as the FRP material microstructure [43, 44]. The following sections will review studies that have characterized the strain rate-dependent behavior of UD-NCF composites and UDTCs since they both comprise unidirectional fibers.

2.3.1 Experimental methods for different strain rates

The most widely used testing equipment to characterize the strain rate-dependent behavior of materials includes hydraulic testing machines, drop towers, and split Hopkinson pressure bar (SHPB) apparatus. Uniaxial hydraulic testing machines with standard or custom grips are commonly used to test FRP composites under quasi-static and intermediate strain rates, in both tension and compression. Commercially available hydraulic machines are used to test specimens under quasi-static strain rates ($< 0.1 \text{ s}^{-1}$), while specialized hydraulic machines are used for testing materials at intermediate strain rates ($\sim 0.1 \text{ s}^{-1}$ to 100 s^{-1}). In hydraulic machines, the load is typically measured directly using a load cell, while the strains are obtained through extensometers, strain gauges or optical methods.

Drop towers have also been used for testing FRP composites up to strain rates of 1000 s^{-1} [45, 46]. A typical drop tower test comprises dropping a rigid body of known mass from a known distance onto the

specimen. The force is measured using an accelerometer attached to the dropping body, while the strains are measured using optical methods or strain gauges [47]. The impact of inertial mass and contact conditions are primary concerns when it comes to drop towers, as they can potentially influence the results.

SHPBs are commonly used to test FRPs at high strain rates (100 s^{-1} to $10,000 \text{ s}^{-1}$) in tension and compression [48, 49]. One important advantage of SHPBs over other dynamic testing machines is that the strain rate is nearly constant for the duration of the test [50]. A typical SHPB apparatus consists of an incident bar, a transmitted bar and a striker bar (**Figure 2-3a**) [51]. The striker bar is typically accelerated by a gas gun to impact the incident bar, which generates a rectangular pulse or elastic wave that travels along the incident bar until it reaches the specimen. Part of the incident pulse is reflected back due to the impedance mismatch between the specimen and incident bar, while the other part of the pulse is transmitted to the transmitted bar (**Figure 2-3b**). The amplitudes of the incident/reflected waves and transmitted waves are measured by the strain gauges installed on the incident and transmitted bars, respectively.

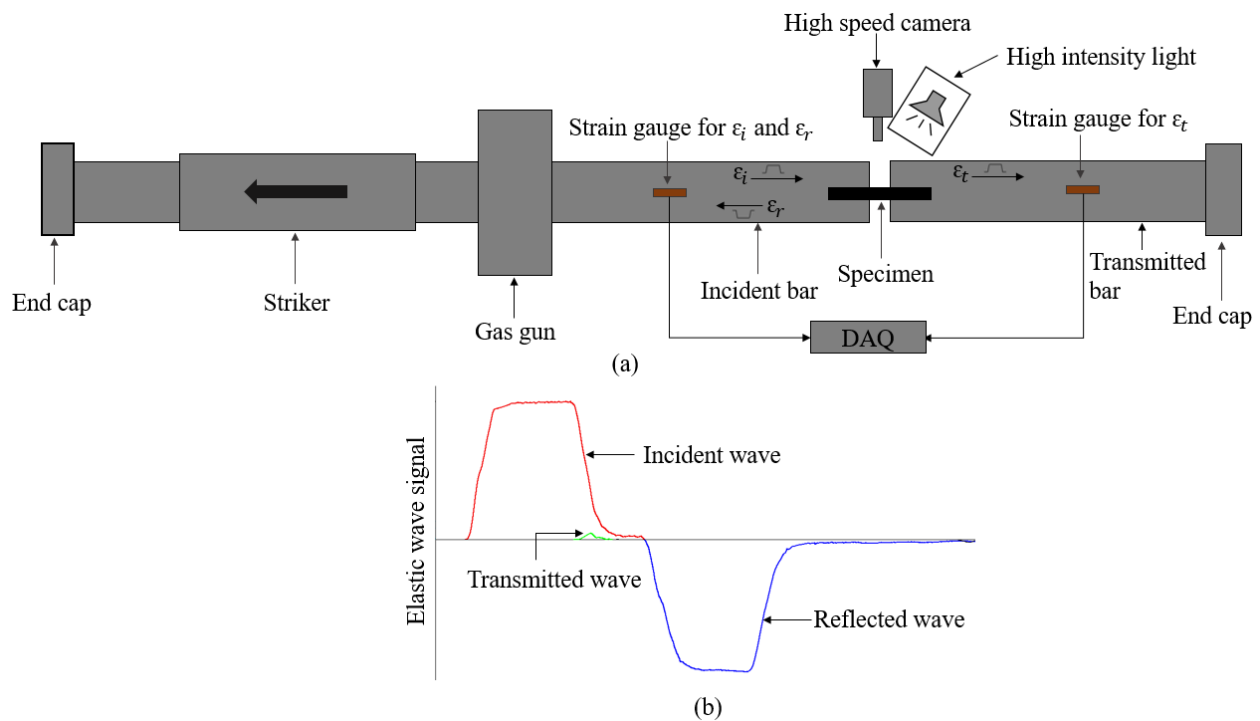


Figure 2-3: (a) Schematic diagram of a conventional tensile split Hopkinson pressure bar apparatus, (b) Incident, transmitted and reflected wave signals for a typical split Hopkinson pressure bar tensile test.

The stress, strain, and strain rate exhibited by the specimen during a high strain rate test on a SHPB apparatus are obtained by analyzing the recorded incident, reflected and transmitted waves and using one dimensional (1D) wave propagation theory [15, 52]:

$$\varepsilon_s = -\frac{2*c}{l_s} \int_0^t \varepsilon_R dt \quad (1)$$

$$\dot{\varepsilon}_s = -\frac{2*c}{l_s} \varepsilon_R(t) \quad (2)$$

$$\sigma_s = E \left(\frac{A_b}{A_s} \right) * \varepsilon_T \quad (3)$$

Here, ε_s , $\dot{\varepsilon}_s$, σ_s , ε_R , ε_T , E , A_b , A_s , c , and l_s represent the specimen strain, specimen strain rate, specimen stress, reflected strain in the incident bar, transmitted strain in the transmitted bar, elastic modulus of the transmitted bar, cross-sectional area of the transmitted bar, cross-sectional area of the specimen, bar wave velocity, and specimen length, respectively. In 1D wave propagation theory, it is assumed that an elastic wave propagates along one direction only, and the amplitudes are negligible in the other directions.

There are two main requirements when performing tests at high strain rates using a SHPB, namely attaining dynamic force equilibrium and a constant strain rate for the duration of the test. Achieving dynamic equilibrium ensures that the specimen uniaxial deformation is homogenous along the specimen length, which can be confirmed by comparing the forces at the incident and transmitted bar ends. For materials having low strain-to-failure, such as continuous fiber-reinforced composites, the conventional SHPB set up is not suitable because it produces a rectangular pulse with a sharp rise time causing specimens to fail during the rise time. Therefore, the input pulse is often changed to produce a ramp shaped pulse with a longer rise time, which aids in achieving dynamic equilibrium [53] and measuring the complete stress-strain response at nearly constant strain rate. This is important for the FRPs which exhibit viscoelastic and viscoplastic response [15]. Some researchers [41, 37, 54, 55] have applied the pulse shaping technique by using sacrificial specimens of different materials such as copper, cardboard, rubber and plastics in their tests to achieve the dynamic equilibrium. These sacrificial specimens are placed between the striker and incident bars and deformed plastically upon impact; therefore, they cannot be reused. Gerlach *et al.* [56] developed a new method to change the shape of the input pulse by introducing a rod of different cross-sections in the incident bar that interferes with the mechanical impedance and increases the rise time of the input pulse.

2.3.2 Strain rate dependency for fibers and matrix

Carbon fibers have high stiffness and strength and low strain-to-failure; thus, they exhibit little to no strain rate dependency [57]. Few studies have been performed to characterize the strain rate-dependent response of carbon fibers. Zhou *et al.* [57] tested T700 carbon fiber bundles at strain rates of 0.001 s^{-1} , 100 s^{-1} and 1300 s^{-1} in tension, and reported that the tensile modulus, strength and strain to failure were insensitive to the strain rate. Ou *et al.* [58] studied the effect of strain rate on the tensile properties of T300 carbon fiber bundles at four strain rates in the range 40 s^{-1} - 160 s^{-1} . The strain-to-failure and elastic modulus

were reported to be rate insensitive. A slight increase in the average strength was observed; however, most results were within the scatter. Note, the strain rate sensitivity of other reinforcement fibers has also been studied in previous work; however, these studies are not discussed here since the present study is focused on FRP composites comprising carbon fibers.

Epoxy resins are a class of glassy amorphous polymers that have relatively low stiffness and strength when compared to carbon fibers, while exhibiting some degree of ductility. Epoxy resins exhibit pronounced strain rate dependency in their tensile, compressive and shear response [23, 49, 59, 60]. Gilat *et al.* [49] characterized the strain rate-dependent behavior of Cyctec Fiberite 977-2 epoxy resin in tension for strain rates up to 400 s^{-1} . The tensile modulus and strength were found to increase with an increase in strain rate, while the strain-to-failure was found to decrease. A similar strain rate-dependent response for the other epoxy systems (*i.e.* E-862, PR-520, Hexcel RTM-6) was observed in the other studies [60, 38]. Recently, Zeng [23] characterized the strain rate-dependent tension and compression deformation response of the same snap-cure epoxy resin considered in this study. A significant increase in the ultimate tensile strength and a slight increase in the elastic modulus were observed with an increase in strain rate, while the strain-to-failure was found to decrease (**Figure 2-4a**). The compressive yield stress was also found to increase significantly with an increase in strain rate; however, the initial compressive modulus was reported to be rate independent (**Figure 2-4b**).

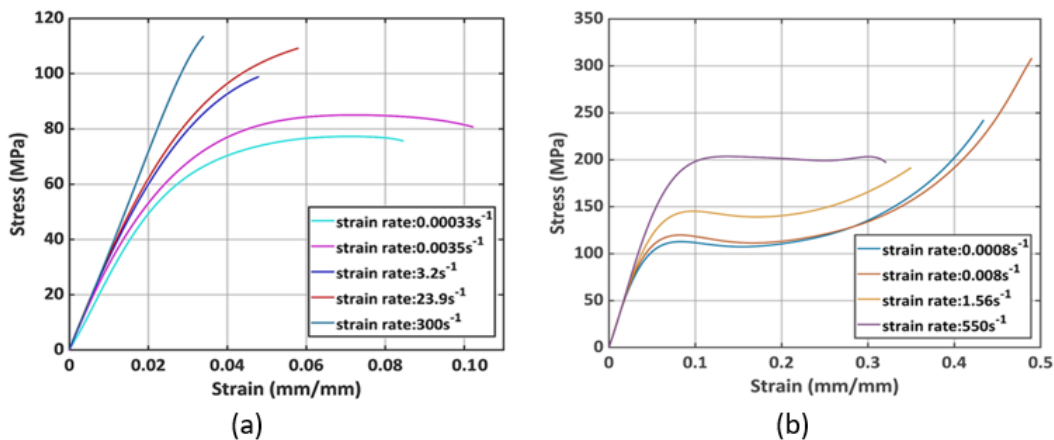


Figure 2-4: Stress-strain response of EPIKOTE™ Resin TRAC 06150 epoxy at various strain rates: (a) Tension, (b) Compression [23].

2.3.3 Strain rate-dependent mechanical response of unidirectional composites

Due to their anisotropic nature, the mechanical response of UD composites is distinct for different modes of deformation, including longitudinal tension and compression (*i.e.* along the fibers), transverse

tension and compression (*i.e.* along the direction transverse to the fibers), and in-plane shear. A literature review of the strain rate dependent response for each mode of deformation is provided in the following paragraphs.

Harding and Welsh [61] studied the effect of strain rate on the longitudinal tensile properties of HYFIL-Torayca-130-S/R7H UDTC using a tensile SHPB apparatus for strain rates up to 400 s^{-1} . The longitudinal tensile modulus and strength were reported to be rate independent. Taniguchi *et al.* [48] studied the strain rate-dependent behavior of a UDTC fabricated from T700S/2500 prepreg using a tensile SHPB for strain rates up to 11 s^{-1} . The effect of strain rate on the longitudinal tensile stress-strain response was reported to be negligible. Ou *et al.* [58] characterized the strain rate-dependent response of a UD-NCF composite, namely T300/JN-C3P, using a servo-hydraulic testing machine. The tensile strength was reported to increase by less than 10% with an increase in strain rate from 25 s^{-1} to 200 s^{-1} . Note that, since the in-plane longitudinal tensile response of unidirectional composites is dominated by the properties of the fibers, the findings reported above were expected.

Melin and Asp [40] characterized the in-plane transverse tensile response of a high performance HTA/6376C UDTC for strain rates up to 800 s^{-1} . A hand driven loading frame and a tensile SHPB apparatus were used for the quasi-static and high strain rate tests, respectively. The transverse modulus was reported to be strain rate independent, while the transverse tensile strength and strain-to-failure were found to increase by 36% and 37%, respectively when the strain rate was increased from 10^{-3} s^{-1} to 800 s^{-1} . Gilat *et al.* [49] tested IM7/977-2 UDTC in the transverse tension at strain rates up to 400 s^{-1} . The transverse strength was reported to increase approximately 21% with an increase in the strain rate from 10^{-5} s^{-1} to 400 s^{-1} (**Figure 2-5a**). Taniguchi *et al.* [48] characterized the strain rate-dependent response of T700S/2500 UDTC at strain rates of 0.0001 s^{-1} and 100 s^{-1} . The transverse tensile strength and modulus were reported to increase 12.5% and 17.8% with the increase in strain rate, respectively. Note, since the in-plane transverse tensile response of the UDTCs is dominated by the properties of the matrix, the conflicted findings about the effect of strain rate on the transverse modulus might be due to different epoxy systems used in the studies. Nevertheless, studies focused on characterizing the effect of strain rate on the transverse tensile response of UD-NCF composites are lacking in the literature.

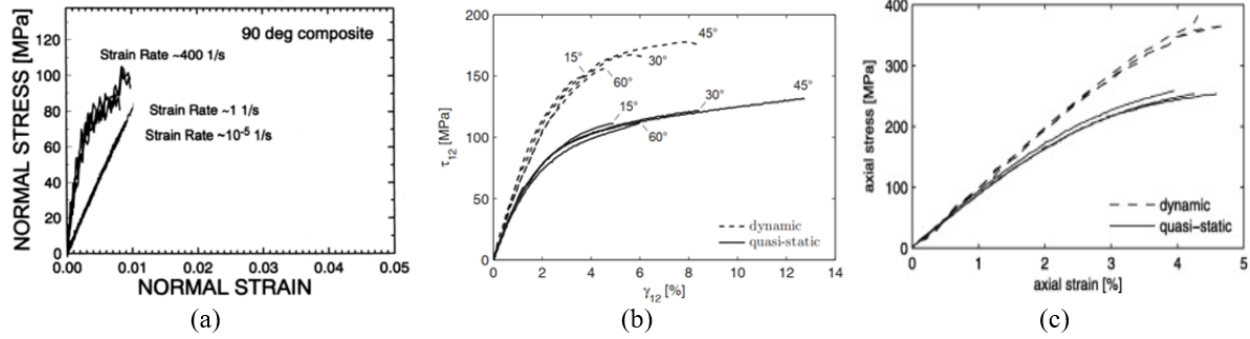


Figure 2-5: Stress-strain plots for UDTCs tested under different strain rates: (a) Transverse tension [49], (b) In-plane shear [35], and (c) Transverse compression [35].

Several test methods have been developed to capture the in-plane shear response of FRPs under quasi-static loading conditions, including uniaxial tests on specimens with off-axis lamina [62] and $[\pm 45]_{ns}$ angle-ply laminates (ASTM D3518 [63]), the Iosipescu shear test (ASTM D5379 [64]), and notched rail shear tests (ASTM D7078 [65]). However, performing dynamic tests with the tensile or compression SHPB apparatus using the large fixtures required for Iosipescu and notched rail shear tests is not feasible due to the inertial effects that would influence the stress waves in the specimen. Therefore, off-axis lamina and $[\pm 45]_{ns}$ laminate tests have been used in previous work. Gilat *et al.* [49] measured the in-plane shear properties of IM7/977-2 UDTC by testing a $[\pm 45]_s$ laminate in tension under quasi-static (0.00009 s^{-1}), intermediate (2 s^{-1}) and high (600 s^{-1}) rates of strain. Quasi-static and intermediate tests were performed on a hydraulic testing machine, while the high strain rate tests were performed on a tensile SHPB. The ultimate shear stress was reported to increase by 41% with the increase in strain rate from 0.00009 s^{-1} to 600 s^{-1} . Taniguchi *et al.* [48] measured the in-plane shear response of T700S/2500 UDTC using a $[\pm 45]_s$ laminate under quasi-static (0.0001 s^{-1}) and high (100 s^{-1}) rates of strain. Shear strength and shear modulus were reported to increase by 77.5% and 77.1%, respectively, over the range of strain rates tested. Cui *et al.* [37] characterized the strain rate-dependent response of IM7/8552 UDTC using a $[\pm 45]_{4s}$ laminate. Quasi-static (0.00005 s^{-1}) and high rate (1300 s^{-1}) tests were performed on a screw-driven testing machine and a SHPB apparatus, respectively. A 46% increase in the shear strength was reported with the increase in strain rate. Off-axis laminae have also been used by several researchers [15, 16, 45, 62] to study the strain rate-dependent in-plane shear behavior of carbon-epoxy UDTCs. Koerber *et al.* [35] characterized the strain rate-dependent in-plane shear behavior of IM7/8552 UDTC. Off-axis specimens oriented at 15° , 30° and 45° from the loading axis were tested under a quasi-static strain rate of 0.0004 s^{-1} using a hydraulic testing machine and at strain rates from 90 s^{-1} to 350 s^{-1} using a compression SHPB. Pure in-plane shear strength was obtained by applying a method proposed by Tsai and Sun [62], which requires plotting the ultimate transverse and shear strengths of off-axis laminates. A 42% increase in the shear strength and 18% increase

in the shear modulus was observed for the specimens tested under elevated strain rates (**Figure 2-5b**). Other researchers [16, 45, 62] have also reported similar effects of strain rate on the in-plane shear response of unidirectional composites.

Hsiao and Daniel [45] studied the effect of strain rate on the longitudinal compressive response of IM6G/3501-6 UDTC using a hydraulic testing machine for strain rates below 10 s^{-1} and a drop tower for strain rates between 10 s^{-1} and 110 s^{-1} . The longitudinal compressive strength and strain-to-failure were reported to increase by 79% and 74%, respectively, with the increase in strain rate from quasi-static to 110 s^{-1} . Yokoyama and Nakai [66] studied the effect of strain rate on T700/2521 UDTC at quasi-static (0.002 s^{-1}), intermediate (0.1 s^{-1}), and high (320 s^{-1}) strain rates. The longitudinal compressive strength was reported to be strain rate independent, while a decrease of about 15% in the strain-to-failure was observed. Hosur *et al.* [67] studied the effect of strain rate on the longitudinal compression response of DA 4518 UDTC from quasi-static to 817 s^{-1} strain rate. Compressive strength and stiffness were reported to increase 7 – 26 % and 2 – 3 times, respectively, with the increase in strain rate over the range considered. Koerber and Camanho [17] studied the effect of strain rate on the longitudinal compression of IM7/8552 UDTC under quasi-static (0.00036 s^{-1}) and high strain rate (93 s^{-1}) loading using a newly developed dynamic compression fixture. All specimens were found to fail at the ends for both quasi-static and dynamic loading (**Figure 2-6a** and **Figure 2-6b**), respectively. Nevertheless, a 40% increase in the longitudinal compression strength and strain-to-failure was reported for this increase in strain rate (**Figure 2-6c**). In later studies [68, 69] by the same group, the dynamic compression fixture was modified to mitigate premature failure at the specimen ends. The longitudinal compression strength measured with the modified fixture was 17% more than reported in [17]; however, the effect of the strain rate on the longitudinal compression strength was similar in both studies ([17, 69]). Recently, Gilat and Seidt [18] tested T800/F3900 UDTC in longitudinal compression at strain rates of 0.001 s^{-1} and 730 s^{-1} using a hydraulic testing machine and a compression SHPB set up, respectively. Longitudinal compressive properties were reported to be strain rate insensitive. The discrepancy in the strain rate dependency of the longitudinal compression response of carbon/epoxy UDTC reported in different studies might be due to different failure modes observed during testing. In general, measuring the longitudinal compression strength of UD composites by end loading test specimens is challenging because end brooming and ply splitting occurs before the expected in-phase fiber micro-buckling occurs, causing premature failure of the specimens [36]. Different matrix materials and fiber-matrix interfacial bonding strength may have also contributed to the discrepancies reported in previous studies.



Figure 2-6: Images of the failed specimens tested at: (a) quasi-static strain rate [17], and (b) high strain rate [17]. (c) Stress-strain response for specimens tested in longitudinal compression at quasi-static and high rates [17].

Yokoyama and Nakai [66] studied the effect of strain rate on the in-plane transverse compression response of T700/2521 UDTC. The quasi-static (0.002 s^{-1}) and intermediate (0.2 s^{-1}) strain rate experiments were performed on a servo-hydraulic testing machine, while high strain rate experiments (up to 700 s^{-1}) were performed on a compression SHPB apparatus. An increase of about 13% in the ultimate strength was observed with the increase in strain rate, while a marginal decrease in the strain-to-failure with the increase in strain rate was reported. Koerber *et al.* [35] investigated the strain rate-dependent response of IM7/8552 UDTC under quasi-static (0.0004 s^{-1}) and high strain rate (271 s^{-1}) loading using a hydraulic test frame and a compression SHPB setup, respectively. Some specimens were reported to fail along fracture planes of approximately 55° with respect to the loading axis. A 12% increase in the transverse modulus and 45% increase in the ultimate compressive strength were observed with the increase in strain rate from 0.0004 s^{-1} to 271 s^{-1} (**Figure 2-5c**). Schaefer *et al.* [16] tested specimens of IM7/8552 UDTC at 0.0001 s^{-1} , 0.1 s^{-1} and 800 s^{-1} and reported similar trends to those reported by Koerber *et al.* [17]. Recently, Gilat *et al.* [18] tested T800/F3900 UDTC at 0.001 s^{-1} and 550 s^{-1} using a hydraulic testing machine and a compression SHPB, respectively. A 70% increase in the transverse compressive strength was reported with the increase in the strain rate from 0.001 s^{-1} and 550 s^{-1} .

Previous studies have focused on characterizing the strain rate-dependent behaviour of UDTCs, whereas a few studies have characterized UD-NCF composites. Jorg and Wolfgang [70] characterized the strain rate-dependent response of a TORAYACA/Sika UD-NCF composite using two high-speed servo-hydraulic test machines. Transverse tension and compression tests were performed for strain rates up to 100 s^{-1} . The transverse tensile strength and compressive strength were found to increase by 35% and 20% with an increase in strain rate from 0.001 s^{-1} to 100 s^{-1} , respectively. In-plane shear tests were performed with

strain rates in the range of 10^{-5} s^{-1} to 1 s^{-1} . The shear strength was found to increase by 15% over the strain rates considered.

A summary of the effect of strain rate on each deformation mode is provided:

- The longitudinal tensile properties of UDTCs exhibit negligible strain rate dependency.
- The transverse tensile strength has positive strain rate-dependency; however, no conclusion can be drawn about the effect of strain rate on the transverse modulus and transverse tensile strain-to-failure.
- In-plane shear yield stress and ultimate strength have moderate to significant positive strain rate dependency, while the strain rate dependency of the in-plane shear modulus is slight to moderate.
- Transverse compression strength exhibits slight to significant strain rate dependency, while the transverse modulus has slight strain dependency.
- Conflicting findings have been reported in the literature about the effect of strain rate on the longitudinal compression response of UDTCs; thus, it is difficult to draw conclusions.
- Several reported studies did not consider pulse shaping for high strain rate tests nor did they report whether a constant strain rate or dynamic force equilibrium was achieved; therefore, the effect of strain rate on the complete stress-strain response in those studies may not be reliable.

2.4 Multiscale Modelling of NCF Composites

2.4.1 Introduction to multiscale modelling

The mechanical properties of FRP composites can be predicted by conducting virtual experiments that utilize multiscale modelling techniques [71]. Virtual experimentation is a powerful tool that can potentially reduce laboratory experimentation, which can be prohibitively expensive and time consuming especially when characterization must be performed for different deformation modes at various strain rates. Virtual experiments can also be used to characterize the deformation response of an FRP material along a direction that is difficult to measure through physical experiments. Multiscale models consider the structure of the material at multiple length scales, including micro-scale, meso-scale, and macro-scale (**Figure 2-7**). Two main multiscale modeling strategies have emerged, namely hierarchical and concurrent, with the former more widely employed for FRP composite materials [72]. Hierarchical multiscale modelling approaches involve predicting the material deformation response at different length scales sequentially and passing information between length scales using either a bottom-up and top-down approach. In a top-down multiscale modelling approach, analysis begins at the macro-scale and moves down to the micro-scale. While a bottom-up multiscale modelling approach begins at the micro-scale and moves up to the macro-scale. Bottom-up multiscale modelling approach is commonly used to predict the effective macroscopic

response and thermomechanical properties of the material using the constituent properties of the material [73, 74]. Bottom-up multiscale analysis begins with the identification of a suitable representative volume element (RVE) for the material at the micro-scale [75, 76]. The number of fibres and their spatial arrangement in the RVE affects the predicted properties of the composites; therefore, a balance between accuracy and computational costs must be maintained [77, 78, 79, 80]. For fabric reinforced composites, RVEs must also be defined at the next relevant length scale (i.e., the mesoscale) where the unit cell of the fabric must be considered.

Analytical, numerical and combined analytical/numerical homogenization approaches are used to perform analysis at each length scale. The classical analytical models or the so-called mean field homogenization (MFH) approximations include Voigt and Reuss approximations (*i.e.* rule of mixture), Hashin and Shtrikman's bound, Mori-Tanaka (M-T) method, Self-Consistent scheme and Method of Cells [76]. Voigt [81] and Reuss [82] developed some of the first models that were used to determine the effective elastic properties of UD composites. These models provide the upper and lower bounds to the elastic properties. Hashin and Shtrikman [83] developed an improved model that gives a stricter bound to the elastic moduli than the Voigt and Reuss models. The M-T theory [84] was originally developed to relate the average stresses and strain in the inclusion with those of the matrix material. Later, Benveniste [85, 86] developed the M-T tensor using the Eshelby's Equivalent inclusion theory, and the effective properties of composites were determined from this tensor. Several researchers [87, 88, 89, 90, 91, 92, 93, 94] modified the M-T theory and applied it to capture different behaviors (homogenized elastic properties, average elastic-plastic response, damage and interfacial debonding) of various types of composites containing inclusions of various sizes and shapes. Generalized Method of Cells (GMC) is another widely used micromechanics based theory that was originally developed by Jacob Aboudi [95], considering the square shape of the inclusions. Later, several modified versions of GMC were developed to predict different behaviors of composites such as strength of long fiber composites [96], time dependent response of composites [97], stiffness of composites containing anisotropic fibers [98], interface debonding in composites [99] and interphase modeling in composites [100]. Self consistent scheme [101] is also a well-known approach in the micromechanics; however, it yields good results when the stiffness of the constituent is similar such as the polycrystalline materials.

Recently, Sabiston *et al.* [102] developed a unit-cell model, namely Functionally Graded Interphase (FGI) model, based on the interaction between the matrix and fiber for a long fiber composite. An interphase was defined to capture the load transfer between the fiber and matrix. The predicted results were compared with the one's obtained with the method of cell [103], and it was observed that the model was able to predict the average stress-strain behavior for a large range of volume fractions. In a later study [104], the model was extended to capture the elasto viscoplastic behavior of the composites, and an excellent agreement was

observed between the predicted and experimental results. Some other researchers have also developed advanced homogenization methods [105, 106, 107], and implemented in the finite element (FE) codes.

Some MFH approaches can predict the homogenized response of composites with good accuracy and are computationally efficient. However, the main bottleneck is their inability to capture the local stress fields and the fact that they need to be reformulated with a change in the shape of the inclusion that is critical for the damage initiation and evolution due to the change in the stress concentration with the change in the shape of the inclusion. Therefore, numerical homogenization-based approaches remain the preferred choice when it comes to the accuracy. Most commonly used numerical homogenization approaches include mechanics of structure genome (MSG) [76] and 3D FE method (FEM) with periodic boundary conditions [108]. MSG [109] is based on the variational asymptotic method and is a unified approach that allows multiscale constitutive modelling for materials with all types of microstructure, and was originally developed for predicting the elastic response. 3D FE-based multiscale models allow for the accurate representation of the material microstructure (e.g., multiple nonuniformly dispersed fibers) to better capture the 3D stress fields within the constituents, which allows for accurate prediction of the effective properties as well as damage onset and failure. Another advantage of FE-based approaches is that manufacturing-induced defects can be represented within the RVE, which can further increase the accuracy of predictions. FE-based modelling begins by designing an RVE in the 3D or 2D space depending on the heterogeneity. The RVE is then meshed and boundary conditions are applied to the defined RVE. It has been shown [108] that periodic boundary conditions (PBCs) provide the most accurate estimate of the effective mechanical response of FRPs. The effective properties of a UDTC can typically be predicted by applying a homogenization approach at the microscopic length scale whereby the constituent properties are used. However, a dual-scale homogenization approach is required to predict the effective properties of FRPs, including UD-NCF composites, which enables capture of the in-tow and inter-tow material structure (**Figure 2-7**) and potential defects at each length scale.

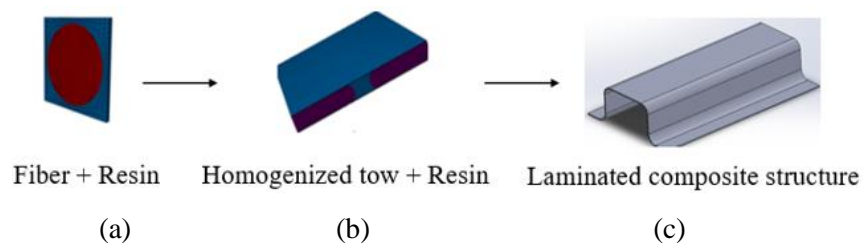


Figure 2-7: Flowchart for a hierarchical multiscale modelling approach for UD-NCF composite: (a) Micro-scale, (b) Meso-scale, (c) Macro-scale.

2.4.2 Review of relevant literature

Several studies have been reported in the literature that focus on predicting the quasi-static deformation response and failure of NCF composites through virtual experimentation. Edgren and Asp [110] developed an analytical model based on Timoshenko beam theory to predict the in-plane elastic properties of a NCF composite lamina and laminates, consisting of T700SC / DION 9500-501, in the presence of tow crimp. Ply level stiffness reduction factors were introduced into a classical laminate plate theory (CLPT) framework. Despite achieving a good agreement between the experimental and predicted results, the model may yield inaccurate results if the misalignment angle is high. Olsson *et al.* [111] proposed simple analytical models, similar to the rule of mixture and Halpin-Tsai models [112], for predicting the elastic moduli in the longitudinal, transverse and in-plane shear modes of a UD NCF composite, consisting of Tenax HTS carbon fiber and RTM 6 resin. Failure in the fiber dominated mode (longitudinal tensile) was predicted by applying a constant strain model, while a constant stress model was applied to predict failure in the matrix dominated modes (transverse tension and in-plane shear). A reasonable agreement between the predicted and measured results was reported; even though, this model ignored the tow crimp and fiber misalignment. Drapier and Wisnom studied the compressive strength of NCF composites using a 2D FE model [113]. It was suggested that the stitching tension should be kept low for better compressive strength properties. Marklund *et al.* [114] developed a multiscale approach where a mesoscale FE model was used to predict the tensile and compressive transverse strength of a multidirectional (MD) NCF composite, consisting of Tenax HTS carbon fiber and RTM 6 resin. The epoxy was modelled as an elastic-plastic material using a linear Drucker Prager plasticity model. A good agreement between the experimental and predicted transverse tension and compression strengths was reported. The effective mechanical properties of the impregnated tows (microscale) were measured from experiments on equivalent UD composites, which is deemed to be a drawback of this approach. Cao *et al.* [115] studied the effect of fiber misalignment on the mechanical properties of a NCF composite, comprising of Toray T700 carbon fiber and Epikote 828 resin, using a multiscale modelling framework. A small decrease in the longitudinal stiffness, while a significant decrease in the longitudinal strength due to fiber misorientation was reported.

González *et al.* [116] used 3D FE models that capture tow crimp to predict the tensile, compressive, and shear response of a Tenax HTS 5632/epoxy UD-NCF composite. The longitudinal tensile modulus and in-plane Poisson's ratio were reported to be dependent on the tow crimp angle, while the transverse and in-plane shear moduli were found to be independent of the crimp angle. A key outcome from this study was that simple analytical models such as rule of mixture are not appropriate for NCF composites. Ernst *et al.* [117] proposed a multiscale (micro, meso and macro) framework to predict the stress-strain behavior of a UD-NCF composite. The epoxy matrix, RIM 135, was modelled using a pressure dependent plasticity

model, while glass fibers were modelled as a linear elastic material. The predicted effective mechanical properties were used to simulate a three-point bending test. A good agreement between the predicted and experimentally measured force-displacement response was reported. Lidgett [118] developed a multiscale modelling methodology, involving two scales, to predict the strain rate-dependent macroscopic response of a cross-ply NCF composite laminate. The fibers were modelled as rate independent transversely isotropic linear elastic materials, while the matrix was modelled as a strain rate-dependent isotropic linear elastic material. The tow, at the meso-level, was modelled as a rate independent transversely isotropic linear elastic material. The strength and stiffness for the matrix and tow were scaled with the strain rate using the scaling functions. The damage initiation was modelled using the max-stress failure criteria, and the interfacial debonding was captured with the cohesive zone elements. A notable variation between the predicted and experimental results was reported at both quasi-static and intermediate strain rates. It was suggested that an improved material model for the epoxy material and considering the strain rate dependency of the fibers may improve the predictions. Recently, Singh *et al.* [119] developed a micromechanics-based model for predicting the rate-dependent stress-strain response of a carbon fiber/epoxy NCF composite under the compression loading. The matrix was modelled as an isotropic material using a viscoelastic-viscoplastic material model, while the fibers were modelled as the transversely isotropic linear elastic material. It was reported that model can qualitatively capture the increase in the stress-strain response with the increase in the strain rate; however, some discrepancies were observed in the predicted and experimental quantitative data.

Based on the literature review, the following gaps were identified:

- Most studies present models that predict the deformation response and failure of NCF composites under quasi-static loads without considering the strain rate-dependent response.
- Many studies assume that the matrix behaves as a linear elastic material, while there is substantial evidence that the matrix materials (such as epoxies) exhibit significant inelastic response.
- Many studies do not consider tow crimp and misalignment or in-tow nonuniform fiber dispersion; thus, the material microstructure is not well represented.

2.5 Macromechanical Response of FRPs

The generalized constitutive or stress-strain response of an orthotropic FRP lamina can be represented in four stages including linear elastic, pre-peak softening, peak, and post-peak softening (**Figure 2-8a**). Material models that can capture the entire stress-strain behaviour of FRPs for different modes are required to support accurate simulation of the crashworthiness of laminated FRP structures [120].

During the elastic stage, the stress-strain response remains linear and follows a generalized Hooke's law in which there is no permanent deformation after unloading. Pre-peak softening represents the inelastic response before reaching the maximum stress, which is attributed to accumulating micro-damage and localized yielding of the matrix material [121]. The peak represents the initiation of failure (i.e., transition from pre-peak to post-peak softening) that can be predicted using stress- or strain-based failure criteria (see Section 2.5.3.1). Post-peak softening represents the subsequent macroscale damage evolution that leads to the final failure of a lamina. A brief overview of the theoretical approaches used to predict the material response in each of these regions is provided below.

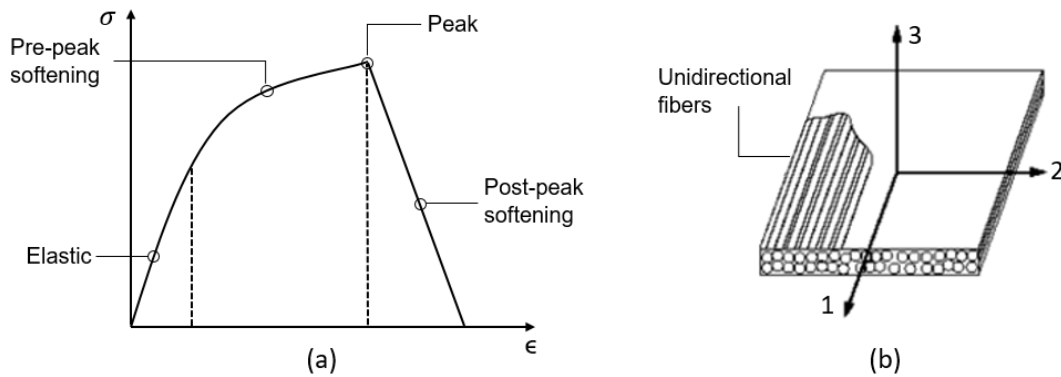


Figure 2-8: (a) Generalized stress-strain response of an FRP lamina (showing different stages of deformation), (b) An image showing a UD lamina with material axis [122].

2.5.1 Linear elastic response of composite materials

The theory of linear elasticity is only applicable when the deformations are small and the material does not permanently deform. The linear elastic stress-strain relation for FRPs can be described using the generalized Hooke's law:

$$\underline{\sigma} = \underline{\mathbf{C}} : \underline{\epsilon} \quad (4)$$

where $\underline{\sigma}$, $\underline{\mathbf{C}}$, $\underline{\epsilon}$, and $:$ denote the second-order Cauchy stress tensor, fourth-order effective stiffness tensor second-order infinitesimal strain tensor, and double dot product, respectively. A fully populated fourth order stiffness matrix with 36 terms is needed to describe the complete stress-strain relation of an anisotropic material. However, UD-NCF composites exhibit three orthogonal planes of symmetry; therefore, they can be treated as orthotropic materials. The stress-strain response in the reduced Voigt notation can be described as:

$$\begin{Bmatrix} \sigma_{11} \\ \sigma_{22} \\ \sigma_{33} \\ \sigma_{12} \\ \sigma_{23} \\ \sigma_{31} \end{Bmatrix} = \begin{bmatrix} C_{11} & C_{12} & C_{13} & 0 & 0 & 0 \\ C_{12} & C_{22} & C_{23} & 0 & 0 & 0 \\ C_{13} & C_{23} & C_{33} & 0 & 0 & 0 \\ 0 & 0 & 0 & C_{44} & 0 & 0 \\ 0 & 0 & 0 & 0 & C_{55} & 0 \\ 0 & 0 & 0 & 0 & 0 & C_{66} \end{bmatrix} \begin{Bmatrix} \varepsilon_{11} \\ \varepsilon_{22} \\ \varepsilon_{33} \\ \varepsilon_{12} \\ \varepsilon_{23} \\ \varepsilon_{31} \end{Bmatrix} \quad (5)$$

The stiffness matrix terms can be related to the effective elastic constants, which can be found using multiscale mechanics or from experimental data, by using the following relations:

$$C_{11} = \frac{1 - \nu_{23}\nu_{32}}{E_2 E_3 \Delta}, C_{22} = \frac{1 - \nu_{13}\nu_{31}}{E_1 E_3 \Delta}, C_{33} = \frac{1 - \nu_{12}\nu_{21}}{E_1 E_2 \Delta} \quad (6)$$

$$C_{12} = \frac{\nu_{21} + \nu_{31}\nu_{23}}{E_1 E_2 \Delta}, C_{13} = \frac{\nu_{31} + \nu_{21}\nu_{32}}{E_2 E_3 \Delta}, C_{23} = \frac{\nu_{32} + \nu_{12}\nu_{31}}{E_1 E_3 \Delta} \quad (7)$$

$$C_{44} = G_{23}, C_{55} = G_{13}, C_{66} = G_{12} \quad (8)$$

$$\Delta = \frac{1 - \nu_{23}\nu_{32} - \nu_{13}\nu_{31} - \nu_{12}\nu_{21} - 2\nu_{21}\nu_{32}\nu_{13}}{E_1 E_2 E_3} \quad (9)$$

The thickness of UD lamina along the out-of-plane direction (see 3-axis in **Figure 2-8b**) is notably smaller when compared to the in-plane dimensions of an FRP component; therefore, lamina and laminates are often represented in an FE model using shell elements. Shell elements are computationally efficient and are desired for virtual structural analysis. Different element formulations exist for shell elements such as plane stress, plane strain and thick shells. For FRPs, a plane normal stress formulation is the most suitable because of the low thickness. For the plane normal stress state, normal stress through the thickness should vanish, *i.e.* $\sigma_{33} = 0$ [9]. Therefore, Equation (5) can be re-written as:

$$\begin{Bmatrix} \sigma_{11} \\ \sigma_{22} \\ 0 \\ \sigma_{12} \\ \sigma_{23} \\ \sigma_{31} \end{Bmatrix} = \begin{bmatrix} C_{11} & C_{12} & C_{13} & 0 & 0 & 0 \\ C_{12} & C_{22} & C_{23} & 0 & 0 & 0 \\ C_{13} & C_{23} & C_{33} & 0 & 0 & 0 \\ 0 & 0 & 0 & C_{44} & 0 & 0 \\ 0 & 0 & 0 & 0 & C_{55} & 0 \\ 0 & 0 & 0 & 0 & 0 & C_{66} \end{bmatrix} \begin{Bmatrix} \varepsilon_{11} \\ \varepsilon_{22} \\ \varepsilon_{33} \\ \varepsilon_{12} \\ \varepsilon_{23} \\ \varepsilon_{31} \end{Bmatrix} \quad (10)$$

It is important to note that through the through-thickness strain component does not vanish and can be re-written in terms of the stiffness matrix terms:

$$\varepsilon_{33} = -\frac{C_{13}}{C_{33}}\varepsilon_{11} - \frac{C_{23}}{C_{33}}\varepsilon_{22} \quad (11)$$

By substituting the value of the ε_{33} in the above equation, the in-plane normal stresses become:

$$\begin{Bmatrix} \sigma_{11} \\ \sigma_{22} \end{Bmatrix} = \begin{bmatrix} C_{11} - \frac{C_{13}C_{13}}{C_{33}} & C_{12} - \frac{C_{13}C_{23}}{C_{33}} \\ C_{12} - \frac{C_{23}C_{13}}{C_{33}} & C_{22} - \frac{C_{23}C_{23}}{C_{33}} \end{bmatrix} \begin{Bmatrix} \varepsilon_{11} \\ \varepsilon_{22} \end{Bmatrix} \quad (12)$$

The absence of through the thickness normal stress does not affect calculation of the shear stresses (σ_{12}, σ_{23} and σ_{31}), which remain the same as for the 3D orthotropic case and are provided in Equation (13).

$$\sigma_{12} = C_{44}\varepsilon_{12}, \quad \sigma_{23} = C_{55}\varepsilon_{23}, \quad \sigma_{31} = C_{66}\varepsilon_{31} \quad (13)$$

The strain rate dependency of the elastic properties can be introduced into the constitutive equations using scaling functions, which can be obtained by fitting the experimental results [11, 15] or using a viscoelastic model [123].

2.5.2 Pre-peak response

When deformed beyond its elastic limit, the stress-strain response of an FRP material becomes non-linear. The inelastic response of a lamina may be due to a combination of local plastic deformation of the matrix and damage development (*e.g.* matrix micro-cracking, fiber/matrix debonding etc.). Separating and quantify the different phenomena that contribute to the inelastic response requires a series of experiments and is not practical. Therefore, the inelastic response in the pre-peak stage may be assumed plastic and modelled using the theory of plasticity [124, 125, 126].

The main ingredients of a plasticity model include yield criteria, a hardening rule, and a flow rule [127, 128]. Yield criteria are often expressed in terms of stresses and define the yield surface in a 3D stress space. The hardening rule describes how the shape of the yield surface evolves under plastic deformation. The flow rule provides a relation between the plastic strain increments at a stress state and the unknown plastic multiplier, which is determined by ensuring that the stress state remain on the yield surface during plastic deformation. Moreover, some materials exhibit different yield stresses in tension and compression due to the pressure dependency of the material, in which a pressure-dependent yield criterion that considers the hydrostatic stresses can be used. Examples of pressure independent and dependent yield criteria are von Mises and Drucker Prager, respectively, which have been developed for isotropic materials. FRPs exhibit different yield strengths along different directions due to their anisotropic nature. To capture the directional dependent plastic behavior, anisotropic yield functions are required.

Sun and Chen [126] proposed a 3D plasticity model (Equation (14)) based on a quadratic yield function to model the pre-peak constitutive response of FRPs. The anisotropy of the proposed yield surface is governed by the a_{ij} parameters, which are obtained through experimentation.

$$\begin{aligned}
2f(\sigma_{ij}) = & a_{11}\sigma_{11}^2 + a_{22}\sigma_{22}^2 + a_{33}\sigma_{33}^2 + 2a_{12}\sigma_{11}\sigma_{22} \\
& + 2a_{13}\sigma_{11}\sigma_{33} + 2a_{23}\sigma_{22}\sigma_{33} \\
& + 2a_{44}\sigma_{23}^2 + 2a_{55}\sigma_{13}^2 + 2a_{66}\sigma_{12}^2 = k
\end{aligned} \tag{14}$$

An associated flow rule was used to define the plastic strain components:

$$d\varepsilon_{ij}^{pl} = \frac{\partial f}{\partial \sigma_{ij}} d\lambda \tag{15}$$

The increment of the effective plastic strain is:

$$d\bar{\varepsilon}_{pl} = \frac{2}{3} \bar{\sigma} d\lambda \tag{16}$$

where $d\lambda = \frac{3}{2} \left(\frac{d\bar{\varepsilon}_{pl}}{d\bar{\sigma}} \right) \left(\frac{d\sigma}{\bar{\sigma}} \right)$ and $\bar{\sigma} = \sqrt{3f}$. The scalar k is defined as:

$$k = \frac{2}{3} \bar{\sigma}^2 \tag{17}$$

The total incremental plastic strain was decomposed into decoupled elastic and plastic strain increments:

$$d\varepsilon_{ij} = d\varepsilon_{ij}^{el} + d\varepsilon_{ij}^{pl} \tag{18}$$

By assuming that there is no plastic strain along the fiber direction, *i.e.* $d\varepsilon_{11}^{pl} = 0$, and applying it to the associated flow rule, the following plastic coefficients are obtained:

$$a_{11} = a_{12} = a_{13} = 0 \tag{19}$$

On further manipulation, the following relationships between the a_{ij} coefficients are obtained:

$$a_{22} = a_{33}, a_{23} = -a_{22} \tag{20}$$

Assuming $a_{22} = 1$, the generalized yield function for plane stress conditions reduces to:

$$2f = \sigma_{22}^2 + 2a_{66}\sigma_{12}^2 \tag{21}$$

The effective stress for plane-stress conditions is defined by:

$$\bar{\sigma} = \left[\frac{3}{2} (\sigma_{22}^2 + 2a_{66}\sigma_{12}^2) \right]^{1/2} \tag{22}$$

The effective plastic strain increment is:

$$d\bar{\varepsilon}_{pl} = \left[\frac{3}{2} (\sigma_{22}^2 + 2a_{66}\sigma_{12}^2) \right]^{1/2} d\lambda \tag{23}$$

The value of parameter “ a_{66} ” in the above equation can be obtained from off-axis testing.

Despite being a simple plasticity model that requires only one parameter to be calibrated, the determination of the parameter requires testing several off-axis laminae and the model does not account for pressure- and strain rate-dependency [15]. Vogler *et al.* [125] developed a 3D transversely isotropic elasto-plastic model to capture the non-linear constitutive response of FRPs. Pressure dependency was considered to accurately capture the tension/compression asymmetry of the yield surface. The model developed by Vogler *et al.* [125] was recently extended by Koerber *et al.* [41] to incorporate strain rate effects.

Goldberg *et al.* [129] introduced a general quadratic 3D orthotropic yield function similar to the Tsai-Wu failure criterion [130]. A non-associated flow rule was used to accurately compute the evolution of the plastic strain components. Pressure dependency was incorporated to capture the tension/compression asymmetry. A plane stress version of the model was later developed by Tobias [9] for shell elements that has been implemented in the commercial FE software LS-DYNA (LSTC, Livermore) as material model MAT_213.

Recently, Tan *et al.* [131] developed a strain rate-dependent micromechanically motivated deformation model based on the concept of crystal plasticity to capture shear deformation modes of UDTCs. Three slip systems were defined, and it was assumed that the plastic deformation occurs along one of these slip systems within the matrix. The model was implemented in Abaqus Explicit for 3D solid elements and validated for several strain rate-dependent cases that include off-axis lamina and laminates. The model does not require mode-dependent hardening curves or a master curve; thus, only a few experiments are required for calibration. However, a small mesh size (less than 1 mm) is required to accurately predict the stress-strain response that makes this model unsuitable for component level simulations.

The strain rate dependency of the post yield response can be introduced into the constitutive equations using scaling functions, which can be obtained by fitting the experimental results [15] or using viscoplastic models [41, 132, 9]. Viscoplastic models such as the Perzyna model [133] require additional characterization for their calibration, which complicates the calibration procedure.

2.5.3 Failure initiation and damage evolution in FRPs

Predicting the initiation of failure and subsequent evolution of damage in laminated FRPs is one of the most challenging tasks due to the presence of multiaxial stress states and interaction between different damage modes [11, 12, 134]. Damage modes can be broadly categorised as either intralaminar and interlaminar. Since the current work is focused on the intralaminar response of an FRP composite, the content in the subsequent sub-sections will be limited to intralaminar failure initiation and damage evolution.

2.5.3.1 Intralaminar failure initiation (peak)

Intralaminar failure modes represent the onset of failure or fully developed damage across the thickness of a lamina (**Figure 2-9**). A plethora of intralaminar failure criteria have been developed for FRPs, which can be broadly categorised as interactive, non-interactive, mode dependent and mode independent. Non-interactive failure criteria such as the max-stress and max-strain criteria consider only one stress component to predict failure of a lamina [135]. Interactive failure criteria such as the Tsai-Wu [130] criterion consider the effect of different stress components; however, such criteria have no physical basis [12]. Some researchers have developed interactive mode dependant failure criteria such as Puck, LaRC05,

and invariant based failure criteria. Puck criterion [136] comprises on two fiber failure modes (tension and compression) and three inter fiber failure modes. In the LaRC05 [137], failure is evaluated using two fiber failure functions and one inter fiber failure function. Both Puck and LaRC05 criterion requires finding the action plane that increases the computational costs significantly. Recently, some attempts have been made to develop and apply the invariant based failure criteria [138]. The invariant based failure criteria [138] eliminates the need of finding the action plane; and is computationally efficient and simple to implement.

During the past three decades, a series of World Wide Failure Exercises [139, 140] were undertaken to identify appropriate failure criteria for FRP composites; however, there was no consensus as to which failure criteria provided better estimates for damage initiation in laminae under different stress states. Nevertheless, physical-based mode dependent criteria were recommended since they provide comparatively improved predictions [11, 12]. Predicting damage initiation for plies within a MD FRP composite laminate is even more challenging because damage initiation and growth are affected by the position of the ply in the laminate due to the effect of ply constraints [75]. Strain rate dependency on the damage initiation can be introduced into the failure criteria using scaling functions, which can be obtained from experimental data [11, 15]. Several studies have used this approach to capture the strain effects on the failure initiation [41, 141, 142].

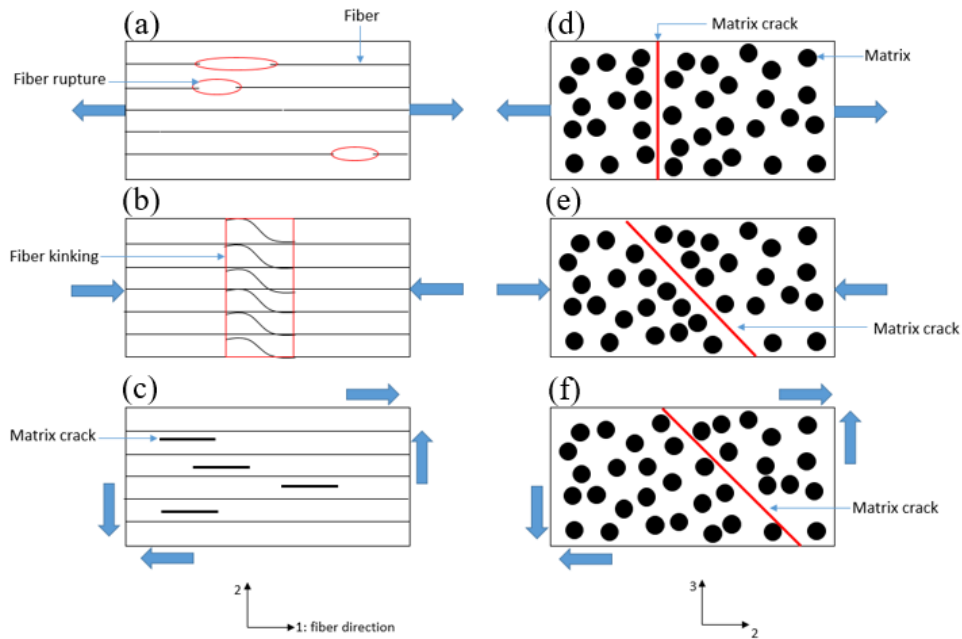


Figure 2-9: Intralaminar failure modes in unidirectional composites: (a) Fiber tensile mode, (b) Fiber compression mode, (c) In-plane shear mode, (d) Matrix tensile mode, (e) Matrix compression mode, (f) Out-of-plane shear mode.

2.5.3.2 Intralaminar damage evolution (post-peak response)

Two approaches, namely micro damage mechanics (MIDM) and macro damage mechanics (MADM), have been used to model damage evolution in laminated FRPs [143]. MIDM models focus on determining changes in the lamina properties using local stress states around cracks [143]. MADM, a.k.a continuum damage mechanics (CDM), models smear damage at lower length scales and consider the effects of damage on the material macroscopic (constitutive) response [11] (see **Figure 2-10**). Since the proposed research is focused on constitutive modelling of FRPs, the following discussion is limited to CDM-based models. Kachanov [144] introduced the fundamental concept of CDM and applied it to predict microvoid development preceding rupture in ductile metals subjected to creep loads. The development of microvoids was described by defining a scalar internal variable, ϕ , whose value varies from 0 (fully damage) to 1 (fully intact). The rate of material degradation, $\frac{d\phi}{dt}$, was represented as:

$$\frac{d\phi}{dt} = -A \left(\frac{\sigma}{\phi} \right)^m \quad (24)$$

where A and m are material parameters.

Robertson [145] redefined the scalar variable, ϕ , as $\omega = 1 - \phi$, and represented it as a function of reduction in the net area:

$$\omega = \frac{S_D}{S} = \frac{S - S^*}{S} \quad (25)$$

Here, S and S_D represent the undamaged and damage area, respectively. S^* is the net area of the damaged material excluding the area covered by damaged entities.

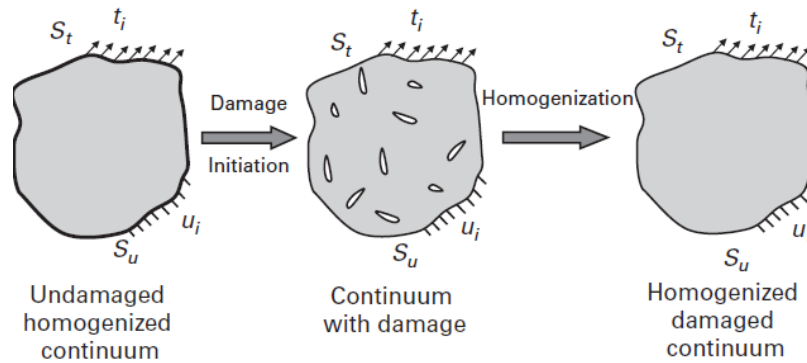


Figure 2-10: An illustration of homogenization of damage [143].

Using the definition of damage introduced by Robertson [145], the effective stress, $\bar{\sigma}$, is defined as:

$$\bar{\sigma} = \frac{\sigma}{1 - \omega} \quad (26)$$

Lemaitre and co-workers [146] used Robotnov's concept of effective stress along with the principal of strain equivalence to define the effective elastic modulus, \tilde{E} ,

$$\bar{\sigma} = \frac{\sigma}{1-\omega} = \frac{E}{\tilde{E}} \sigma \quad (27)$$

The damage variable, ω , introduced by Kachanov and Robotnov is scalar in nature, and cannot consider the directional dependency of the damage. Murakami and Ohno [147] developed constitutive equations for creep damage in metals by employing a symmetric damage tensor as an internal state variable. Later, Lemaitre and Chaboche [148] developed a relationship between the elastic constants and damage tensor. Using the damage tensor and the principal of strain equivalence, the relation between the applied stress, strain and damage stiffness tensor was derived [148]:

$$\underline{\sigma} = \mathbf{C}(\omega):\underline{\varepsilon} \quad (28)$$

where $\underline{\sigma}$, $\mathbf{C}(\omega)$ and $\underline{\varepsilon}$ represent the applied stress, damage stiffness, and strain tensors, respectively.

Most CDM models developed for FRP composites represent damage using anisotropic damage tensors with parameters that are functions of strain or strain rate. A key difference between different CDM based models lies in the description of damage evolution [11]. A simple damage evolution law was proposed in the Chang-Chang model [149] for laminated composites where elastic properties were degraded according to the Weibull distribution. Another approach for deriving the damage evolution law is based on the thermodynamical potentials as was applied by Matzenmiller *et al.* [150] and Ladeveze and Le Dantec [151] for FRPs. Pinho *et al.* [152] proposed a 3D CDM model where the damage evolution was defined based on experimentally measured intralaminar fracture toughness associated with different modes. A similar approach was used by Tan *et al.* [153] to predict damage evolution in laminated composites under low velocity impact. In both of these studies the effect of strain rate on damage evolution and post-peak response was ignored despite experimental evidence that suggests otherwise [154, 155, 156].

2.6 Existing Material Models in Commercial FE Software

Simulating the impact response and accurately predicting the energy absorption of FRP composite structures requires robust material models that are capable of capturing the different deformation stages of laminae (**Figure 2-8a**), while considering the material strain rate dependency. Several material models for laminae have been developed and implemented into commercial FE software such as LS-DYNA, Abaqus CAE (Dassault Systèmes Simulia Corp., Providence), RADIOSS (Altair Engineering Inc., Michigan) and PAM-CRASH (ESI Group, Paris). LS-DYNA is widely used in the automotive and aerospace sectors for simulating the dynamic response of load-bearing structures [9]. LS-DYNA utilizes an explicit integration scheme for dynamic problems that requires small time increments and may be computationally expensive; therefore, shell elements are commonly used to perform component level and full-vehicle simulations [157].

A review of the existing material models for FRP composites available in LS-DYNA that have been developed for shell elements follows.

MAT_22 (Composite damage) is based on the Chang-Chang failure criterion [149] and was developed to model the tensile and shear failure in bolted composite joints. Five strength parameters, including longitudinal tensile strength, transverse tensile strength, transverse compressive strength, in-plane shear strength, and a non-linear shear stress parameter, are required to calibrate three failure criteria [115]. MAT_022 has limited applicability and is not suitable for crash simulations since it does not include post-peak softening response, nor does it consider fiber compressive failure [158].

MAT_054 (Enhanced composite damage) is an improved version of MAT_022 that considers fiber compressive failure and is widely used for simulating impact of composite structures [8, 159, 160]. Composites are modelled as orthotropic linear elastic materials until failure, which is predicted using the Chang-Chang failure criteria [149]. The model does not consider physical based post-peak softening and instead assumes a sudden property degradation followed by a constant residual stress after failure. It uses a combination of non-physical parameters which can be broadly categorized: erosion parameters, crash front softening parameters, and material response parameters. A significant effort is required to calibrate these non-physical parameters iteratively as outlined by Dharmaraj [5]. The MAT_055 material model is similar to MAT_054 where instead a Tsai-Wu based failure criteria is used.

MAT_058 is a constitutive continuum damage model that considers four damage modes: fiber rupture, fiber kinking, matrix cracking and matrix crushing. Failure initiation is evaluated using Hashin's failure criteria [161]. The model takes into account both the pre-peak and post-peak softening, which is incorporated through a CDM-based model proposed by Matzenmiller *et al.* [150]. MAT_058 has been used to simulate impact events for structures made of UDTCs, UD-NCF composites, textile composites and honeycomb structures [5, 162, 163]. Recently, an attempt [142] was made to incorporate strain rate effects to perform material, coupon and components level simulations at different strain rates using MAT_058.

MAT_158 is an updated version of MAT_058 that provides the option of capturing the strain rate-dependent elastic response, which are incorporated through a Maxwell model using linear viscoelasticity. The model can capture stress increase only for small stress magnitude (up to approximately 15% of the total stress). However, it has been seen that composites exhibit significant strain rate dependency especially in the in-plane shear and transverse compression modes [17]. Further, MAT_158 does not consider strain rate effects on the pre-peak softening which is commonly observed in composites.

MAT_219 is a CDM-based material model that was developed for capturing progressive damage in FRP laminates [164]. Unlike the previous material models that are formulated for a single lamina, this material model requires definition of sub-laminates as building blocks within a laminate. Therefore, the material model captures the effect of ply constraint on damage evolution [165]. Damage initiation is

modelled using the mode-dependent strain-based criteria, while damage growth is modelled by the composite damage model (CODAM) [164]. MAT_219 has been used to simulate the impact performance of various composite structures [121, 160]. Nevertheless, material model MAT_219 has two main limitations, including neglecting the strain rate dependency of the material response and it requires testing of the specific laminate under consideration for calibration [9].

MAT_213 is a lamina-based elasto-plastic-damage material model for FRPs that has been recently developed for solid and shell elements [121, 9, 124]. The model considers pre-peak softening response due to both yielding and damage. The yield function is defined using a generalized modified form of the Tsai-Wu failure criterion. A non-associated flow rule is used to compute the plastic strain increments. The pre-peak damage is incorporated using a tensorial damage framework based on Matzenmiller's approach [150]. A generalized tabulated failure criteria is used and elements are deleted once failure is predicted. Thus, the material post-peak response is not considered with this material model. The strain rate dependent deformation response was captured using a viscoelastic-viscoplastic model. This model also accounts for the effect of temperature on the yield stress. The applicability and accuracy of this model has not been rigorously evaluated to date. The main limitation of the model is the requirement of more than 100 calibration parameters [166].

MAT_261 is an orthotropic CDM model [167] for FRPs that is implemented in LS-DYNA for solid and shell elements. It considers the pre-peak softening in the in-plane shear mode. Failure initiation is modelled based on the physical based failure models developed by Pinho *et al.* [12]. Damage evolution (post-peak response) for each deformation mode is governed by the associated experimentally measured intralaminar fracture toughness. MAT_261 has been used to simulate the crash and impact response of FRP structures [8, 14, 168]. The predicted results have been reported to be lower than the experimental values; however, 'tuning' the effective failure strain leads to improved correlation with the experiments [14]. The limitations of the MAT_261 model include ignoring strain rate effects and pre-peak softening response for longitudinal and transverse tension/compression modes. MAT_262 is another orthotropic CDM-based material model [13] that is similar to MAT_261. The main difference is that MAT_262 employs the LaRC04 failure criteria for damage initiation and assumes bilinear softening for the damage evolution in the longitudinal direction [169].

The review of existing material models available in LS-DYNA has revealed the following limitations:

- i. Most models do not account for the effect of strain rate on the complete deformation response, which limits their ability to accurately predict the impact response of composite structures at different loading rates.
- ii. Some material models require extensive material characterization for calibration of parameters (*e.g.* MAT_213) or the calibration of non-physical parameters (*e.g.* MAT_54, MAT_58), which can significantly increase the associated cost and modelling effort.

- iii. Aside from MAT_261, MAT_262 and MAT_213, the material models do not consider pre-peak softening response, even though there is considerable experimental evidence revealing that FRP composite materials exhibit inelastic response in the transverse compression and shearing modes [35].
- iv. Aside from MAT_261, MAT_262 and MAT_213, the material models utilize failure criteria that are not physical based and are generally not regarded as robust [170].

Chapter 3: Research Objectives and Scope

3.1 Research Objectives

The overarching goal of this research is to support the development of a high-fidelity CAE impact simulation model for fiber-reinforced composite energy absorbing structures. To this end, a comprehensive material model will be developed for a material system that comprises a heavy-tow carbon fiber UD-NCF and a snap-cure epoxy resin and is manufactured using the HP-RTM process.

Stemming from the gaps identified in the literature review (Chapter 2) and summarized in Table 3-1, the research project addresses the following main objectives:

1. Characterize the strain rate-dependent transversely isotropic deformation response and failure characteristics of the UD-NCF composite material to provide calibration data for an associated material constitutive model;
2. Develop a validated computational multiscale model to predict the strain rate-dependent transversely isotropic deformation response of the UD-NCF composite material to provide additional calibration data for the material constitutive model;
3. Develop and verify a strain rate-dependent pre-peak deformation model for the UD-NCF composite material and implement into a commercial FE software to support future CAE impact simulations.

Table 3-1: Objectives, gaps, and tasks for the proposed research work

Objectives	Gaps in Literature	Tasks
1. Strain rate-dependent constitutive characterization	<p>The strain rate-dependent deformation response and fracture behaviour of heavy-tow UD-NCF carbon fiber/snap-cure epoxy composites have not been previously studied.</p> <p>The strain rate-dependent response of UD composites reported in the literature is conflicting for some deformation modes and may be due to deficiencies with experimental protocols.</p>	<p>1.1 Develop dynamic testing protocols.</p> <p>1.2 Perform transverse tensile, transverse compression, longitudinal compression, and in-plane shear tests at three strain rates.</p>
2. Develop a strain rate-dependent multiscale model for virtual experimentation	<p>Several computational models were previously developed to predict the orthotropic deformation response and failure of UD-NCF composites; however, few of these accurately capture the material microstructure or can predict the material response at different strain rates.</p>	<p>2.1 Develop a multiscale model to predict the quasi-static orthotropic elastic properties and verify with test data.</p> <p>2.2 Develop a multiscale model to predict the strain rate-dependent inelastic deformation response and verify with test data.</p>
3. Develop and implement a strain rate-dependent pre-peak deformation material model	<p>Existing material models used to capture the generalized stress-strain response of FRP composites do not consider strain rate effects for all stages of deformation (<i>i.e.</i> linear elastic, pre-peak softening, peak, and post-peak softening), and/or require extensive calibration of non-physical parameters or comprise a significant number of physical parameters that are difficult to calibrate.</p>	<p>3.1 Develop a plane-stress strain rate-dependent elasto-plastic deformation model at the lamina level.</p> <p>3.2 Implement the deformation model in LS-DYNA for shell elements and perform verification and validation tests at the coupon level.</p>

3.2 Scope of Work

The proposed research work comprises three main tasks, each addressing the corresponding project objectives (Table 3-1). The workflow is shown in Figure 3-1 and described in the following paragraphs.

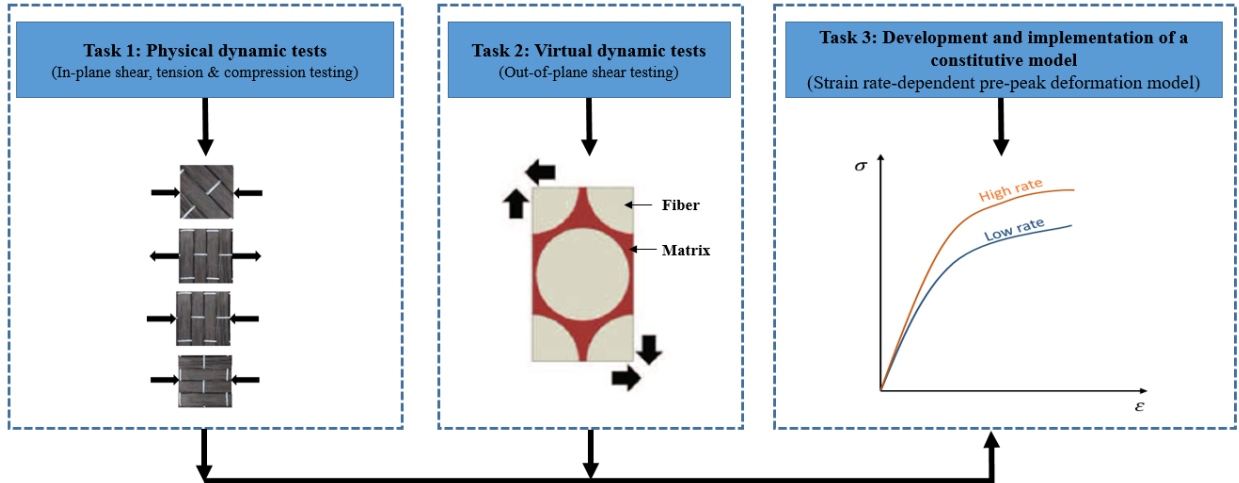


Figure 3-1: Schematic showing the proposed research plan.

3.2.1 Task 1

Task 1.1 focuses on developing protocols for the dynamic tests and designing testing fixtures. All designed testing fixtures are integrated into existing testing frames/apparatus. Suitable pulse shapers are identified for use with the SHPB apparatus for the high rate tensile and compression tests. *Task 1.2* focuses on characterizing the strain rate-dependent deformation and failure response of the UD-NCF composite. All tests are performed at three strain rates, namely quasi-static ($< 10^{-2} \text{ s}^{-1}$), intermediate ($10^{-2} - 10^2 \text{ s}^{-1}$) and high ($10^2 - 10^3 \text{ s}^{-1}$) rates. The quasi-static and intermediate-rate tests are performed on hydraulic testing machines, while the high rate tests are performed on compression and tensile SHPB apparatus. All tests are performed at nearly constant strain rate and under dynamic equilibrium.

3.2.2 Task 2

Task 2.1 focuses on developing the multiscale modelling framework for predicting the elastic properties of the UD-NCF carbon fiber/snap-cure epoxy composite at quasi-static strain rates. FE models based on micrographic assessment of the UD-NCF composites are developed at both the microscale and mesoscale, in which periodic boundary conditions (PBCs) are applied to the RVEs through custom Python scripts in Abaqus. The effective lamina elastic properties are obtained through volumetric stress averaging

and are compared with the obtained experimental results (Task 1.2). *Task 2.2* involves using the developed multiscale modelling framework (Task 2.1) to predict the strain rate-dependent non-linear stress-strain response of the UD-NCF carbon fiber/snap-cure epoxy composite. Existing dynamic test data for the resin [23] is used for this task. The deformation response of the lamina under longitudinal tension, transverse tension and in-plane shear is predicted and validated with the obtained experimental data (Task 1.2). The validated FE model is then be used to predict the lamina out-of-plane shear stress-strain response.

3.2.3 Task 3

Task 3.1 focuses on the theoretical development of a strain rate-dependent invariant-based transversely isotropic elasto-plastic deformation model suitable for shell elements. *Task 3.2* involves the development of a user defined material subroutine in FORTRAN and its implementation into LS DYNA for shell elements. The constitutive model is calibrated using the obtained physical and virtual test data (*Tasks 1.2 and 2.2*) for the UD-NCF composite material and published data for the IM7-8552 UDTC. The VUMAT is verified and validated for different strain rates.

Chapter 4: Research Results

This chapter summarizes the results that were obtained from the tasks outlined in **Chapter 3** to address the associated research objectives. First, an overview of the material system investigated in this study is presented. Next, a summary of the results obtained from the experimental characterization (Task 1) and virtual experimentation (Task 2) are provided. Finally, the verification and validation results obtained from the constitutive model developed in this research work (Task 3) are presented. A more detailed presentation of the methodology and results for Tasks 1, 2, and 3 can be found in Appendices A-B, Appendices C-D, and Appendix E, respectively. Each appendix comprises a published or submitted peer-reviewed journal paper:

- Appendix A **Rouf, K.**, Suratkar, A., Imbert-Boyd, J., Wood, J., Worswick, M., & Montesano, J. (2021). Effect of strain rate on the transverse tension and compression behavior of a unidirectional non-crimp fabric carbon fiber/snap-cure epoxy composite. *Materials*, 14(23), 7314.
- Appendix B **Rouf, K.**, Worswick, M., & Montesano, J. (2023). Effect of strain rate on the in-plane mechanical response of a unidirectional non-crimp fabric carbon fiber/snap-cure epoxy composite. Manuscript submitted (under review).
- Appendix C **Rouf, K.**, Worswick, M. J., & Montesano, J. (2021). A multiscale framework for predicting the mechanical properties of unidirectional non-crimp fabric composites with manufacturing induced defects. *Journal of Composite Materials*, 55(6), 741-757.
- Appendix D **Rouf, K.**, Worswick, M. J., & Montesano, J. (2023). Experimentally verified dual-scale modelling framework for predicting the strain rate-dependent nonlinear anisotropic deformation response of unidirectional non-crimp fabric composites. *Composite Structures*, 303, 116384.
- Appendix E **Rouf, K.**, Worswick, M., & Montesano, J. (2023). An invariant-based constitutive model to capture the non-linear strain rate-dependent deformation response of fiber-reinforced composite materials: formulation and finite element implementation. Manuscript submitted (under review).

4.1 Materials and Manufacturing

The composite material under investigation consists of PX35 UD300 unidirectional NCF (Zoltek Corp.; **Figure 2-1**) and a snap-curing three-part epoxy system (Westlake Epoxy). The binder stabilized NCF comprises unidirectional tows each with 50,000 continuous PX35 high strength carbon fibers and transversely oriented supporting glass fibers, which are bonded with a polyester stitch in a warp knitted tricot pattern [20]. The resin system includes EPIKOTE™ Resin TRAC 06150, EPIKURE™ Curing agent TRAC 06150 and an internal mold release agent HELOXY™ Additive TRAC 06805 [23]. The flat panels of the material were manufactured through the HP-RTM manufacturing process at Fraunhofer Innovation Platform for Composites Research (London, Canada). Details of the HP-RTM manufacturing process used to produce flat panels of the NCF composites are described in [29]. The measured fiber volume fraction for the manufactured panels was 53% [171], and void percentage was found to be less than 2% [172]. The test specimens were cut from the flat panels using an abrasive water jet cutting machine (Protomax, OMAX) with an abrasive mesh size of 80 and a pressure of 30,000 psi. The test specimens for the compression testing were machined on a milling machine using a titanium carbide bit at 2000 RPM, and it was ensured that the loading ends of the specimens are parallel (within 0.02 mm). The dimensions of the test specimens were decided based on several factors. First, it was ensured that at minimum there were two unit cells of the fabric structure along both the width and length directions of the samples as per ASTM standard D6856 [173]. The specimens were also limited in size to mitigate inertial effects and ensure dynamic force equilibrium during dynamic tests. The compression specimens were sized to reduce frictional effects and prevent specimen buckling. Schematics of the compression and transverse tension specimens are shown in **Figure 4-1**. The stacking sequence, specimen gauge dimensions and nominal panel thickness for different tests are provided in **Table 4-1**.

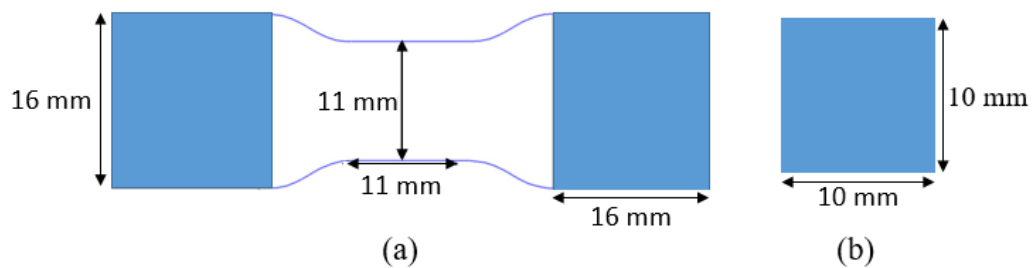


Figure 4-1: Schematics of test specimens with dimensions: (a) Transverse tension, (b) Compression

Table 4-1: Nominal gauge dimensions and lay-up sequence of specimens used for different tests.

Test type	Nominal specimen gauge section dimensions	Stacking sequence
Transverse tension	$11 \times 11 \times 2.3 \text{ mm}^3$	$[90]_7$
In-plane shear	$10 \times 10 \times 2.6 \text{ mm}^3$	$[\pm 45]_{2s}$
Transverse compression	$10 \times 10 \times 3.3 \text{ mm}^3$	$[90]_{11}$
Longitudinal compression	$10 \times 10 \times 2.3 \text{ mm}^3$	$[0]_7$

4.2 Task 1: Strain Rate-Dependent Constitutive Characterization [Appendix A and Appendix B]

The strain rate-dependent characterization of the UD-NCF composite material was performed for the transverse tension, transverse compression, longitudinal compression, and in-plane shear modes at three strain rates (quasi-static, intermediate, and high rate). The achievable strain rate for the high strain rate tests varied for different deformation modes due to the distinct deformation response of the specimens for each mode as well as limitations of the test setup. However, the minimum achieved strain rate was higher than the average strain rate normally observed during automobile crash events (i.e., $>50 \text{ s}^{-1}$) [174]. Details about the test setups and DIC setup are omitted here for brevity, and can be found in Appendix A and Appendix B. The strain rate dependent characterization for the longitudinal tensile mode was not performed since the deformation response in this mode is primarily governed by carbon fibers, and it has been observed that UD composites, made from carbon fibers, exhibit negligible strain rate dependency for the longitudinal tension mode [48]. The strain rate dependent characterization for the out-of-plane shear mode was performed through the virtual experimentation (Task 2) because the transverse shear testing requires special fixtures that can induce dynamic effects in the test results at high rates and interfere with the incident and transmitted wave signals on SHPB.

4.2.1 Development of testing protocol

4.2.1.1 Pulse shaping for high-rate testing on the compression split-Hopkinson pressure bar

Preliminary tests were performed to calibrate the compression SHPB apparatus using a similar material system with a 45% fiber volume fraction [51, 174, 172] (Appendix A). The high strain rate testing of the UD-NCF carbon fiber/snap-cure epoxy composite for the longitudinal compression, transverse

compression, and in-plane shear was performed using a maraging steel compression SHPB apparatus (**Figure 4-2a**). An oxygen-free high thermal conductivity (OFHC) copper pulse shaper with 0.5 mm thickness and 7 mm diameter was used to achieve dynamic equilibrium and a nearly constant strain rate. An OFHC pulse shaper was chosen because of its low yield stress when compared to that of the bar material (steel). The dimensions for the pulse shaper were obtained based on the pulse shaping analysis (PSA) proposed by Nemat-Nasser *et al.* [53], and was attached to the incident bar with a thin film of petroleum jelly. The copper pulse shaper was effective in modifying the pulse shape to a desired ramped shape (**Figure 4-2b**), while dynamic equilibrium was established, as evidenced by the consistency with the incident and transmitter end forces (**Figure 4-2c**). The unloading portion of the incident pulse shape was not elastic, indicating that the pulse shaper was being plastically deformed through the creation of the incident pulse. It is noted that the dispersion-free oscillation assumption is usually not fulfilled for the classical rectangular pulse since there is oscillation in the incident pulse signal initially. However, the pulse shaper minimizes those oscillations, as shown in (**Figure 4-2b**), to a point that the dispersion free assumption is satisfied [15]. The strain was found to increase linearly with time after the initial loading period, allowing a nearly constant strain rate to be calculated based on the slope of the linear region of the strain-time plot (**Figure 4-2d**). The specimens initially exhibited a linear stress–strain response; however, the stress–strain response became non-linear with increasing strain (**Figure 4-3**). The stress-strain response was found to be repeatable with minor scatter. The bending percentage for all tested specimens was measured through a high-speed camera and was found to be lower than 10% before failure. Further details about the bending percentage measurements can be found in Appendix A.

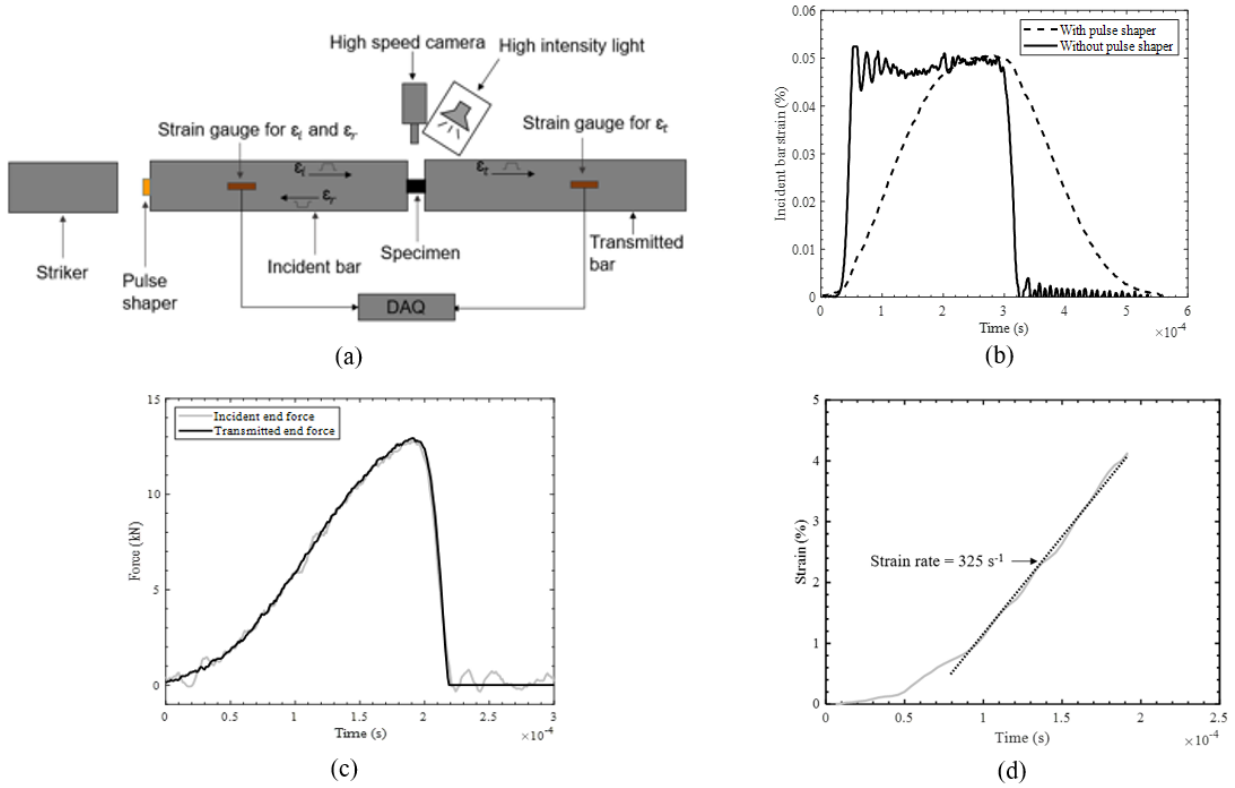


Figure 4-2: (a) Schematic of a compression SHPB showing a pulse shaper at the end of the incident bar, (b) Comparison of an incident bar pulse with and without a copper pulse shaper (without specimen), (c) Comparison of the incident and transmitted bar forces with pulse shaper, (d) Strain-time evolution during a high strain rate transverse compression test.

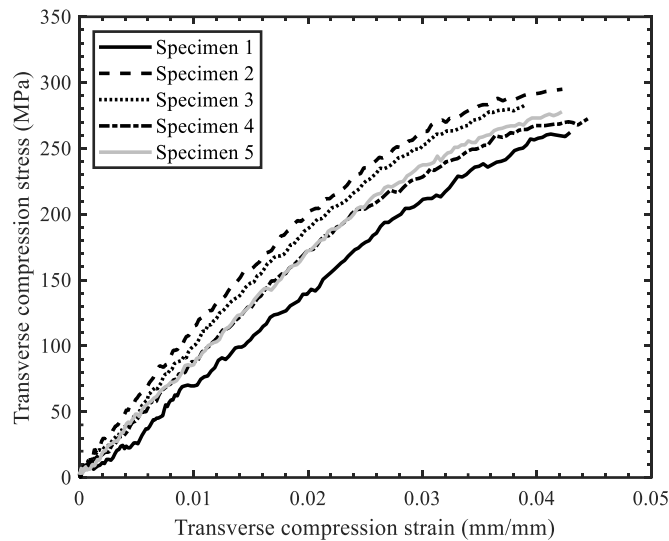


Figure 4-3: Stress–strain response for transverse compression tests, performed at high strain rate (325 s^{-1}).

4.2.1.2 Pulse shaping for high-rate testing on the tensile split-Hopkinson pressure bar

A tensile SHPB apparatus with aluminum bars was used to perform high strain rate transverse tension tests. Preliminary tests were also performed to calibrate the tensile SHPB apparatus. Different materials, including rubber, brass, copper, lead and lead-tin, and geometries were considered to identify a suitable pulse shaper (**Figure 4-4a**). Lead-tin wire having a diameter of 3 mm was found to be the most suitable pulse shaper to modify the shape of the input pulse (**Figure 4-4b**) and achieve dynamic equilibrium (**Figure 4-4c**). A lead-tin pulse shaper was used for all subsequent tests performed on the tensile SHPBs. It is noted that the dispersion-free oscillation assumption is usually not fulfilled for the classical rectangular pulse since there is oscillation in the incident pulse signal initially. However, the pulse shaper minimizes those oscillations, as shown in (**Figure 4-4b**), to a point that the dispersion free assumption is satisfied [15]. It is noted that there is an impedance mismatch between the specimen and the bars; however, the magnitude of the signal was strong enough to measure it accurately.

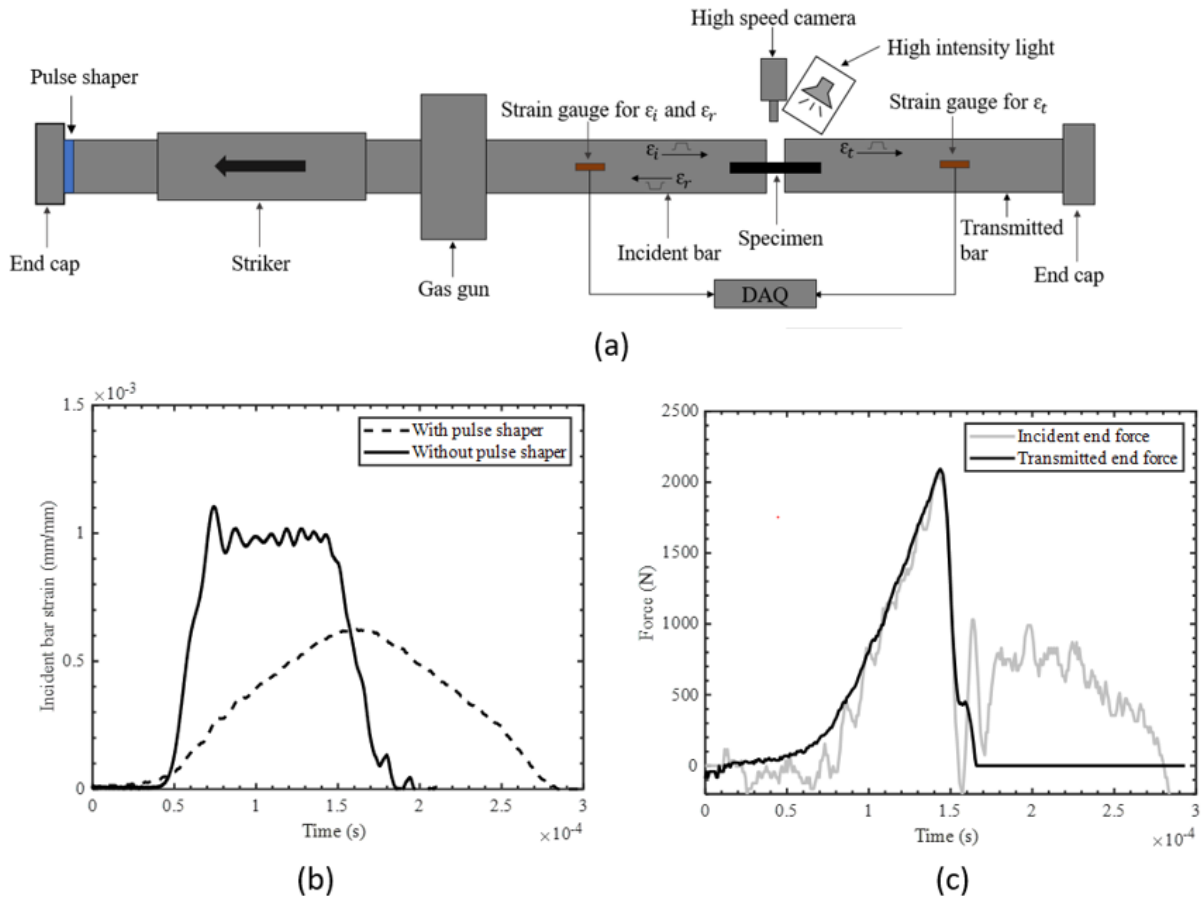


Figure 4-4: (a) Schematic of a tensile SHPB showing a pulse shaper on the incident bar, (b) Comparison of incident bar pulse with and without a lead-tin pulse shaper, (c) Comparison of the incident and transmitted bar forces with pulse shaper.

4.2.2 In-plane shear testing results

The in-plane shear deformation and failure response of the UD-NCF carbon fiber/snap-cure epoxy composite was characterized by subjecting specimens with a $[\pm 45^\circ]_{2s}$ stacking sequence to a uniaxial compression load at room temperature. In total, three shear strain rates were considered, including quasi-static (0.003 s^{-1}), intermediate (1.8 s^{-1}) and high (315 s^{-1}). The specimens had nominal dimensions of $10 \text{ mm} \times 10 \text{ mm}$, with a thickness of 2.6 mm , and were end loaded [175]. Each specimen was lubricated with a thin layer of molybdenum sulphide grease to reduce contact friction with the loading platens. Quasi-static and intermediate tests were performed on a custom-built servo-hydraulic test frame equipped with an MTS 407 controller and a 20,000 lbf (88,964 N) capacity load cell. The high strain rate tests were performed on a compression SHPB apparatus with maraging steel bars (**Figure 4-2a**). High speed cameras were used to capture images at 60 fps, 10,000 fps and 360,000 fps for the quasi-static, intermediate and high rate

experiments, respectively. For all tests, cameras were triggered manually before applying the load. The deformation response of the specimens was obtained by post-processing the images obtained from the high-speed cameras in the GOM Aramis image correlation software. Further details about the test set-up can be found in Appendix B.

A significant nonlinear shear stress-strain response was observed in the specimens tested at all strain rates (**Figure 4-5**), which is attributed to the inelastic behavior of the matrix material [35]. The shear stress-strain response also exhibited some degree of pre-peak softening. The average values (**Figure 4-6**) of the elastic modulus and the initial yield stress (0.2% offset) were found to increase by approximately 10% and 60%, respectively, with the increase in strain rate from 0.003 s^{-1} to 315 s^{-1} . The in-plane shear strength was also found to increase by 61% over the same range of strain rates. Based on statistical analysis (one-way ANOVA and Tukey's test with significance level: $p \leq 0.05$), the average in-plane shear yield stress and strength are significantly different at the three strain rates considered. However, there is no significant difference among the shear moduli.

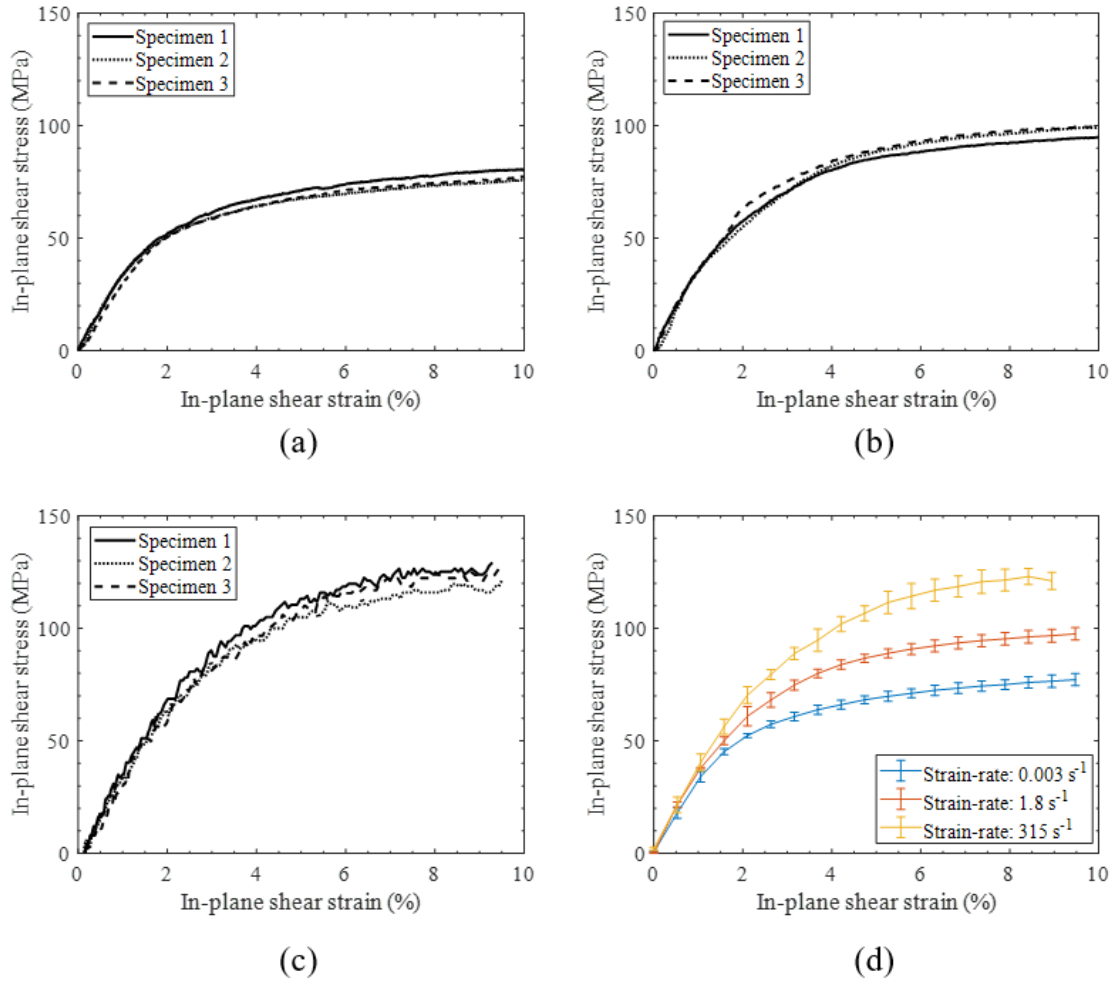


Figure 4-5: Stress-strain plots for in-plane shear tests at strain rates of: (a) 0.003 s^{-1} , (b) 1.8 s^{-1} , and (c) 315 s^{-1} . (d) Average stress-strain plots for indicated strain rates with standard error bars.

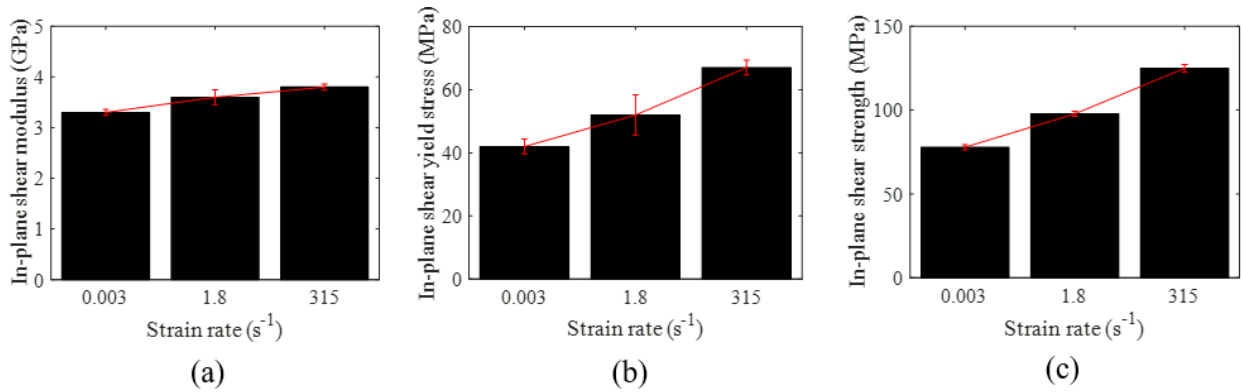


Figure 4-6: Average in-plane shear properties of the UD-NCF composite for indicated strain rates: (a) Modulus, (b) Yield stress, (c) Ultimate strength

The empirical relationships for the average in-plane shear yield stress, strength and modulus as a function of strain rate were established by fitting the data with a semi-logarithmic expression (**Figure 4-7**), which can be used to interpolate these properties at other strain rates. Specimens tested at all strain rates were found to fail in a brittle manner with fracture planes oriented 45° biased to the loading direction (**Figure 4-8a** and **Figure 4-8b**). Most supporting fibers were found to be intact in the microscopic images (**Figure 4-8b**), indicating that the transverse stresses were low during the tests. The fracture surfaces of the specimens could not be analyzed since the specimens remained intact after failure.

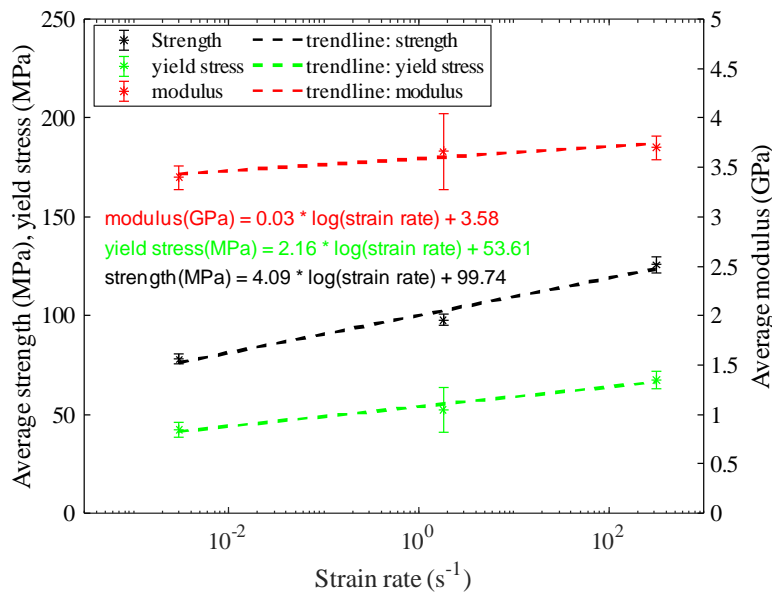


Figure 4-7: Average in-plane shear yield stress, strength and modulus versus strain rate for the UD-NCF composite with regression lines and empirical equations shown.

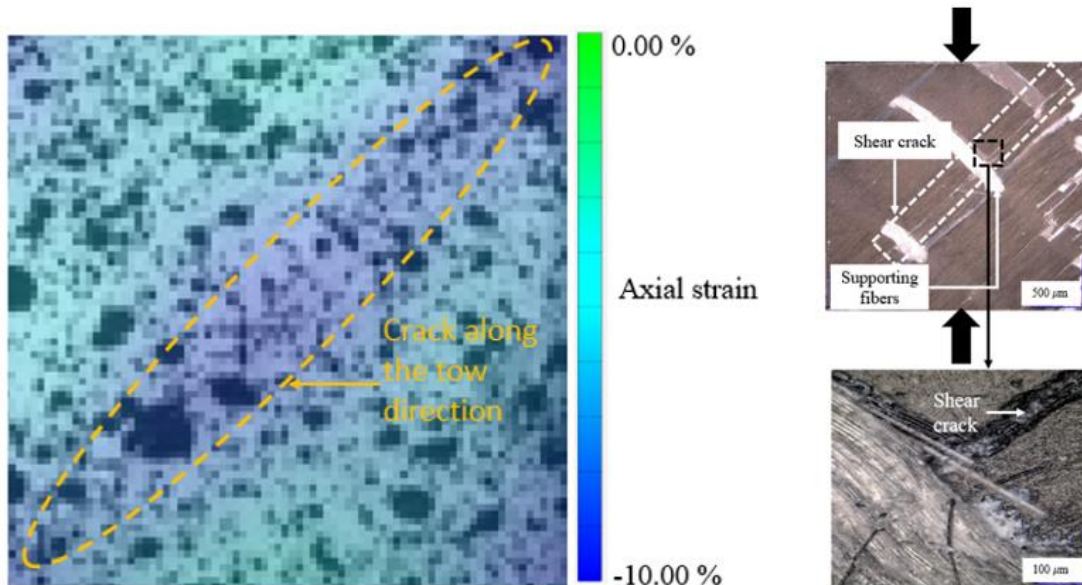


Figure 4-8: (a) An image showing axial strain distribution during a high rate shear test on the C-SHPB, (b) A microscopic image of the failed in-plane shear specimen tested at high strain rate.

4.2.3 Transverse tensile testing results

Transverse tensile testing of the UD-NCF carbon fiber/snap-cure epoxy composites was carried out at room temperature at three strain rates, including quasi-static (0.1 s^{-1}), intermediate (16 s^{-1}) and high (126 s^{-1}) rate. Quasi-static and intermediate strain rate tests were performed on a custom built hydraulic intermediate strain rate (HISR) testing frame using a custom pin loaded fixture. The frame was equipped with an MTS 407 controller and a 30,000 N capacity load cell. The high strain rate tests were performed on a tensile SHPB with aluminum bars (**Figure 4-4a**). Dog-bone shaped specimens with a $[90]_7$ stacking sequence and an $11 \text{ mm} \times 11 \text{ mm}$ gauge section were used for all performed tests. Each specimen was speckled with a black-on-white pattern to capture the specimen strain using digital image correlation (DIC). For both the low and intermediate strain rate tests, the camera was triggered through the data acquisition system (DAQ), while for the high strain rate test the camera was triggered manually. High speed cameras were used to capture images at frame rates of 10,000 fps, 46,500 fps, and 262,500 fps for the quasi-static, intermediate and high rate tests, respectively, and were post-processed in GOM Aramis image correlation software for the strain measures. Further details about the test set-up can be found in Appendix B.

The specimens exhibited a linear elastic response and brittle fracture at all testing rates (**Figure 4-9**), which is attributed to fiber/matrix de-bonding or matrix cracking. The strain-to-failure was found to be approximately 1% or lower (**Figure 4-9**). The average ultimate transverse tensile strength increased approximately 20% with an increase in strain rate from 0.1 s^{-1} to 126 s^{-1} (**Figure 4-10**). Based on a statistical

analysis (one-way ANOVA and Tukey's test with significance level: $p \leq 0.05$), there is a statistically significant difference between the average transverse tensile strength measured at 0.1 s^{-1} and 126 s^{-1} . However, no significant strain rate effects on the elastic modulus were observed.

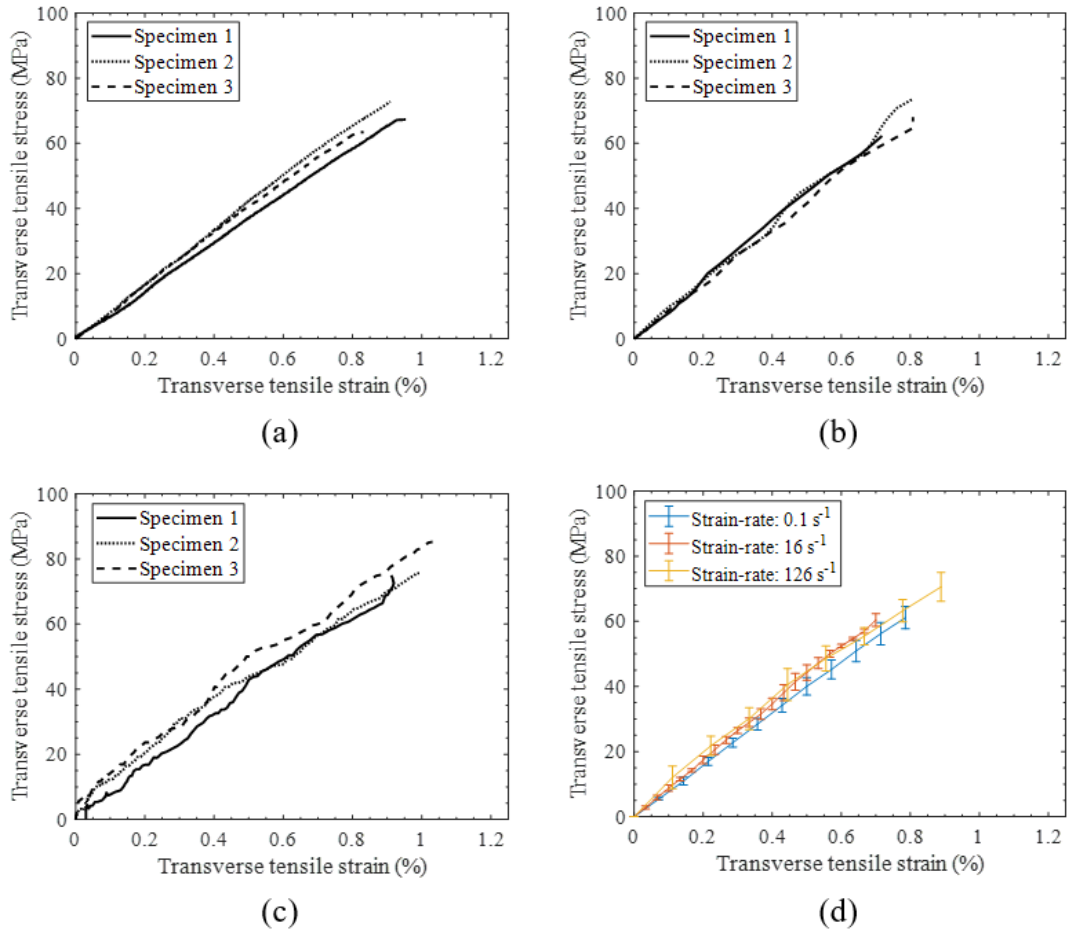


Figure 4-9: Stress-strain plots for transverse tensile tests performed at applied strain rates of: (a) 0.1 s^{-1} , (b) 16 s^{-1} , and (c) 126 s^{-1} . (d) Average stress-strain plots for indicated strain rates with standard error bars.

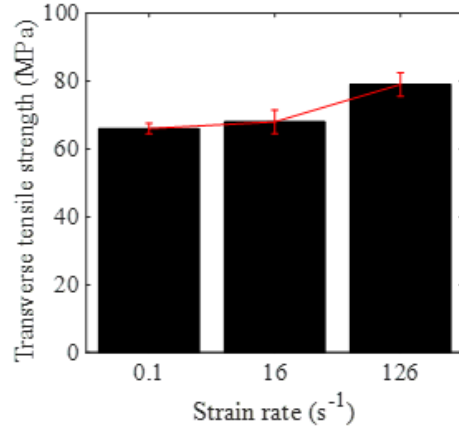


Figure 4-10: Average in-plane transverse tensile strength of the UD-NCF composite for indicated strain rates.

The empirical relationship for the average transverse tensile strength was obtained by fitting the data with a semi-logarithmic expression (**Figure 4-11**), which can be used to interpolate the transverse tensile strength at other strain rates. Specimens tested for the transverse tension tests were found to fail in the brittle mode for all rates (**Figure 4-12**). The orientation of the fracture plane was perpendicular to the loading direction. Multiple cracks were observed in the specimens tested at the high rate (**Figure 4-12c**) that might be due the increased stiffness of the matrix due to the increased applied strain rate. Fracture surfaces of the tested specimens at all rates were smooth in appearance. The scanning electron microscopy (SEM) of the fracture surface of the specimens revealed pull-out of the supporting fiber and broken supporting fibers (**Figure 4-13**). Most carbon fibers on the fracture surfaces were found to be bare that indicate that the transverse tension failure was mainly governed by the interfacial debonding at the matrix/fiber interface. Small deformation was also observed in the matrix rich region that indicate small local plastic deformation. These rate sensitive local mechanisms may contribute to the difference in the trend of transverse tensile strength with strain rate for UD-NCF composite when compared to that of UDTCs where a minor increase was reported previously [40, 49].

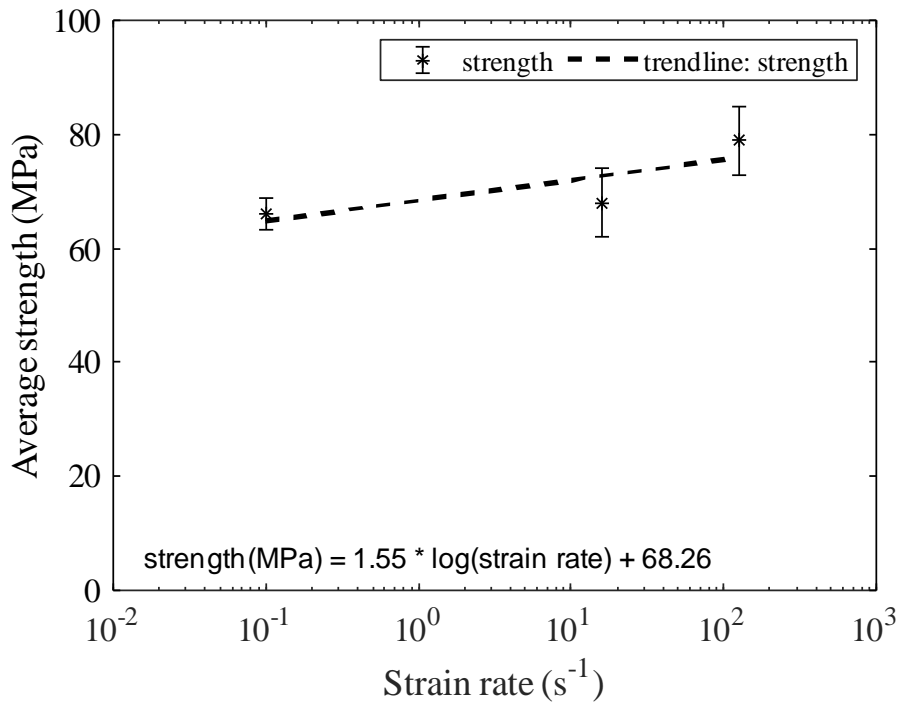


Figure 4-11: Average transverse tensile strength versus strain rate for the UD-NCF composite with regression line and empirical equation shown.

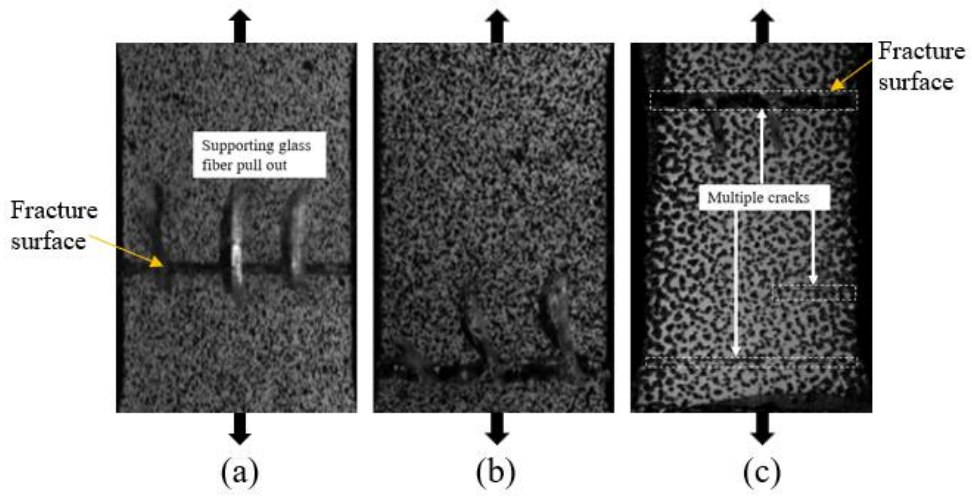


Figure 4-12: Images of failed transverse tension specimens at strain rate: (a) 0.1 s⁻¹, (b) 16 s⁻¹, and (c) 126 s⁻¹.

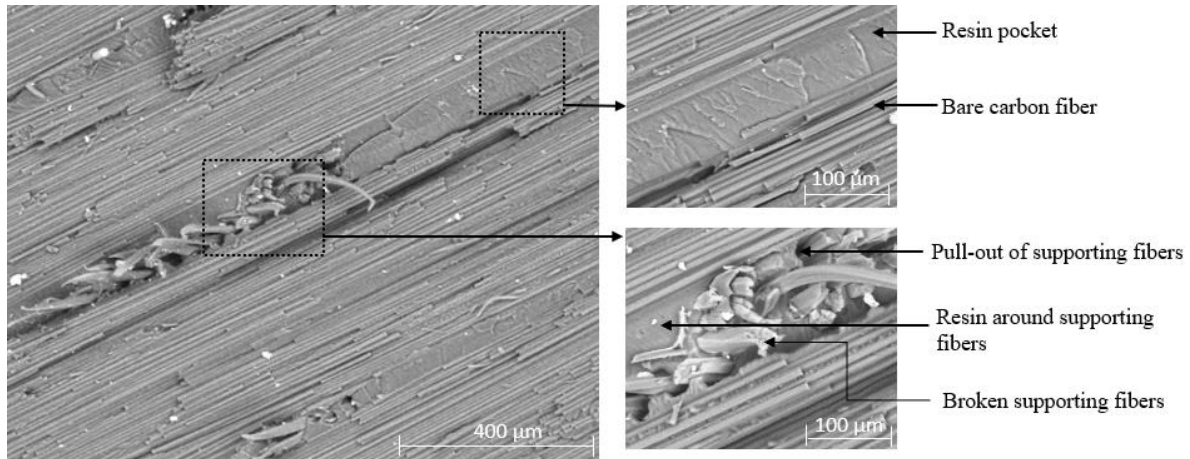


Figure 4-13: Fracture surface images of a transverse tension specimen (taken with a scanning electron microscope): 100x magnification (left) and 500x magnification (right).

4.2.4 Transverse compression testing results

Transverse compression tests were performed by uniaxially loading $[90]_{11}$ specimens ($10 \text{ mm} \times 10 \text{ mm}$) at room temperature under three strain rates, including quasi-static (0.003 s^{-1}), intermediate (1.4 s^{-1}) and high rate (260 s^{-1}). Tests were performed on the same testing machines used for the in-plane shear tests (Section 4.2.2). Some degree of non-linearity was observed in the stress-strain response at all strain rates (**Figure 4-14**). The compressive elastic modulus, yield stress and ultimate strength were found to increase by 20%, 54% and 50%, respectively, with the increase in strain rate from 0.003 s^{-1} to 260 s^{-1} (**Figure 4-15**). Based on the statistical analysis (one-way ANOVA and Tukey's test with significance level: $p \leq 0.05$), the average values of the transverse compressive yield stress and strength are significantly different; however, there is no significant difference among the elastic moduli measured at different rates.

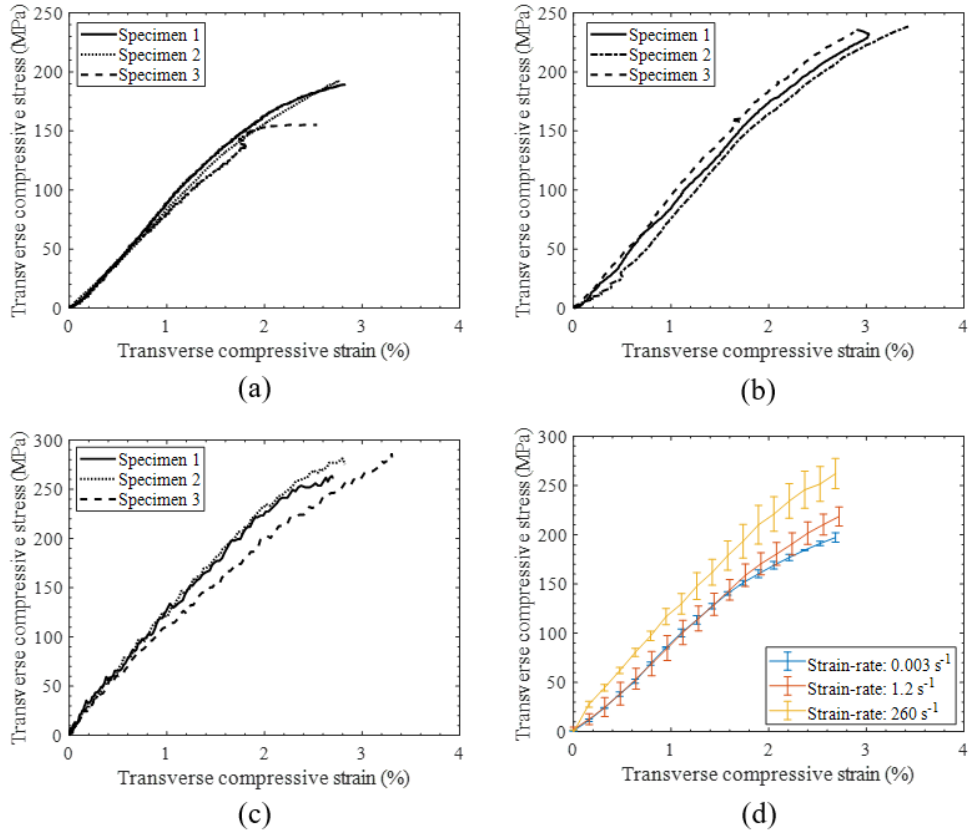


Figure 4-14: Stress-strain plots for transverse compression tests at strain rates: (a) 0.003 s⁻¹, (b) 1.2 s⁻¹, and (c) 260 s⁻¹. (d) Average stress-strain plots for indicated strain rates with standard error bars.

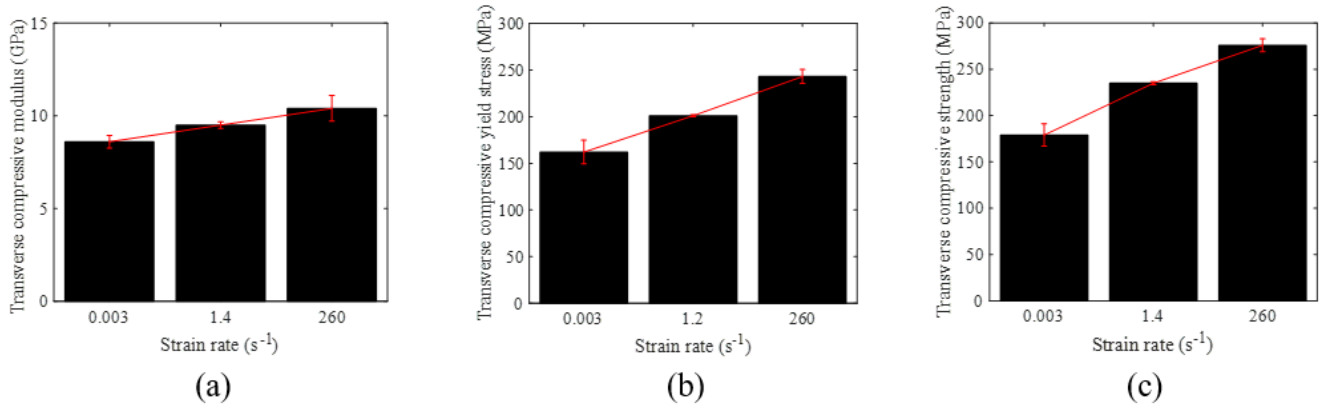


Figure 4-15: Average in-plane transverse compression properties of the UD-NCF composite for indicated strain rates (a) Modulus, (b) Yield stress, (c) Ultimate compression strength.

The empirical relationships (**Figure 4-16**) for the average transverse compression strength, yield stress and modulus were established as a function of strain rate by fitting the data with a semi-logarithmic expression. These relations can be used to interpolate these properties at other strain rates. The transverse compression specimens at all rates were found to fail along a plane biased to the loading direction and a small increase in the fracture angle was observed with increasing strain rate (**Figure 4-17**). Fracture surfaces were found to be smooth for the specimens tested at the quasi-static strain rate (**Figure 4-18a**), while fracture surfaces were rough for the specimens tested at the intermediate (**Figure 4-18b**) and high rate tests (**Figure 4-18c**). The increase in the roughness of the fracture surface might be due to the creation of multiple cracks (micro and macro) that was also observed in the previous studies [55, 39]. Multiple failure modes (broken fibers, matrix cracks, debonding of supporting fibers and carbon fibers from matrix) were seen in the SEM images (**Figure 4-19**) at all rates. However, it is inconclusive which failure mode precedes or succeeds.

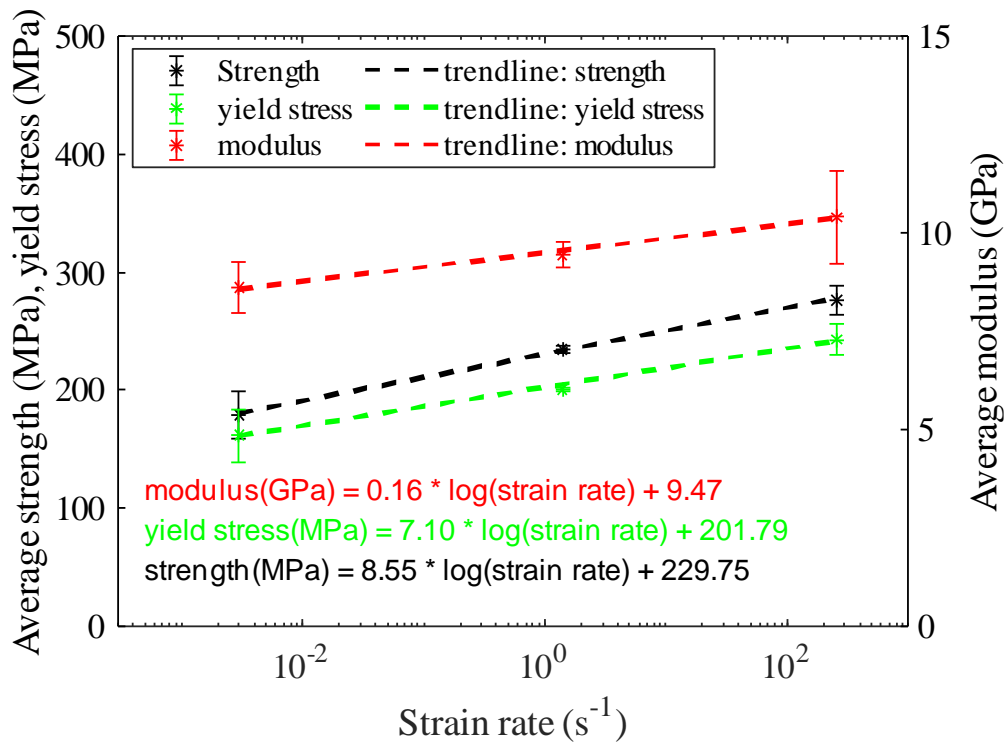


Figure 4-16: Average transverse compression strength, yield stress, and modulus versus strain rate with regression lines and empirical equations shown.

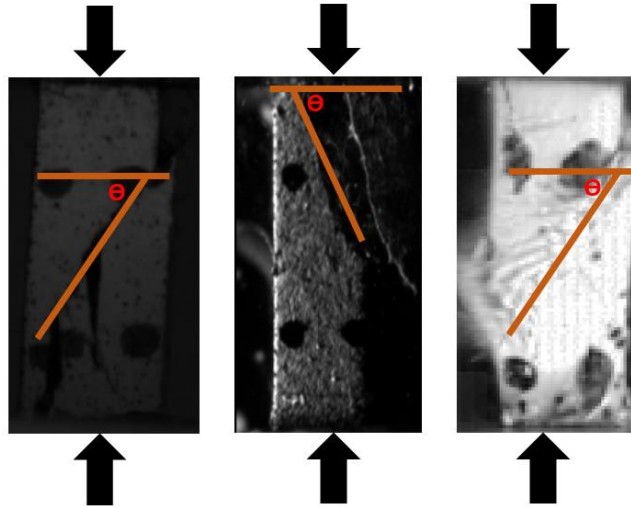


Figure 4-17: Images of failed transverse compression specimens at strain rates:
(a) 0.003 s^{-1} ; (b) 1.2 s^{-1} ; (c) 260 s^{-1} .

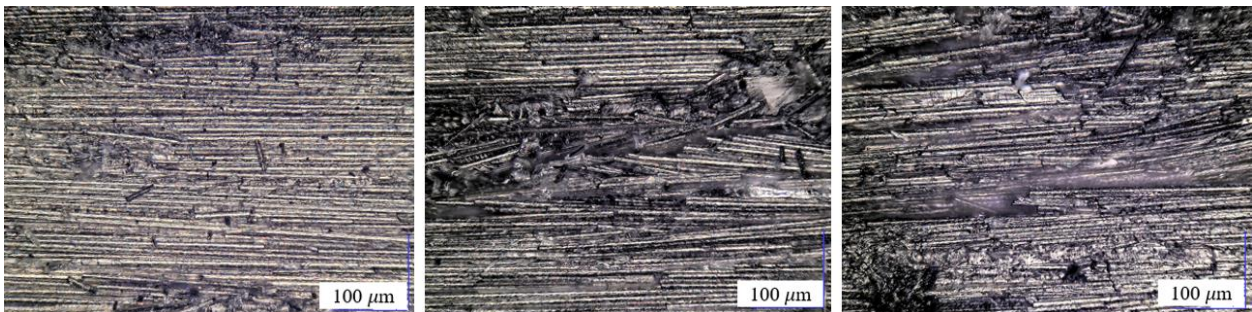


Figure 4-18: Fracture surface images of transverse compression specimens at strain rates: (a) 0.003 s^{-1} ;
(b) 1.2 s^{-1} ; (c) 260 s^{-1} .

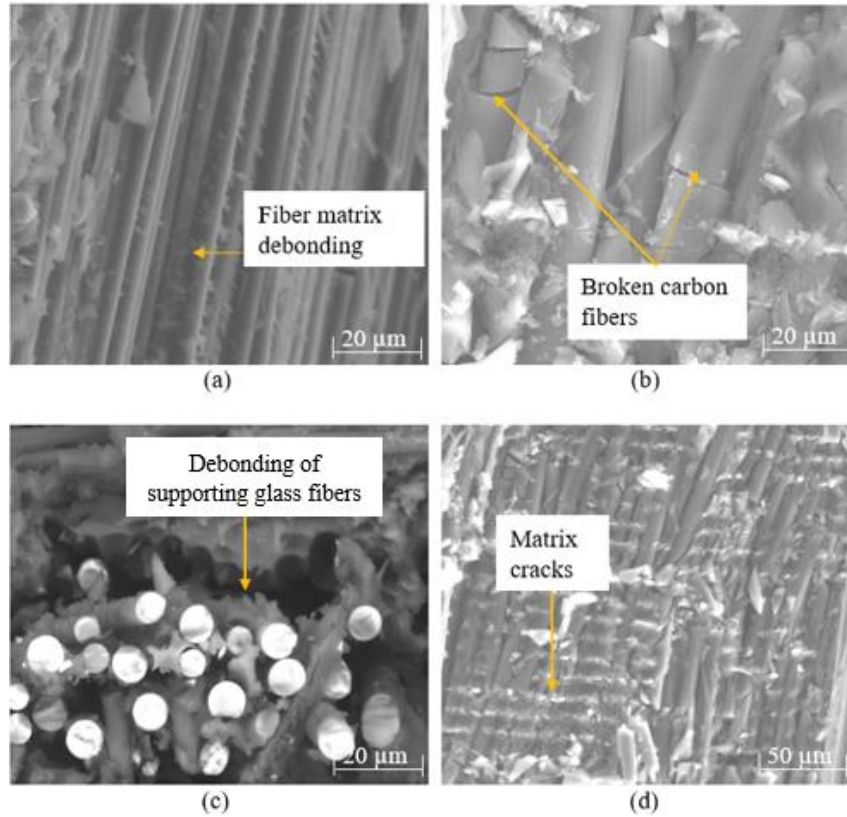


Figure 4-19: Fracture surface images of a transverse compression specimen (taken with a scanning electron microscope) showing different failure modes.

4.2.5 Longitudinal compression testing results

Initial longitudinal compression tests were performed by end loading specimens [175]. However, the specimens failed prematurely at the loaded ends due to brooming and splitting of plies, and the measured strength values were not representative of the actual longitudinal compression strength. A new fixture was designed (**Figure 4-20**) to aid in suppressing premature failure at the specimen ends. The fixture was designed such that it can be used on both the hydraulic test frame and the compression split Hopkinson pressure bar. Both ends of each test specimen were bonded to the fixtures using Loctite[®] 480 adhesive. After bonding a specimen to the fixtures, a height gauge was used to ensure that the parallelism and flatness was within 0.02 mm, which aided in obtaining uniform loading during the test. Each specimen was subsequently speckled with a black-on-white paint pattern to enable capture of strain from the specimen surface. High speed camera (FASTCAM SA-Z, Photron, Tokyo) was used to capture images at frame rates of 125 fps, 2500 fps, and 360,000 fps for the quasi-static, intermediate and high rate tests, respectively. For all tests, cameras were triggered manually before applying the load. Strain measures were obtained by post-

processing images using the GOM Correlate software (GOM, Brunswick). Further details about the test set-up can be found in Appendix B.

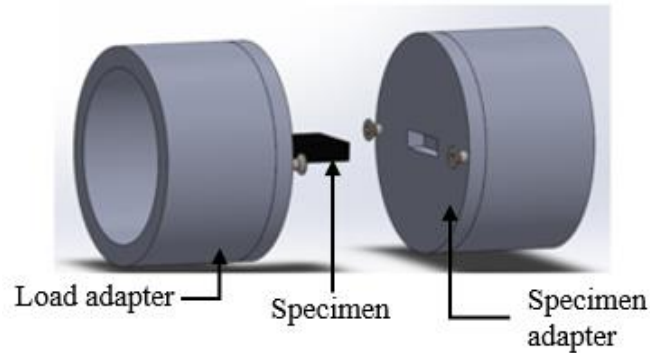


Figure 4-20: Fixture for the longitudinal compression testing.

The stress-strain response of all specimens tested at different rates exhibited a linear behavior until failure (**Figure 4-21**). In general, the results were repeatable, but there was some variability due to the high strength and low strain-to-failure of the UD-NCF composite in longitudinal compression mode, which has been documented in previous studies [18, 68]. For all rates, the strain-to-failure was found to be roughly 1% or less, which is comparable to the findings for carbon fiber/epoxy unidirectional tape composites (UDTCs) [17]. There was an approximately 35% increase in the average ultimate longitudinal compressive strength as the strain rate was increased from 0.001 s^{-1} to 70 s^{-1} (**Figure 4-22**).

The average longitudinal compressive modulus, as measured at different strain rates, was found to be consistent within one standard deviation. Statistical analysis, including one-way ANOVA and Tukey's test with a significance level of $p \leq 0.05$, showed a significant difference between the average longitudinal compressive strength measured at 0.001 s^{-1} and 70 s^{-1} . However, no significant difference was found for the elastic modulus and strain-to-failure measured at different strain rates. To obtain empirical relationships for the average longitudinal compressive strength as a function of strain rate, the data was fitted with a semi-logarithmic expression (**Figure 4-23**). These relationships can be used to interpolate these properties at other strain rates.

The specimens tested at all rates failed away from the loading ends. Tow splitting or brooming was not observed on the specimen ends. The carbon fiber tows in the UD-NCF composites, due to stitching, have small out-of-plane fiber misalignment and are not perfectly straight. This causes UD-NCF composites to fail under less load than UDTCs with straight fibers. A small out-of-plane inclination was observed in

the failed specimens (**Figure 4-24a**), along with evidence of local fiber micro-buckling or fiber kinking (**Figure 4-24b**). Delamination and inter-tow splitting were also seen on the surface of the failed specimens (**Figure 4-24c**). However, it is unclear whether micro-buckling occurred before or after the inter-tow splitting. Nevertheless, the longitudinal compressive failure mode of the studied UD-NCF composite is markedly distinct from that of UDTCs, which typically exhibit the formation of a kink band through the specimen thickness without inter-tow splitting cracks or localized delamination.

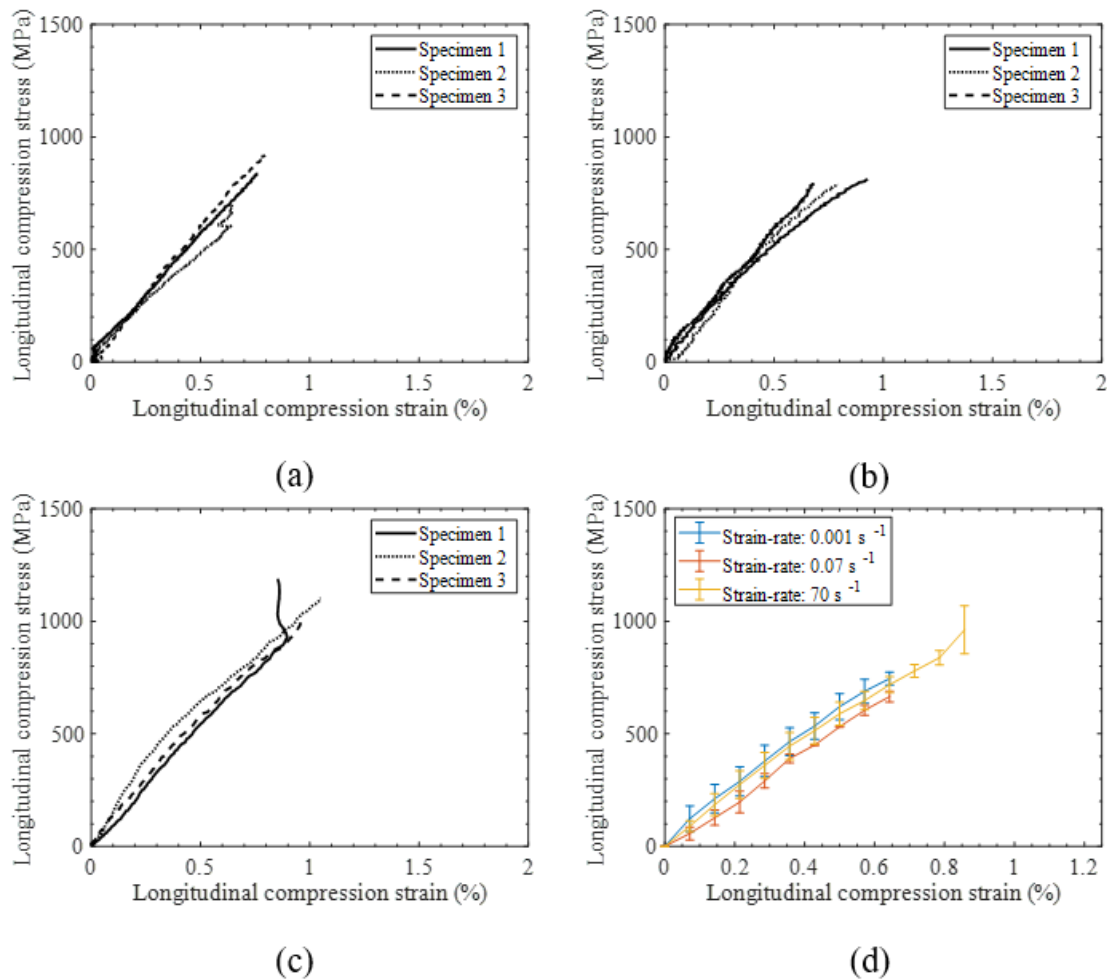


Figure 4-21: Stress-strain plots for longitudinal compression tests performed at strain rates: (a) 0.001 s⁻¹, (b) 0.07 s⁻¹, and (c) 70 s⁻¹. (d) Average stress-strain plots for indicated strain rates with standard error bars.

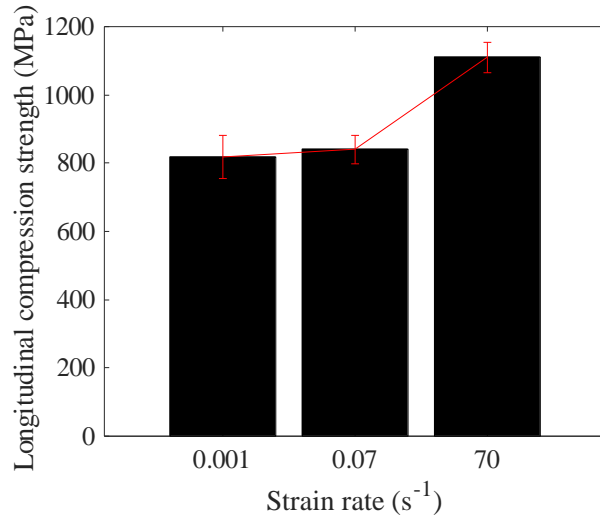


Figure 4-22: Average longitudinal compression strength of the UD-NCF composite for indicated strain rates.

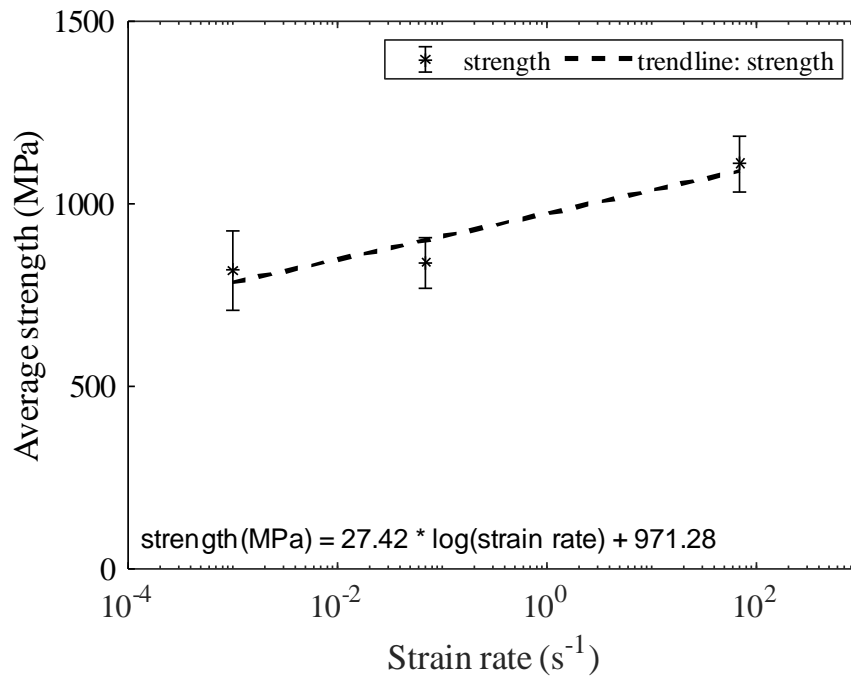


Figure 4-23: Average longitudinal compression strength versus strain rate with regression line and empirical equation shown.

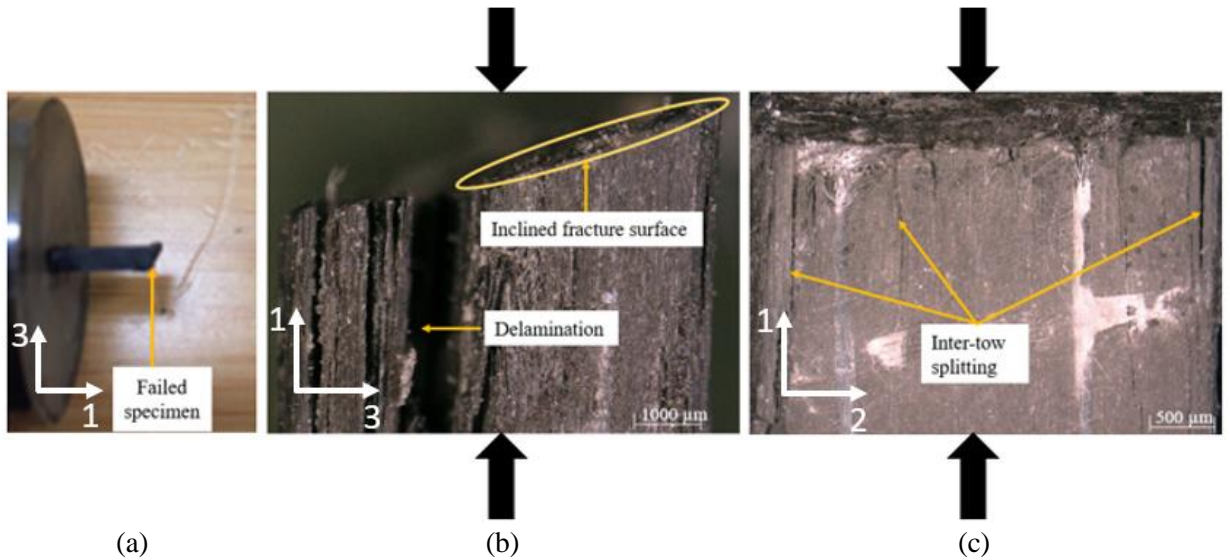


Figure 4-24: Image showing (a) A failed specimen (1-fiber direction, 3-through the thickness transverse direction), (b) Edge view of a failed specimen having inclined fracture surface and delamination, (c) A failed specimen having inter-tow splitting (2-in-plane transverse direction)

4.3 Task 2: Development of a Validated Computational Multiscale Model [Appendix C and Appendix D]

4.3.1 Multiscale modelling for homogenization and failure initiation

A dual-scale computational modelling framework that captures the microstructure of the UD-NCF carbon fiber/snap-cure epoxy composite material at both the micro and mesoscales was developed in Abaqus CAE. Abaqus was chosen for the virtual experimentation since it is more conducive to developing micro/meso-scale models and applying PBCs when compared to LS-DYNA. An initial set of virtual tests was performed for a similar material system with a 45% fiber volume fraction to validate the developed FE-based multiscale modeling framework. Elastic properties and failure initiation for the longitudinal tension and transverse tension modes were predicted in the presence of in-plane fiber misalignment and out-of-plane fiber crimp.

The computationally predicted longitudinal and transverse moduli for the UD-NCF composite material agreed well with available experimental data. This study showed that neglecting the inherent manufacturing-induced defects, namely tow misalignment and crimp, when modeling NCF composites leads to inaccurate predictions, particularly for the longitudinal direction. For the sake of brevity, the details are not included here, and details can be found in Appendix C.

4.3.2 Multiscale modelling framework for strain rate dependent non-linear homogenization

The developed dual-scale computational model was extended to predict the pre-peak inelastic response of a UD-NCF carbon fiber/snap-cure epoxy composite with a 45% fiber volume fraction at different strain rates. The dimensions of the microscale RVE adopted to represent the cross-section of the impregnated unidirectional tow was $57.7 \times 57.7 \mu\text{m}^2$ to accommodate a total of 45 randomly dispersed fibers (**Figure 4-25**). The number of fibers in the RVE was determined from a sensitivity analysis in which different numbers of fibers and fiber dispersions within the RVE were considered. The fiber volume fraction was 55% within the tow and the average fiber diameter was $7.2 \mu\text{m}$, which were equal to that measured through optical microscopy [29]. The RVE was generated using an algorithm based on event-driven molecular dynamics that allows generation of periodic RVEs with non-uniform fiber distribution [176]. After a sensitivity analysis in which the linear elastic response was determined for RVEs with different fiber dispersions and mesh sizes, RVEs having approximately 37,000 reduced integration predominantly hexagonal elements were used for the micro-level analysis. The fibers and matrix were assumed to be perfectly bonded and the interfaces were ignored since they are only important when modelling failure and damage of composite materials, which is not the focus of this study. The meso-scale RVE was composed of homogenized tows and surrounding matrix material. The tow height and width and the thickness of the resin-rich zones within the mesoscale RVE were based on the microscopic measurements that were taken from [29]. After sensitivity studies with different mesh sizes [177], a single tow RVE with 17,577 reduced integration linear hexagonal elements was used for the meso-level simulations (**Figure 4-26**).

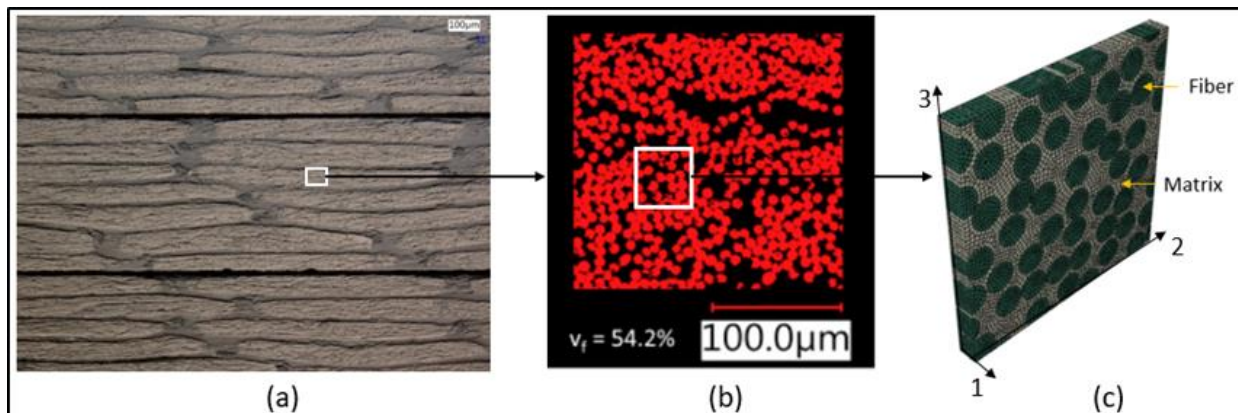


Figure 4-25: (a) Cross-sectional view of the tows of the UD-NCF composite [29], (b) magnified view of a tow showing fibers [29], (c) 3D RVE model for tows (microscale).

The carbon fibers were modelled as transversely isotropic rate-independent linear elastic materials [57]. The longitudinal modulus of the carbon fiber was taken from the PX35 carbon fiber datasheet [178]. The fiber transverse, in-plane shear and out-of-plane shear properties were assumed to be equal to that of AS4 carbon fiber and were taken from Ref. [179] (**Table 4-2**).

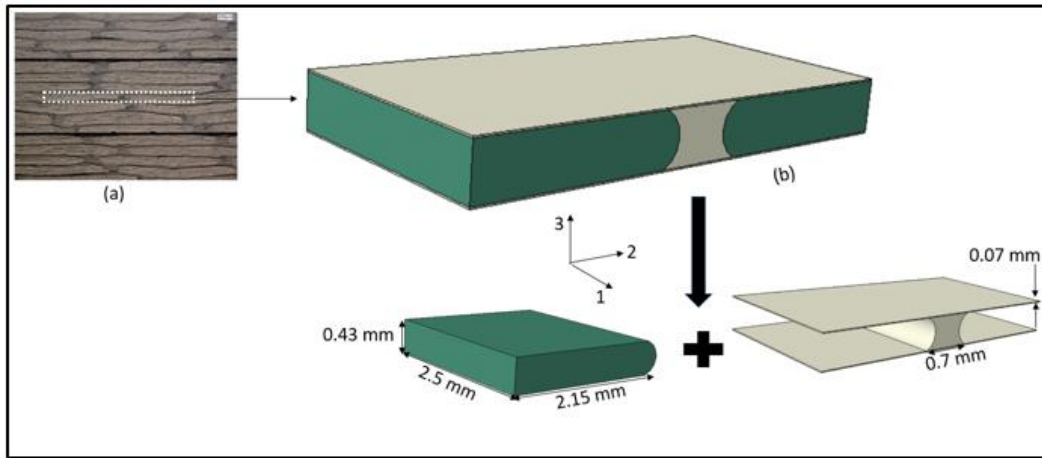


Figure 4-26: (a) Cross-sectional view of the tows of the NCF composite, (b) 3D RVE for the UD-NCF lamina (mesoscale).

Table 4-2: Carbon fiber mechanical properties [178, 179]

Property	E_1 (GPa)	$E_2 = E_3$ (GPa)	$G_{12} = G_{13}$ (GPa)	G_{23} (GPa)	$\nu_{12} = \nu_{13}$	ν_{23}
Value	242	14	28	7.42	0.2	0.25

Table 4-3: Matrix mechanical properties and coefficients [23]

Parameter	E (GPa)	$\sigma_{yt} = \sigma_o$ (MPa)	σ_{yc} (MPa)	ϵ_o (s^{-1})	C	K (MPa)	n
Value	3.2	19.2	30.67	0.0003	0.05	114.6	0.176

The matrix material exhibits tension-compression asymmetry [23] in the yield surface. Several researchers such as Howard *et al.* [180], Boyce *et al.* [181], and Buckley and Jones [182] have developed advanced models for capturing the stress-strain behavior of polymers; however, these models have not been implemented in the commercial software. Also, most of these advanced models require additional experiments beyond uniaxial tension and compression for calibration. The development of a UMAT for polymers and characterizing the epoxy for those models was beyond the scope of this study. Therefore, the

matrix material was modelled using the “Linear Drucker Prager” model [183] available in Abaqus. Therefore, the corresponding yield function is defined by:

$$f = \sqrt{J_2} + AI_1 - B = 0 \quad (29)$$

$$A = \frac{\sigma_{yc} - \sigma_{yt}}{\sqrt{3}(\sigma_{yc} + \sigma_{yt})}, B = \frac{2\sigma_{yc}\sigma_{yt}}{\sqrt{3}(\sigma_{yc} + \sigma_{yt})} \quad (29a)$$

where J_2 and I_1 in Equation (29) denote the second principal invariant of the deviatoric stress tensor and first principal invariant of the Cauchy stress tensor, respectively. σ_{yc} and σ_{yt} in Equation (29a) represent the yield stress in compression and tension, respectively.

Hardening was defined using the “Drucker Prager Hardening” option in Abaqus by the following relation [23]:

$$\bar{\sigma} = \sigma_o + K(\bar{\epsilon}_{pl})^n \quad (30)$$

where $\bar{\sigma}$, σ_o , K , n , and $\bar{\epsilon}_{pl}$ denote the current yield-stress, initial yield stress in tension, strengthening coefficient, power law exponent and effective plastic strain. The values of K , n and σ_o are presented in **Table 4-3**.

The strain rate dependency of the matrix was modelled using the “Johnson-Cook” model [184]. The calibration parameters, reference strain rate (ϵ_o) and strain rate scaling parameter (C), for the model were based on the experimental results [23] (**Table 4-3**).

Impregnated tows in textile composites are commonly modelled as unidirectional composites [40, 71], which are transversely isotropic. In this study, the tows were modelled as an elasto-plastic transversely isotropic material using Hill’s anisotropic yield function [185], which requires the stress-strain behavior of the tows in four different directions (*i.e.* longitudinal tension, transverse tension, in-plane shear, and out-of-plane shear) to define the yield surface parameters (**Table 4-4** and **Table 4-5**). The stress-strain response of the tows was obtained through micro-scale non-linear homogenization (**Figure 4-27**) that was performed by applying displacement-based periodic boundary conditions (PBCs) to the tow RVE. Complete details about implementing the PBCs are available in Appendix C [177]. Johnson-Cook model parameters (**Table 4-6**) for the tows were obtained by simulating the in-plane shear response of the microscale RVE at three strain rates; 0.0001 s^{-1} , 0.01 s^{-1} and 1 s^{-1} , while the Johnson-Cook model parameters for the matrix were taken from [23] (**Table 4-3**).

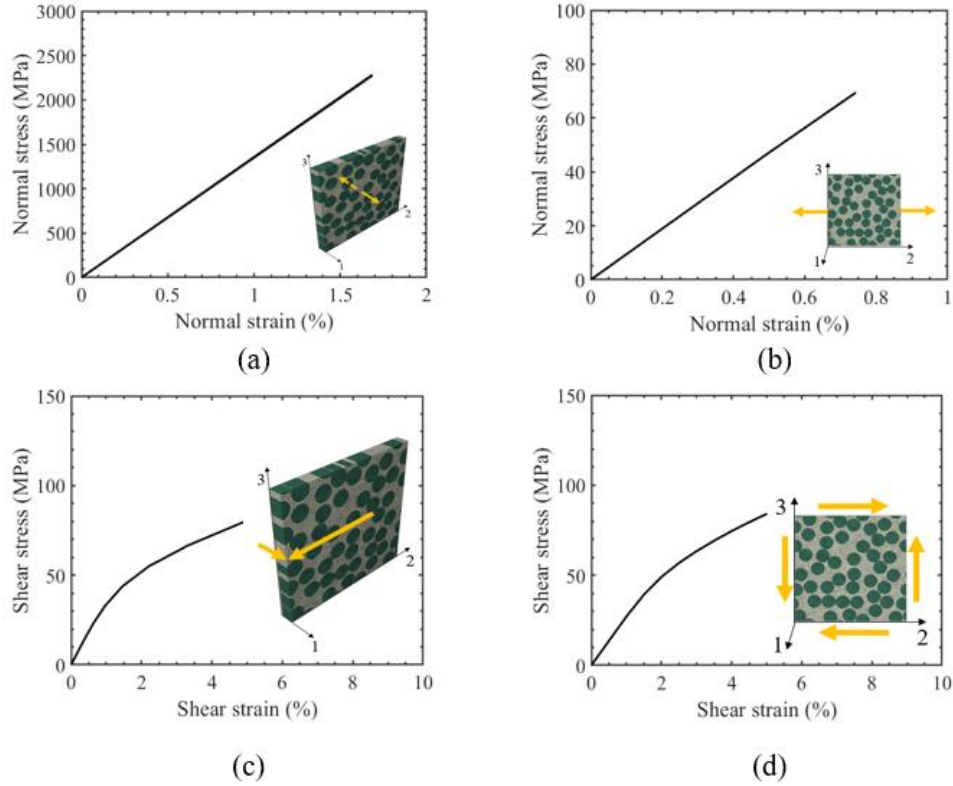


Figure 4-27: Predicted effective stress-strain response of the UD impregnated tow under a quasi-static strain rate (0.0001 s^{-1}) using microscale RVEs: (a) longitudinal tension, (b) transverse tension, (c) in-plane shear, and (d) out-of-plane shear.

It is noted that the effect of adiabatic heating on matrix softening was not considered in this study. A review of the literature reveals that the rise in temperature with strain rate is negligible for UD carbon/epoxy composite materials when loaded along the axial direction [186]. For the transverse and shear modes, the average increase in temperature for FRP composites has been reported to be approximately 9 - 12 °C for strain rates up to 1000 s^{-1} [187, 188, 186], which will not significantly affect the storage modulus of the UD-NCF composite. Furthermore, thermal softening was not observed in the experimental data obtained by Zeng for the same snap-cure epoxy material considered in this study [23].

Table 4-4: Yield stress, taken at zero plastic strain, for the homogenized tows

Parameter	$\bar{\sigma}_{11}$	$\bar{\sigma}_{22} = \bar{\sigma}_{33}$	$\bar{\sigma}_{12} = \bar{\sigma}_{13}$	$\bar{\sigma}_{23}$	$\bar{\sigma}_o$
Value (Mpa)	1643.3	20.8	10.7	9.2	10.7

Table 4-5: Yield stress ratio based on the experimental data (inputs for Hill's anisotropic yield model)

Parameter	R11	R22 = R33	R12 = R13	R23
Value	153.58	1.94	1.73	1.49

Table 4-6: Johnson-Cook model parameters for tow

Parameter	Reference strain rate	C
Value	0.0001 s ⁻¹	0.036

The non-linear homogenized stress-strain response of the UD-NCF carbon fiber/snap-cure epoxy composite at the quasi-static strain rate ($\sim 0.0001 \text{ s}^{-1}$) for longitudinal tension (**Figure 4-28a**), transverse tension (**Figure 4-29a**), in-plane shear (**Figure 4-30a**) and out-of-plane shear (**Figure 4-31a**) loading was predicted by applying PBCs to the mesoscale RVE. The dimensions of the mesoscale RVE and its constituents, and overall fiber volume fraction were defined based on the micrographs (**Figure 4-26**). The sensitivity analysis was performed for multiple tows (not randomly distributed) for the elastic properties; however, no significant difference was observed in the predicted results. Therefore, the final RVE contains a single tow. A very good agreement (within 10%) was observed between the predicted and experimentally measured results [29]. The stress-strain response in the longitudinal direction (**Figure 4-28a**) and transverse direction (**Figure 4-29a**) was predicted to be linear until failure as observed in the experiments. Plastic strains for the longitudinal (**Figure 4-28b**) and transverse modes (**Figure 4-29b**) were found to be small in magnitude. For the longitudinal tension mode, the magnitude of the plastic strain in the matrix region was significantly higher than the plastic strain in the tow, which is probably due to the significant higher initial yield stress of the tow than the matrix for that direction. For the transverse tension mode, the magnitude of the plastic strain in the matrix and tow region were similar that is due to the similar initial yield values for both constituents. Significant non-linearity was observed in the in-plane shear stress-strain (**Figure 4-30a**) and out-of-plane shear stress-strain (**Figure 4-31a**) behavior of the UD-NCF composite, which is attributed to the high plastic strains in both the tow and matrix regions. The magnitude of the out-of-plane shear stress was found lower than the in-plane shear stress at any given applied strain (**Figure 4-32**). The previous studies [80, 189] for the UDTCs have reported the transverse shear stress to be similar or less in magnitude than the in-plane shear stress.

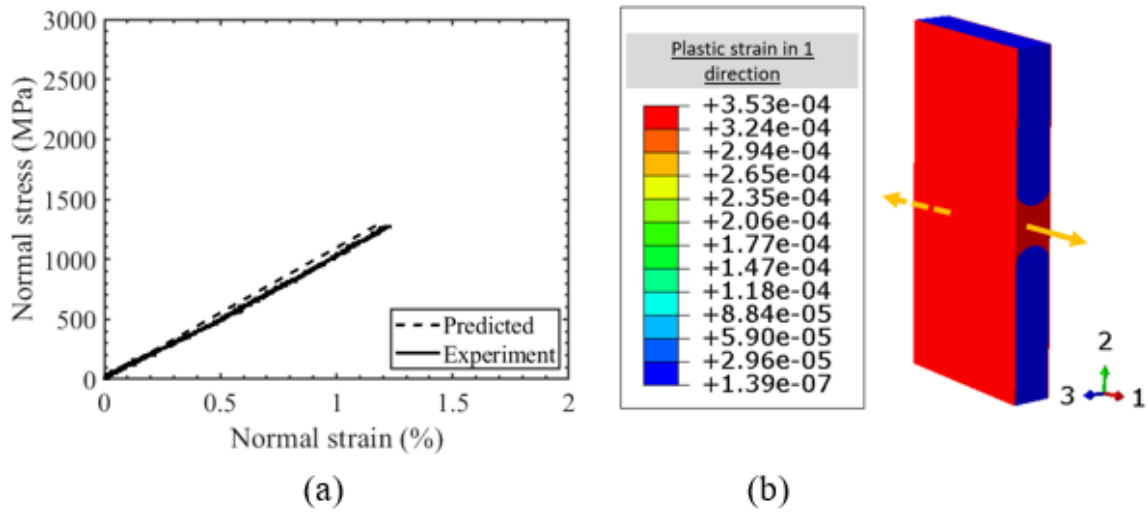


Figure 4-28: Longitudinal tensile response of the UD-NCF composite at quasi-static strain rate: (a) Experimentally measured [25] and predicted stress-strain plot, (b) Contour plot showing plastic strain component for applied strain of 1.2% along the longitudinal direction.

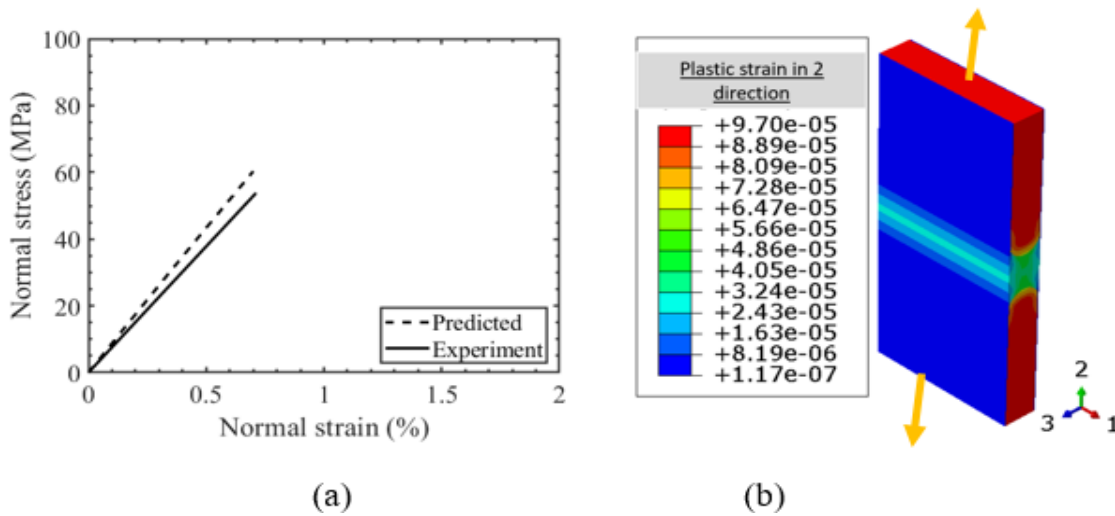


Figure 4-29: Transverse tensile response of the UD-NCF composite at quasi-static strain rate: (a) Experimentally measured [2] and predicted stress-strain plot, (b) Contour plot showing plastic strain component for applied strain of 0.7% along the transverse direction.

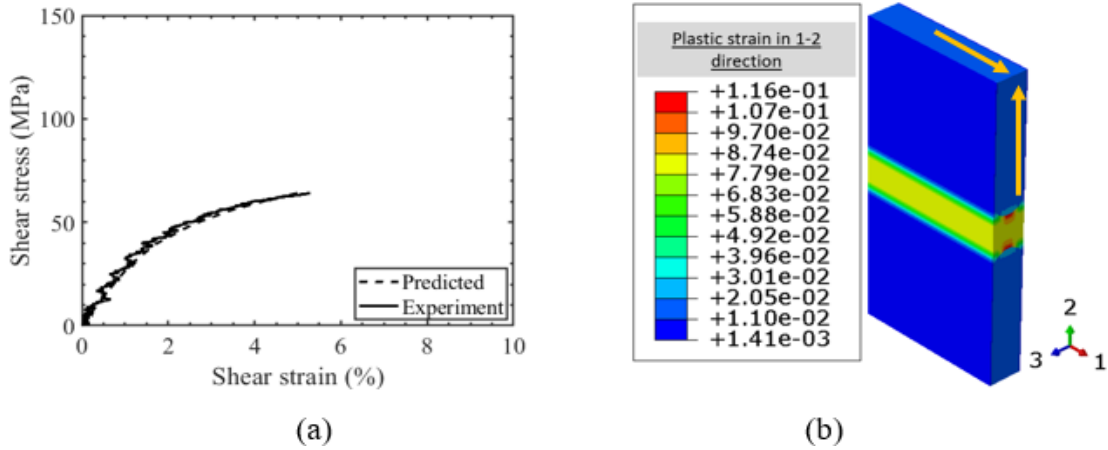


Figure 4-30: In-plane shear response of the UD-NCF composite at quasi-static strain rate: (a) Experimentally measured [2] and predicted stress-strain plot, (b) Contour plot showing plastic strain component for applied strain of 5% in the in-plane shear direction.

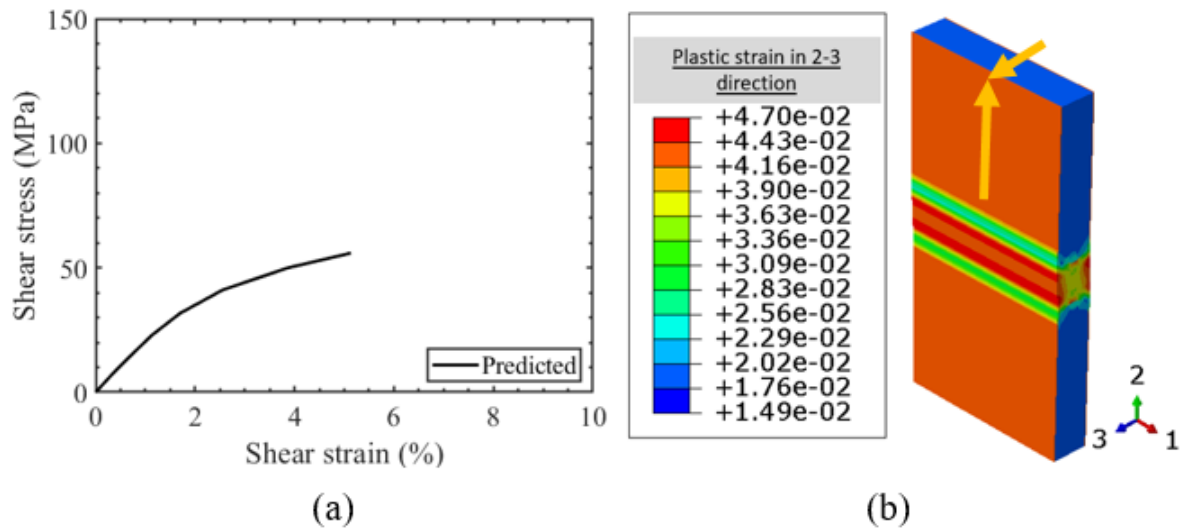


Figure 4-31: Out-of-plane shear response of the UD-NCF composite at quasi-static strain rate: (a) Predicted stress-strain plot, (b) Contour plot showing plastic strain component for applied strain of 5% in the out-of-plane shear direction.

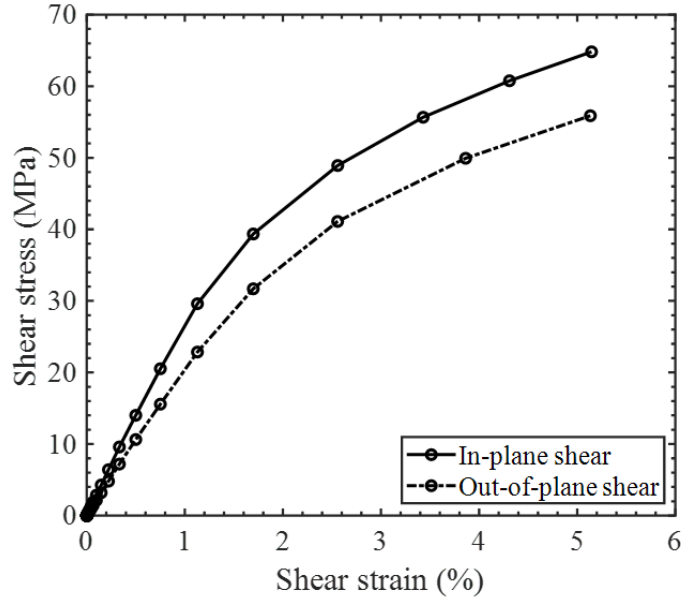


Figure 4-32: Comparison of the in-plane and out-of-plane shear response obtained from the two-scale modelling for the UD-NCF composite.

The effective stress-strain response of the UD-NCF composite under different strain rates ranging from 0.0003 s^{-1} to 550 s^{-1} was predicted for the in-plane shear and out-of-plane shear modes (**Figure 4-33** and **Figure 4-35**). The results showed that the post-yield stress-strain response increased with an increase in strain rate for both in-plane and out-of-plane shear modes. The magnitude of local plastic strains was found to decrease with an increase in strain rate as can be seen in the predicted contour plots (**Figure 4-34** and **Figure 4-36**). The predicted and experimentally [29] (**Figure 4-37**) measured in-plane shear stress-strain response showed good agreement at a strain rate of 550 s^{-1} up until an applied strain of 3%. Beyond 3% applied strain, the predicted stress-strain response was underestimated with a deviation of approximately 10% at 5% applied strain. The discrepancy in the predicted and experimental in-plane shear stress-strain response may be due to the neglect of the effect of strain rate on the elastic modulus of the matrix material, which was found to have a slight positive strain rate dependency in tension. Additionally, the study used Hill's anisotropic yield function to capture the inelastic response of the homogenized tow in the mesoscale RVE, which did not account for the tension-compression asymmetry of the yield surface for the tow. Despite these limitations, the predicted response is considered reasonable based on these assumptions.

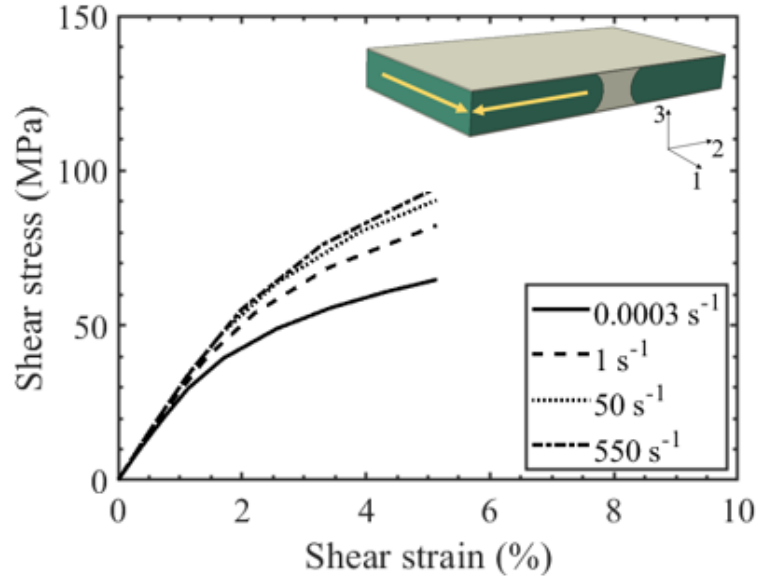


Figure 4-33: Predicted effective in-plane shear stress-strain response for UD-NCF composite at various strain rates.

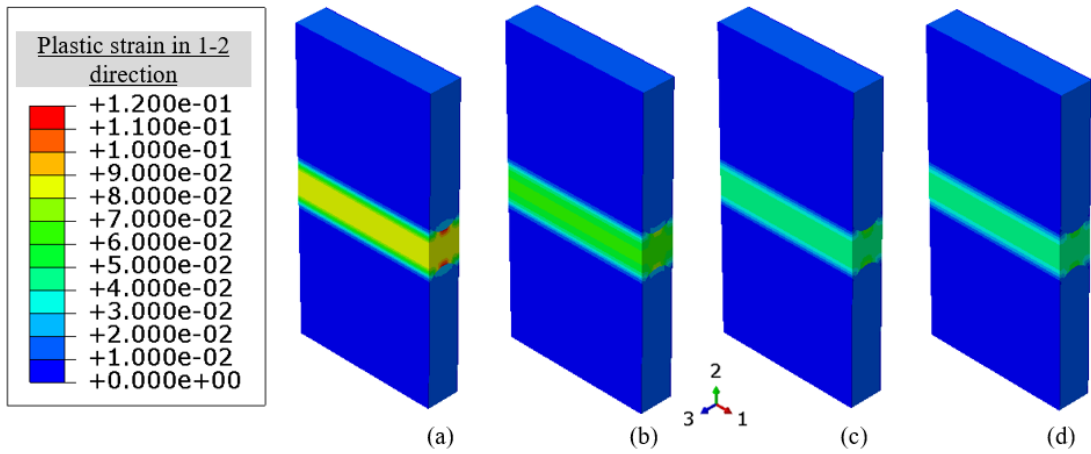


Figure 4-34: Contour plots showing in-plane shear plastic strain component for applied shear strain of 5% at strain rates of: (a) 0.0003 s^{-1} , (b) 1 s^{-1} , (c) 50 s^{-1} and (d) 550 s^{-1} .

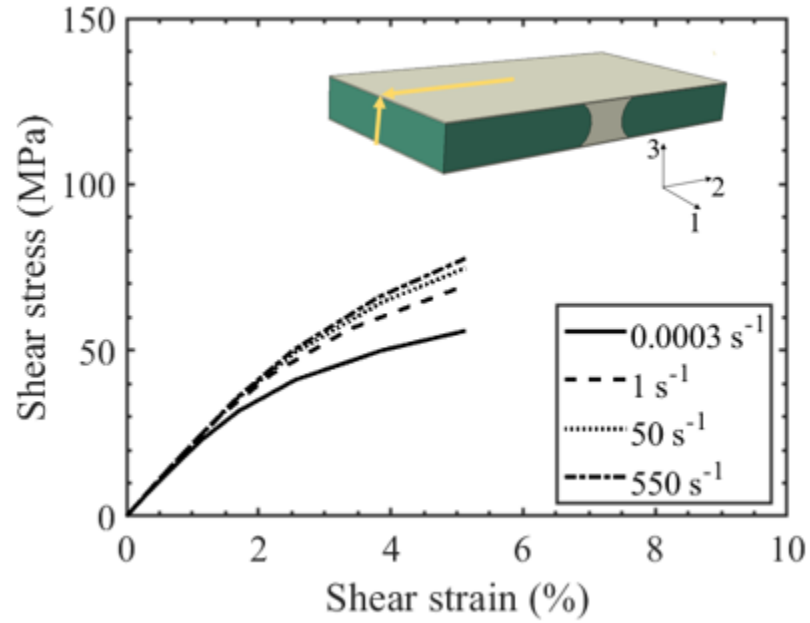


Figure 4-35: Predicted effective out-of-plane shear stress-strain response of UD-NCF composite at various strain rates.

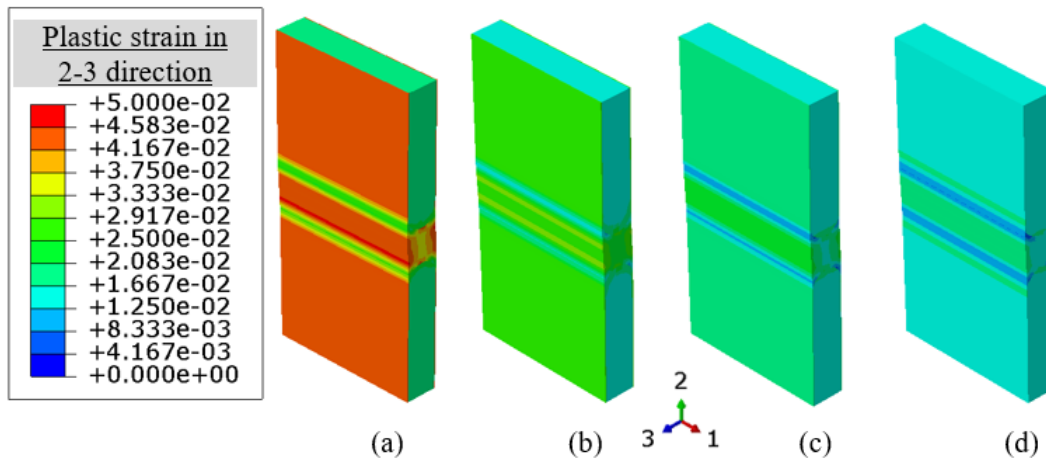


Figure 4-36: Contour plots showing out-of-plane plastic strain component for applied shear strain of 5% at strain rates of: (a) 0.0003 s^{-1} , (b) 1 s^{-1} , (c) 50 s^{-1} , and (d) 550 s^{-1} .

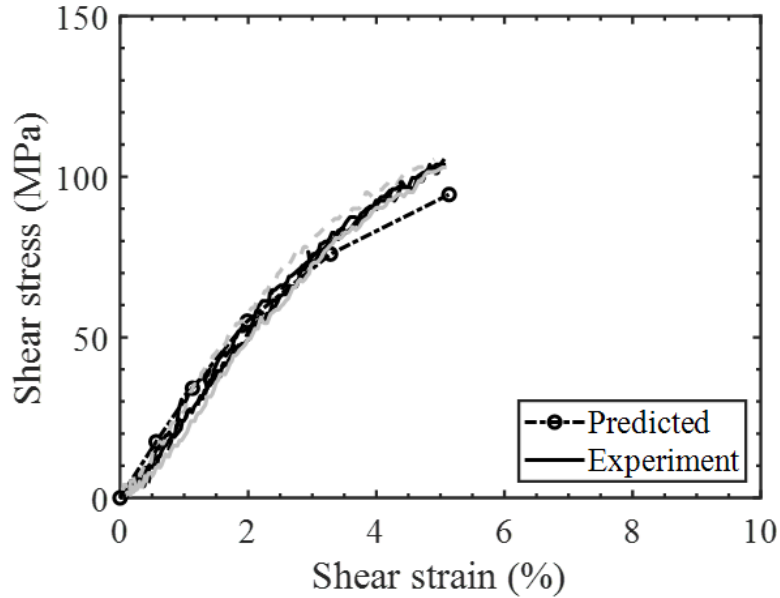


Figure 4-37: Comparison of the predicted and experimentally measured [29] In-plane shear stress-strain response at 550 s^{-1} .

4.4 Task 3: Development of a Validated Strain Rate-Dependent Constitutive Model [Appendix E]

4.4.1 Theoretical development and implementation of an elasto-plastic deformation model

The current research work focused on developing a constitutive model that captures the strain rate-dependent pre-peak deformation response of the UD-NCF composite. The nonlinear response was captured using a plasticity model; thus, the mechanisms that contribute to this response, including local damage and plastic deformation of the matrix, were not explicitly considered. Note, the inclusion of a pre-peak damage within the constitutive model would require calibration of damage parameters using data from loading-unloading experiments, which would be difficult to achieve for dynamic tests on hydraulic test frames or a conventional SHPB setup. The proposed constitutive model assumes an additive decomposition of the strain into elastic strain, inelastic strain and fracture strain [11, 12, 125] (**Figure 4-38**). The UD-NCF composite is treated as a transversely isotropic material and the constitutive equations for the elastic-inelastic response are established by following the mathematical framework of the invariant formulation for the transversely isotropic materials [125, 190, 191]. A structural tensor is used in the invariant formulation as an argument of the constitutive equation, which reflects material symmetries [192]. The structural tensor is obtained by the dyadic product of the preferred direction vector that depends on anisotropic nature (transversely isotropic, orthotropic etc.) of the material. The preferred direction for a transversely isotropic UD composite

is $[1, 0, 0]$ (**Figure 2-8 b**) because the plane perpendicular to this vector is isotropic and physical properties are symmetric about it.

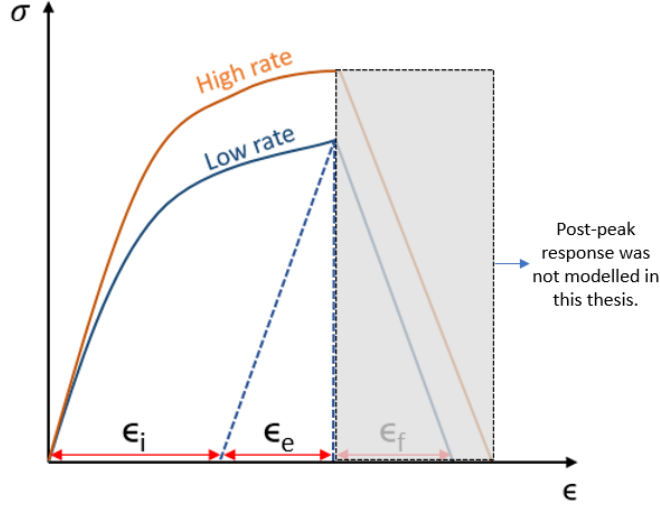


Figure 4-38: Schematic stress-strain plot demonstrating the additive split of strain (ϵ^i , ϵ^e and ϵ^f represent the inelastic, elastic and fracture strains, respectively) and the influence of strain rate.

The elastic free energy in terms of strain and the structural tensor for a transversely isotropic material is defined as [193]:

$$\psi(\underline{\epsilon}, \dot{\underline{\epsilon}}, \underline{A}) = \frac{1}{2}\lambda(\text{tr}\underline{\epsilon})^2 + \mu_T \text{tr}(\underline{\epsilon})^2 + \alpha(\tilde{a}\underline{\epsilon}\tilde{a})\text{tr}\underline{\epsilon} + 2(\mu_L - \mu_T)(\tilde{a}\underline{\epsilon}^2\tilde{a}) + \frac{1}{2}\beta(\tilde{a}\underline{\epsilon}\tilde{a})^2 \quad (31)$$

where $\underline{\epsilon}$ and \underline{A} represent the strain and the structural second order tensors, respectively, and λ , μ_T , μ_L , α and β are the scalar invariant coefficients. \tilde{a} is the preferred direction (a vector quantity along the fiber direction in this case).

Taking the first derivative of the elastic free energy with respect to the strain yields the stress as a function of the strain and structural tensor:

$$\underline{\sigma}(\underline{\epsilon}, \dot{\underline{\epsilon}}, \underline{A}) = \lambda(\text{tr}\underline{\epsilon})\underline{I} + 2\mu_T\underline{\epsilon} + \alpha(\tilde{a}\underline{\epsilon}\tilde{a} + \text{tr}\underline{\epsilon}\underline{A}) + 2(\mu_L - \mu_T)(\underline{A}\underline{\epsilon} + \underline{\epsilon}\underline{A}) + \beta(\tilde{a}\underline{\epsilon}\tilde{a})\underline{A} \quad (32)$$

where \underline{I} represents the second order identity tensor.

By taking the second derivative of the elastic free energy with respect to the strain, the elasticity tensor, \mathbf{C} (a fourth order tensor), for a transversely isotropic material can be written in the form of invariants as:

$$\mathbf{C}(\underline{\epsilon}) = \lambda\underline{I}\otimes\underline{I} + 2\mu_T\underline{I} + \alpha(\underline{A}\otimes\underline{I} + \underline{I}\otimes\underline{A}) + 2(\mu_L - \mu_T)\underline{I}_A + \beta\underline{A}\otimes\underline{A} \quad (33)$$

where $\mathbf{I}_A = A_{im}\mathbf{I}_{jmkl} + A_{jm}\mathbf{I}_{mikl}$, and \mathbf{I} is the fourth order identity tensor.

The yield function, modified from [125], is defined as:

$$f(\underline{\sigma}, \bar{\varepsilon}^p, \dot{\varepsilon}, \underline{A}) = \alpha_1 I_1 + \alpha_2 I_2 + \alpha_3 I_3 - 1 \leq 0 \quad (34)$$

Here, \underline{A} and $\bar{\varepsilon}^p$ denote the structural tensor obtained by the dyadic product of the vector in the fiber direction and the effective plastic strain, respectively. I_i and α_i ($I = 1,2,3$) denote the normal plane stress invariants for a transversely isotropic material and yield stress parameters, respectively, and are defined by:

$$I_1 = \frac{1}{2}(\text{tr}\underline{\sigma}^{pind})^2 - \text{tr}\underline{A}(\underline{\sigma}^{pind})^2 \quad (35)$$

$$I_2 = \text{tr}\underline{A}(\underline{\sigma}^{pind})^2 \quad (36)$$

$$I_3 = \frac{1}{2}(\text{tr}\underline{\sigma}) - \text{tr}\underline{A}(\underline{\sigma}) \quad (37)$$

$$\alpha_1 = 1/Y_{TS}^2, \alpha_2 = 1/Y_{IS}^2, \alpha_3 = \frac{1}{Y_{UT}} - \frac{1}{Y_{UC}} \quad (38)$$

Here, Y_{TS} , Y_{IS} , Y_{UT} , and Y_{UC} represent the yield stresses in the transverse shear, in-plane shear, transverse tension, and transverse compression directions, respectively, which are functions of the effective plastic strains. $\underline{\sigma}^{pind}$ contains stress components responsible for inducing plasticity.

Plastic potential function, $g(\underline{\sigma}, \underline{A})$, takes only the quadratic terms of the stress, and it reads as:

$$g(\underline{\sigma}, \underline{A}) = \beta_1 I_1 + \beta_2 I_2 \quad (39)$$

The definitions of the β_1 and β_2 are adopted from [191] which are defined as below:

$$\beta_1 = 1 \quad (40)$$

$$\beta_2 = \frac{\varepsilon_{12}^p}{\varepsilon_{23}^p} \quad (41)$$

It has been revealed by the experimental results [41, 194] that the elastic and inelastic response of UD composites is strain rate-dependent for some modes. The strain rate-dependency of carbon fiber-reinforced UD composites is negligible for the deformation response along the fiber direction [17]; however, the transverse and shear deformation responses exhibit significant positive strain rate-dependency. Therefore, the strain rate dependency for these two modes is modelled using four scaling functions which are defined below:

$$S_{T_E}(\dot{\epsilon}) = \left(1 + C_{E_{22}} \ln\left(\frac{\dot{\epsilon}}{\dot{\epsilon}_{ref}}\right)\right) \quad (42)$$

$$S_{S_E}(\dot{\epsilon}) = \left(1 + C_{G_{12}} \ln\left(\frac{\dot{\epsilon}}{\dot{\epsilon}_{ref}}\right)\right) \quad (43)$$

$$S_{T_Y}(\dot{\epsilon}) = \left(1 + C_{T_Y} \ln\left(\frac{\dot{\epsilon}}{\dot{\epsilon}_{ref}}\right)\right) \quad (44)$$

$$S_{S_Y}(\dot{\epsilon}) = \left(1 + C_{S_Y} \ln\left(\frac{\dot{\epsilon}}{\dot{\epsilon}_{ref}}\right)\right) \quad (45)$$

Here, $\dot{\epsilon}_{ref}$ and $\dot{\epsilon}$ denote the reference and current strain rates, respectively. $S_{T_E}(\dot{\epsilon})$, $S_{S_E}(\dot{\epsilon})$, $S_{T_Y}(\dot{\epsilon})$ and $S_{S_Y}(\dot{\epsilon})$ represents the scaling functions for the transverse elastic modulus, shear modulus, transverse yield stress and shear yield stress, respectively. $C_{E_{22}}$, $C_{G_{12}}$, C_{T_Y} and C_{S_Y} are the material constants for the transverse elastic modulus, shear modulus, transverse yield stress and shear yield stress, respectively.

The constitutive equations of the material model were solved numerically by discretizing in time at Gauss-point level within FE framework. Time integration is performed using the backward Euler integration scheme, following a methodology proposed by Eidel [195]. A user defined material model is developed in FORTRAN and implemented in LS-DYNA (Explicit) for the verification and validation of the material model. **Figure 4-39** presents the algorithm flowchart for predicting the strain rate-dependent elastic-inelastic response of the UD-NCF composite.

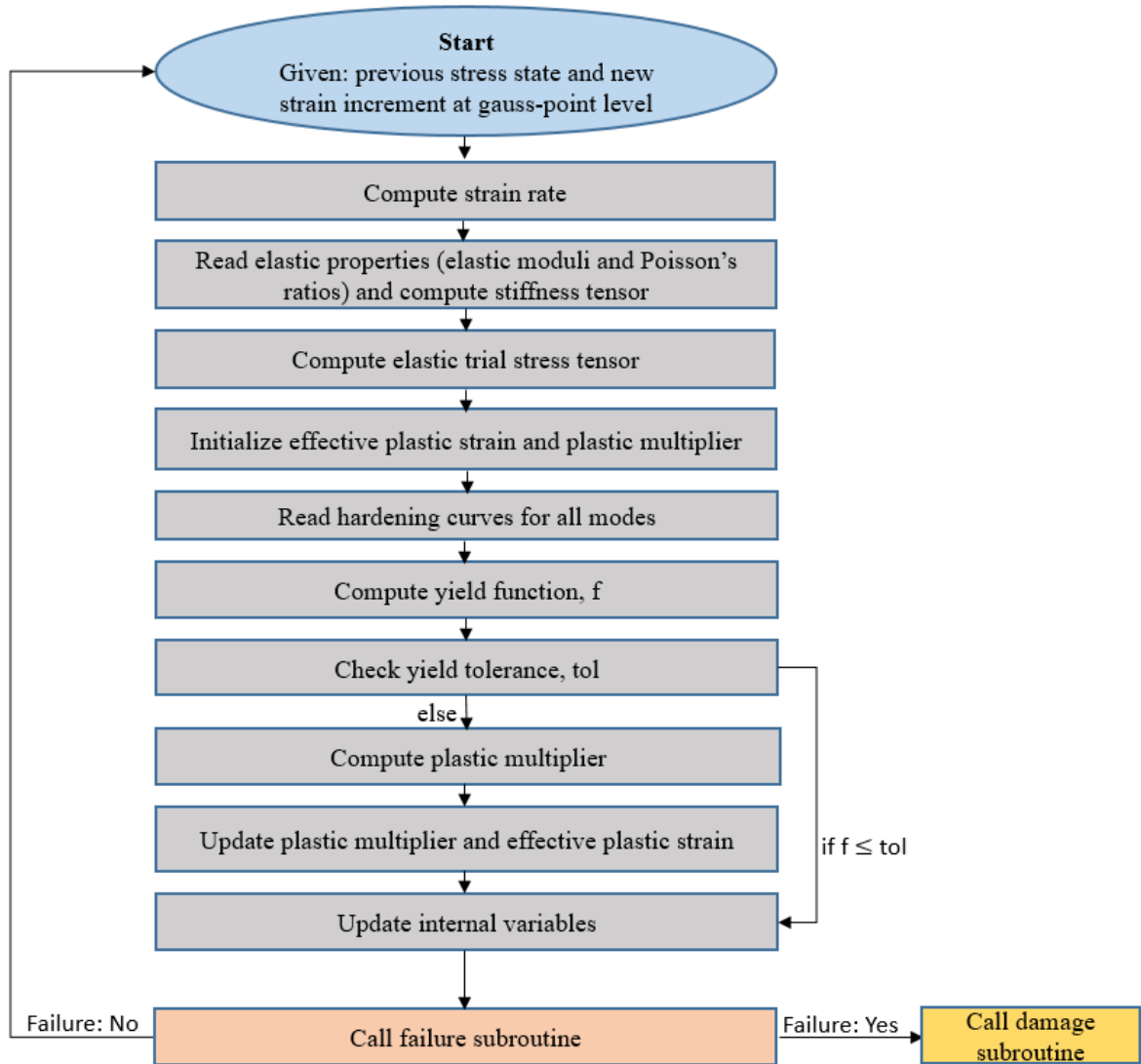


Figure 4-39: Flowchart of VUMAT Subroutine

4.4.2 Material model calibration, verification, and validation for UD-NCF composite

The complete calibration of the material model requires five elastic constants, four strain rate parameters, four hardening curves, and one plastic potential parameter. The elastic constants (E_{11} , E_{22} , G_{12} , G_{23} , ν_{12}), strain rate parameters ($C_{E_{22}}$, $C_{G_{12}}$, C_{T_Y} , C_{S_Y}) (Table 4-7), and hardening curves (in-plane shear and transverse compression (Figure 4-40) were taken from [194, 171]. The previous micromechanical based study (Figure 4-32) for the UD-NCF composite [196] have shown that the transverse shear stress is slightly lower in magnitude than the in-plane shear stress. Therefore, the transverse shear response was obtained by scaling down the in-plane shear response by a factor of 0.95.

Table 4-7: Input parameters for the material model for UD-NCF composite material

Parameter type	Parameter	Values
Elastic parameters	E_{11} [171]	120 GPa
	E_{22} [194]	8.6 GPa
	ν_{12} [194]	0.37
	G_{12} [194]	3.4 GPa
	G_{23} [196]	3.2 GPa
Plastic potential parameter	$\beta 2 \left(\frac{\epsilon_{12p}}{\epsilon_{23p}} \right)$ [197]	1
Strain rate parameters	$\dot{\epsilon}_{ref}$	0.000003 ms ⁻¹
	$C_{E_{22}}$ [194]	0.04
	$C_{G_{12/23}}$ [194]	0.02
	C_{T_Y} [194]	0.10
	C_{S_Y} [194]	0.11
Density	ρ [171]	0.00125 g.mm ⁻³

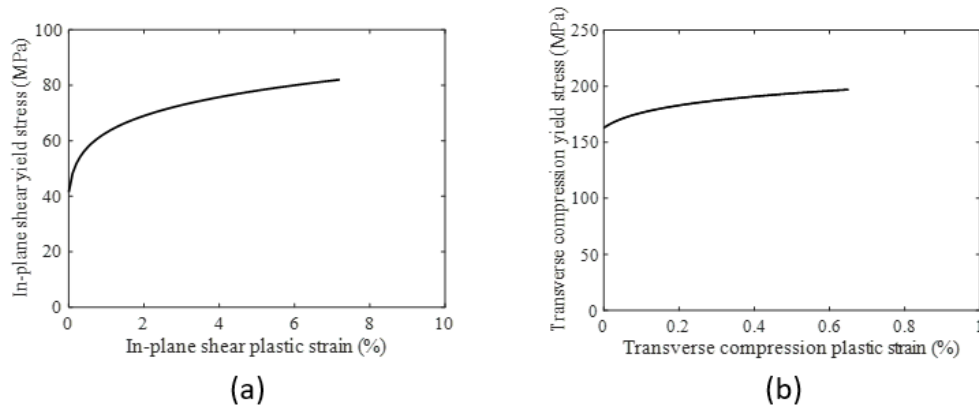


Figure 4-40: Hardening curves for: (a) In-plane shear, (b) Transverse compression.

4.4.3 Material model verification for UD-NCF composite

To check the implementation of the material model, single element tests were performed for different deformation modes in LS-DYNA, including transverse tension, transverse compression, in-plane shear, out-of-plane shear, longitudinal tension, and longitudinal compression. A fully integrated shell element (ELMFORM 16) was used in all cases.

For the transverse tension mode (**Figure 4-41a**), the single element tests were performed at 0.1 s^{-1} , 16 s^{-1} and 126 s^{-1} strain rates by applying displacements for strains up to 1%. The simulated stress-strain response (**Figure 4-42**) for all rates was found to be linear until failure. A good agreement was observed between the simulated and experimental results for the transverse tension mode.

For the transverse compression mode (**Figure 4-41b**), single element tests were performed at 0.003 s^{-1} , 1.4 s^{-1} and 260 s^{-1} by applying displacements for strains up to 3.5%. The simulated stress-strain response at all strain rates was found to be linear (**Figure 4-43**) initially followed by some non-linearity. A very agreement was observed between the simulated and experimental results for the results obtained at 0.003 s^{-1} and 1.4 s^{-1} strain rate tests. However, some discrepancy was observed between the simulated and experimental results at the high rate (**Figure 4-43c**).

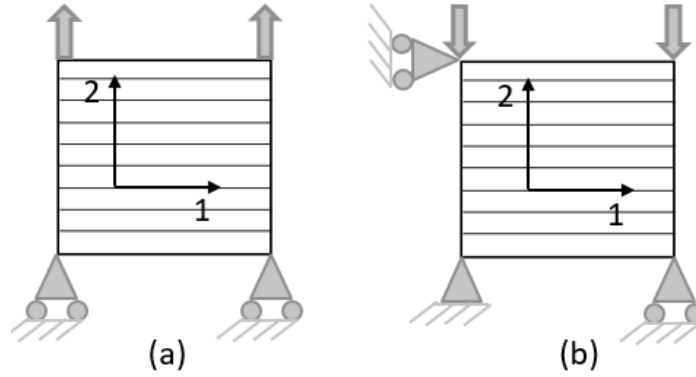


Figure 4-41: Boundary conditions for the single element tests: (a) Transverse tension, (b) Transverse compression (1 represents the fiber direction).

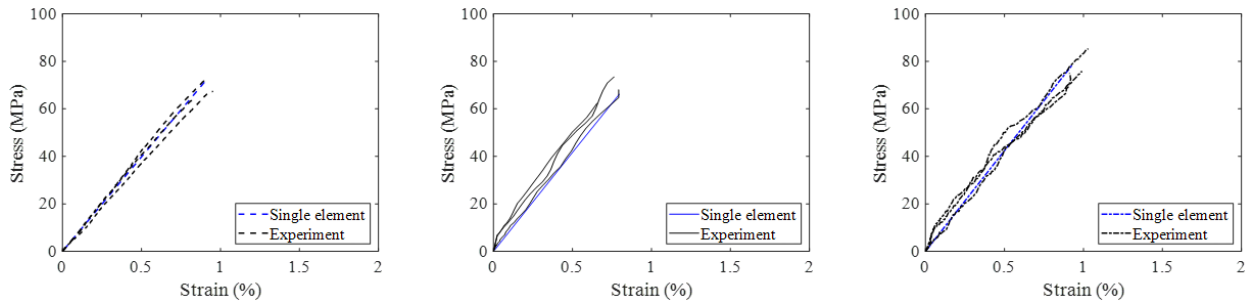


Figure 4-42: Comparison of the single element and experiment [194] test results for the transverse tension mode at strain rate of: (a) 0.1 s^{-1} , (b) 16 s^{-1} and (c) 126 s^{-1} .

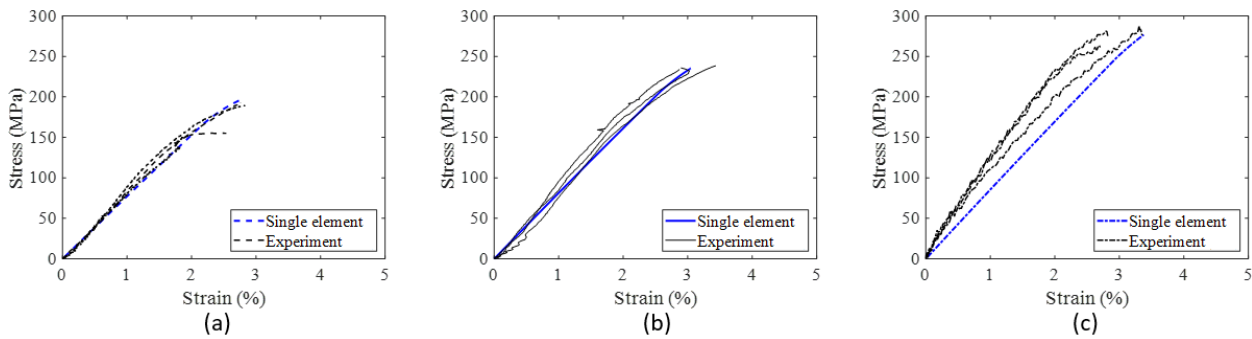


Figure 4-43: Comparison of the single element and experiment [194] test results for the transverse compression mode at strain rate of: (a) 0.003 s^{-1} , (b) 1.4 s^{-1} and (c) 260 s^{-1} .

Single element tests for the in-plane shear and out-of-plane shear modes were performed by constraining two nodes and applying displacement to the other two nodes (**Figure 4-44**) for strains up to 10%. For the in-plane shear mode, the single element tests were performed at 0.003 s^{-1} , 1.8 s^{-1} and 315 s^{-1} strain rates. The simulated stress-strain response at all strain rates was found to be linear initially followed by some softening as was observed in the experiments (**Figure 4-45**). The simulated and experimental stress-strain results (**Figure 4-45**) were found to be in a very good agreement. For the out-of-plane shear mode, single element test was performed at the quasi-static strain rate only, and a very good agreement was observed between the predicted and experimental results (**Figure 4-46**) as well.

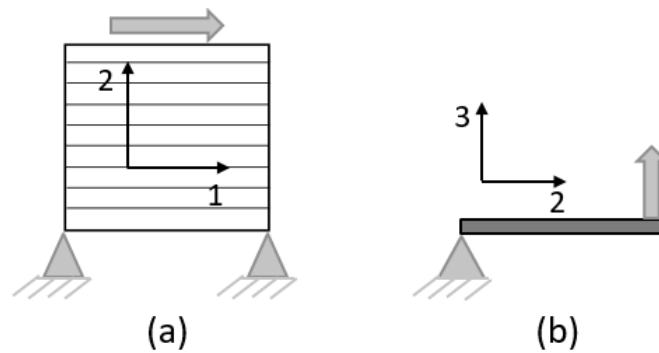


Figure 4-44: Boundary conditions for the single element tests: (a) In-plane shear, (b) Transverse

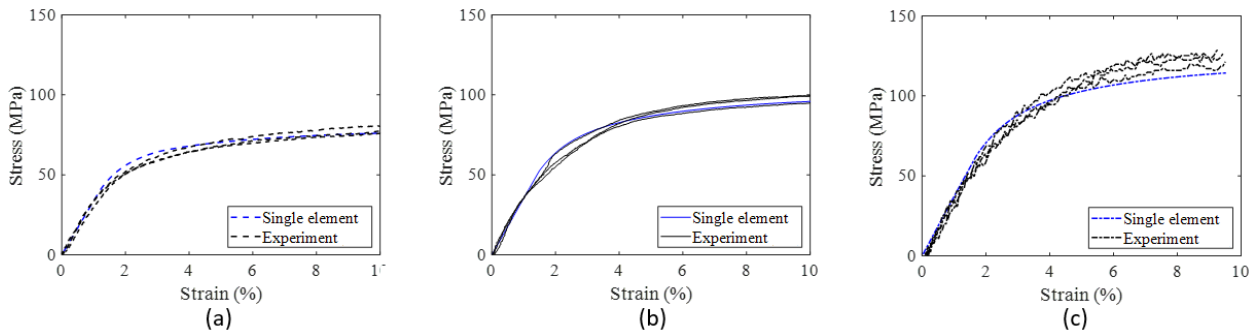


Figure 4-45: Comparison of the single element and experiment [194] test results for the in-plane shear mode at strain rate of: (a) 0.003 s^{-1} , (b) 1.8 s^{-1} and (c) 315 s^{-1} .

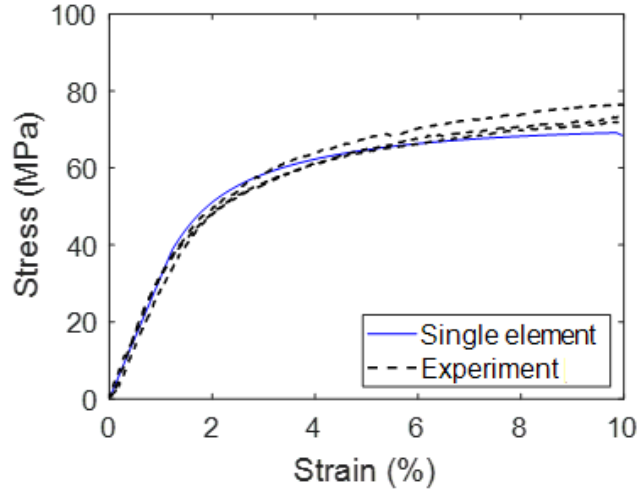


Figure 4-46: Comparison of the single element and scaled experiment [194] test results for the out-of-plane shear mode at strain rate of 0.003 s^{-1} .

Single element tests for the longitudinal tension (**Figure 4-47a**) and compression (**Figure 4-47b**) modes was performed at the quasi-static strain rate (0.001 s^{-1}) only since the pre-peak stress-strain (deformation) behavior for these modes is strain rate-independent [194]. For both modes (**Figure 4-48**), the simulated response was linear up to the failure strain as was observed in the experiments. A very good agreement was seen between the experimental and simulated results.

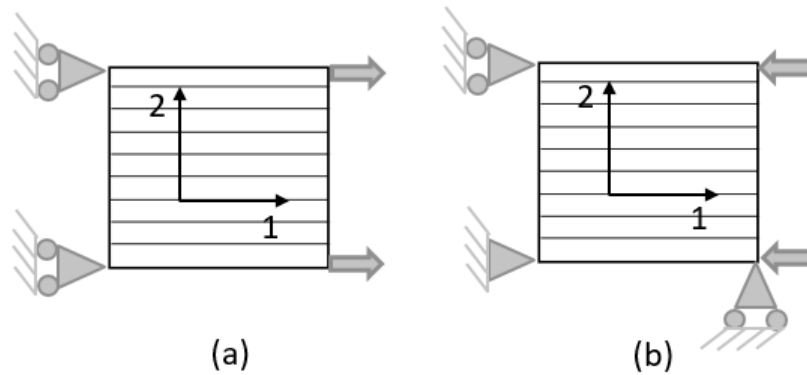


Figure 4-47: Boundary conditions for the single element tests: (a) Longitudinal tension, (b) Longitudinal compression (1 represents the fiber direction).

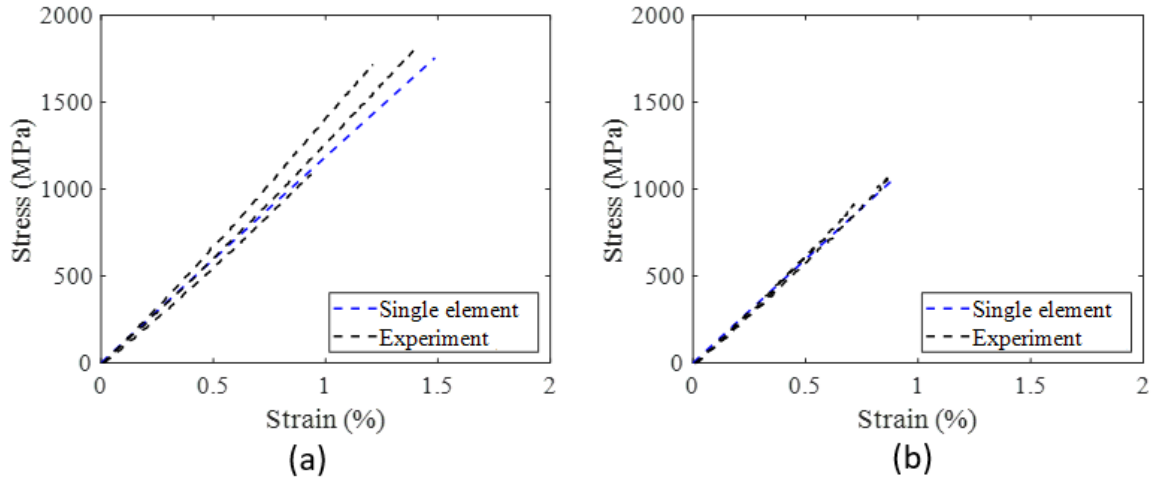


Figure 4-48: Comparison of the single element and experiment [171] test results at 0.001 s^{-1} strain rate for: (a) Longitudinal tension, (b) Longitudinal compression.

4.4.3.1 Material model validation for UD-NCF composite

The material model was validated by subjecting an angle ply laminate ($[\pm 45^\circ]_{2s}$) to the axial compression loading at the quasi-static (0.001 s^{-1}) and high (315 s^{-1}) strain rates (**Figure 4-49**). The predicted and experimental results for the quasi-static tests were found to be in an excellent agreement for both the elastic and post-yield response (**Figure 4-51a**). For the high rate simulation results, significant oscillation was observed in stress-strain response that was mitigated by using a transient velocity curve (**Figure 4-50**). The transient velocity curve almost removed the oscillations by providing enough time to the finite element to reach the required velocity. Overall, the experimental and predicted results were found to be in very good agreement for the high rate as well (**Figure 4-51b**).

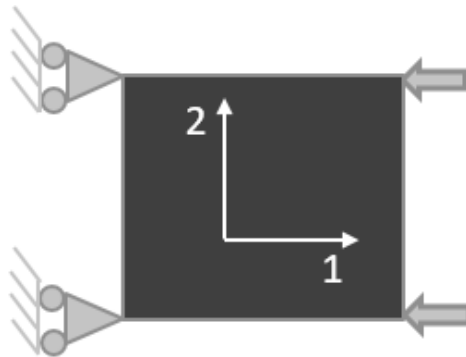


Figure 4-49: Boundary conditions for the single element tests for the first stage validation.

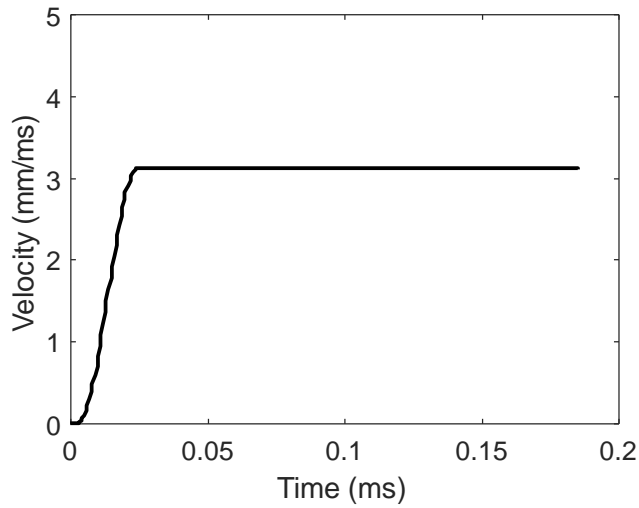


Figure 4-50: Transient velocity curve used for the simulations at high strain rates.

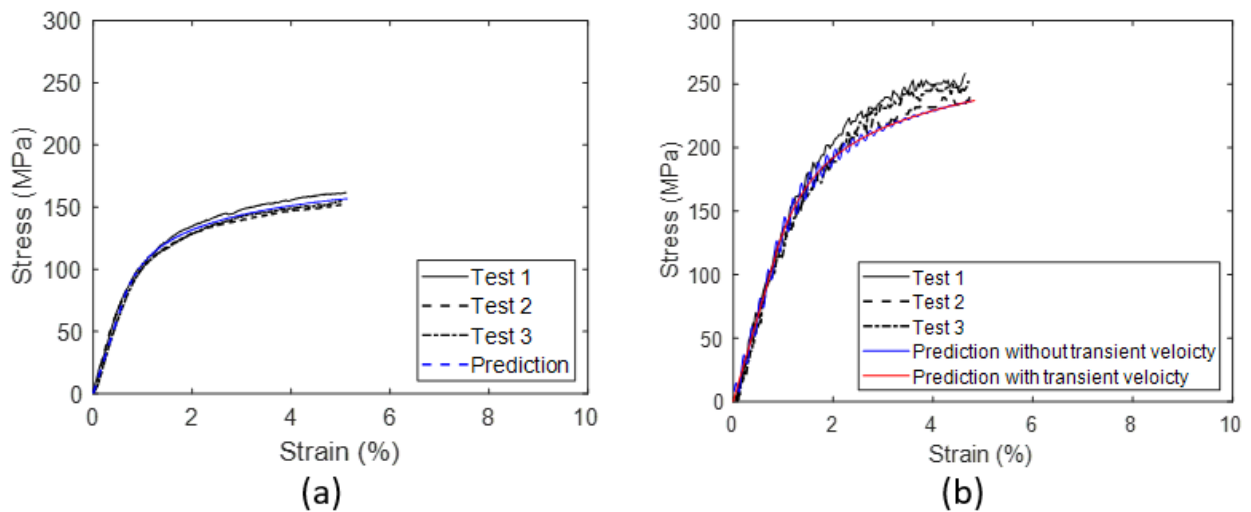


Figure 4-51: Comparison of the predicted and experiment test results for $[\pm 45]_2s$ laminate at the: (a) 0.003 s^{-1} , (b) 315 s^{-1}

4.4.4 Material model verification, and validation for IM7-8552

Since a limited amount of data was available for the UD-NCF composite, data available for a IM7-8552 UDTC was used to further verify and validate the predictive capability of the material model. The material properties for the IM7-8552 UDTC material were taken from [125], and the material model was verified for the in-plane shear, transverse shear and transverse compression modes. A very good agreement between the stress-strain response was observed between the simulated and experimental results for all

three modes (**Figure 4-52**). The material model was also validated for the same material system by subjecting off-axis laminae (15° , 30° , 45° , 60° , 75° and 90°) to an axial compression load at quasi-static and high strain rates. Overall, the predicted and experimental stress-strain response (**Figure 4-53**) compares well for all off-axis tests at both strain rates. Some minor discrepancies were observed between the predicted and experimental results at the higher applied strains.

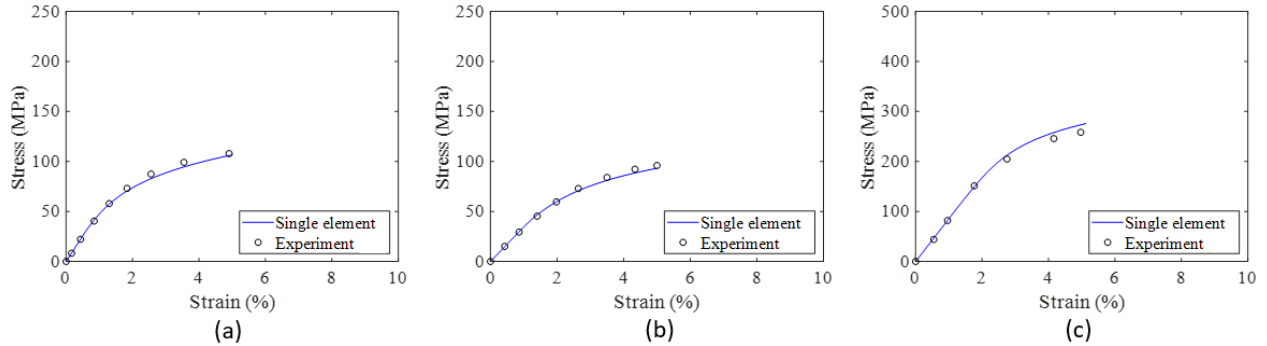


Figure 4-52: Material model verification results for IM7-8552 composite: (a) In-plane shear, (b) Transverse shear, (c) Transverse compression (experimental data was taken from [125]).

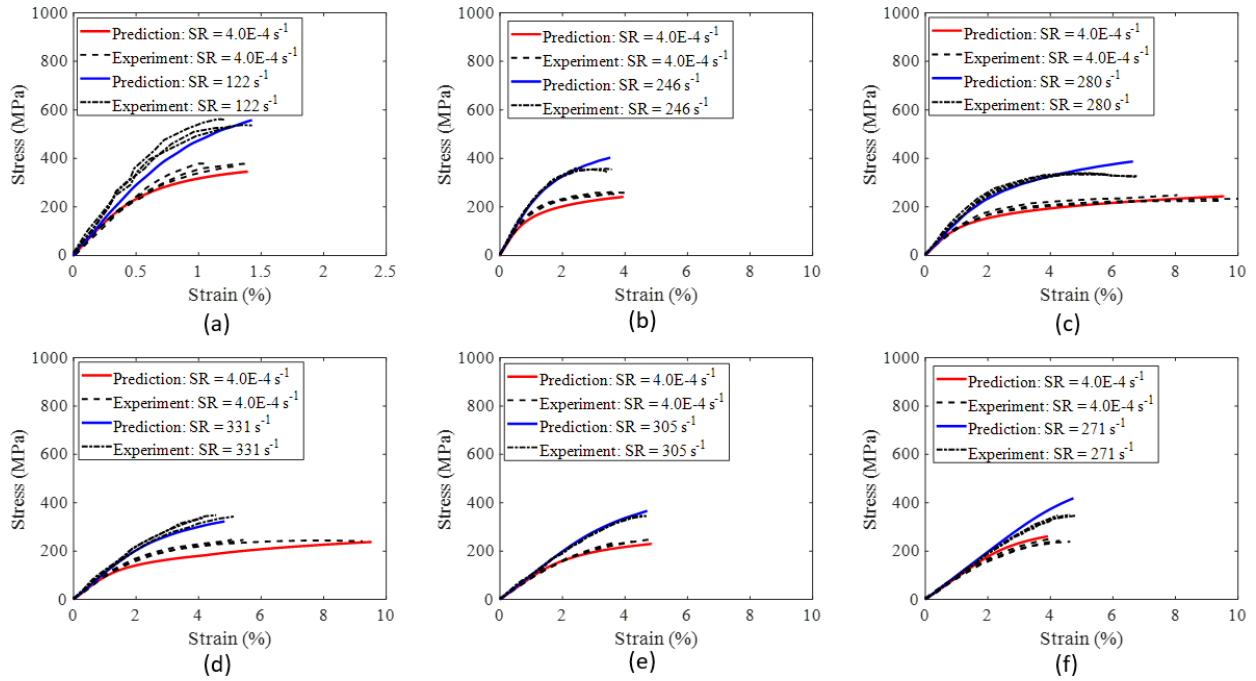


Figure 4-53: Stress-strain plots showing predicted and experimental results [41] at quasi-static and high strain rate for: (a) 15 degree, (b) 30 degree, (c) 45 degree, (d) 60 degree, (e) 75 degree and (f) 90 degree off-axis laminas.

Chapter 5: Conclusions and Recommendations

5.1 Conclusions

The primary objective of this research was to provide support in the development of a high-fidelity CAE impact simulation model tailored to fiber-reinforced composite energy-absorbing structures. The main outcome of this research endeavor was a comprehensive strain rate-dependent material constitutive model that can predict the pre-peak deformation response of a UD-NCF composite. The research comprised three main tasks. The first task involved the development of testing protocols and the characterization of the strain rate-dependent response of the UD-NCF composite material. The second task focused on the development of a multiscale modeling framework to virtually characterize the deformation behavior of the UD-NCF composite. The last task entailed the development, implementation, verification, and validation of the strain rate-dependent constitutive model for predicting the pre-peak deformation response of the UD-NCF composite.

In Task 1, new testing protocols were developed to conduct high-rate testing of the UD-NCF composite material using the tensile and compression SHPB setups. Pulse shaping analysis was used to achieve dynamic equilibrium in the high rate testing, a crucial aspect for FRP materials, often neglected in previous studies. Additionally, a novel and simple testing fixture was designed after several iterations for the longitudinal compression testing of the UD-NCF composite material that prevents premature specimen failure at the ends and ensures consistent failure in the gauge section. A comprehensive dataset was generated through physical laboratory experimentation that encompasses the strain rate-dependent deformation response and failure initiation of the UD-NCF composite material. The experimental work yielded valuable insights into the strain rate-dependent deformation response and failure modes of the in-plane strain rate-dependent material dataset. Moreover, empirical relationships between strain rate and material properties, established through this study, addressed a critical gap in the literature concerning UD-NCF composites. Based on the experimental results, the following conclusions were drawn:

- The transverse tensile strength of the UD-NCF composite increased by approximately 18% with an increase in strain rate from 0.1 s^{-1} to 126 s^{-1} . The transverse tensile modulus was found to be rate independent.

- The pre-peak in-plane shear stress-strain response was found to increase with the increase in strain rate. The in-plane shear strength and yield stress increased by 60% and 61%, respectively, with an increase in strain rate from 0.003 s^{-1} to 315 s^{-1} . The average in-plane shear modulus was found to increase by approximately 10% with increasing strain rate; however, the change in the shear modulus with strain rate was not statistically significant.
- The pre-peak transverse compression stress-strain response was found to increase with the increase in strain rate. The transverse compressive strength and yield stress increased by 50% and 54%, respectively, with an increase in strain rate from 0.003 s^{-1} to 260 s^{-1} . The average transverse compression modulus was found to increase by 20% with an increase in strain rate; however, the change in the transverse compression modulus with the strain rate was not statistically significant.
- An increase of 35% in the longitudinal compression strength was observed with an increase in strain rate from 0.001 s^{-1} to 70 s^{-1} . The longitudinal compression modulus was found to be rate independent.

In Task 2, a dual-scale (microscale and mesoscale) modeling framework was developed to predict the strain rate-dependent deformation response of the UD-NCF composite. The model took into consideration the real material microstructure, including tow crimp and misalignment, that had been commonly overlooked in previous studies. The model captured the strain rate-dependent nonlinear stress-strain response of the UD-NCF composite with good accuracy for different modes. Furthermore, this versatile modeling framework can be applied to other UD-NCF composites as well. The following conclusions were drawn:

- Manufacturing induced defects (tow crimp and fiber misalignment) in the UD-NCF composites had pronounced effect on the longitudinal tensile modulus and strength. Their presence reduced the longitudinal tensile stiffness by approximately 10%. The predicted effect of these manufacturing induced defects on the longitudinal tensile strength was significant and was dependent on the failure criterion used to evaluate the strength.
- The effect of the manufacturing induced defects (tow crimp and fiber misalignment) on the elastic properties and strength for the transverse and in-plane shear modes was negligible, possibly since these modes were primarily governed by the matrix material.

- The stress-strain response for the in-plane and out-of-plane shear modes was found to increase with increasing strain rate. A slight discrepancy was observed between the predicted and experimental results for the in-plane shear mode when the applied strains were higher than 3% for the high rate tests. This discrepancy may be due to ignoring the viscoelastic effects, and the tension-compression asymmetry of the yield surface for the tow. These effects were not modelled since the existing material models in Abaqus CAE cannot capture these effects for the transversely isotropic or orthotropic materials.

In Task 3, an invariant-based constitutive model was developed to predict the nonlinear strain rate-dependent deformation response of unidirectional composite materials. The material model was implemented into LS-DYNA via a user-defined subroutine for use with shell elements. The single element tests were performed for the UD-NCF composite material, characterized in Task 1 and 2, for various modes, including transverse tension, transverse compression, longitudinal tension, longitudinal compression, in-plane shear and out-of-plane shear modes, at different strain rates. Very good agreement between the experimental and single element results was observed indicating that the material model was implemented correctly. The implementation was also verified for another material system, IM7-8552 UDTC, and very good agreement was observed for that material system as well. The first step validation of the material model was performed for an angle ply laminate ($[\pm 45]_{2s}$) of the UD-NCF composite material system under uniaxial compression loading at quasi-static and high strain rates. The predicted results compared very well with the experimental ones indicating that the material model can capture the elastic and inelastic response with good accuracy for different strain rates. The model was also validated for the first step validation for the IM7-8552 UDTC for the 15°, 30°, 45°, 60°, 75° and 90° off-axis laminas at the quasi-static and high strain rate. Again, very good agreement was observed between the predicted and experimental results at both rates (quasi-static and high strain rates) with slight discrepancies observed at the higher applied strains. The discrepancies at the higher applied strain (greater than 5%) might be due to ignoring the fiber rotation that becomes prominent at the high applied strains.

5.2 Recommendations for Future Work

The development of a physically based model to predict high rate failure events, such as axial crush and side impact, in composite structures is an intricate task. This multifaceted problem demands extensive physical and virtual experimentation, along with the development, implementation, and validation of a user-defined material model at both the coupon and component level. As detailed in this thesis, significant progress has been achieved. As next steps, the following recommendations are put forth:

5.2.1 Future experimental work

The in-plane transverse tension, transverse compression, longitudinal tension, longitudinal compression, and shear response of the UD-NCF composite material has been characterized in this study at different strain rates. The Mode I and II interlaminar fracture behaviour and intralaminar fracture toughness for the fiber kinking mode of the UD-NCF composite material was also characterized (not reported in this thesis) [198]. Intralaminar fracture toughness tests for the fiber rupture mode should be performed at different strain rates to complete characterization for the post-peak response of the UD-NCF composite material. The strain rate range for the conducted experiments in this research work was approximately 0.001 s^{-1} to 500 s^{-1} . However, achieving higher rates was not feasible due to constraints imposed by the current test setups. For a more comprehensive understanding of the impact of strain rate on material properties, it is recommended to conduct experiments at higher rates, preferably on the order of 1000 s^{-1} . It is also suggested to use thermal cameras during testing, especially for the in-plane shear tests at high strain rates, to measure the increase in temperature due to the adiabatic heating.

5.2.2 Future multiscale modelling work

A verified dual-scale multiscale modelling framework was developed for predicting the strain rate-dependent deformation response of the UD-NCF composite material. The Tsai-Hill yield function was used for capturing the inelastic response of the tow at the mesoscale; however, this model does not account for the tension-compression asymmetry of the yield surface. Therefore, it is recommended to develop and use a different model that accounts for this effect. The viscoelastic response of the matrix and tow was ignored in this study due to the lack of availability of test data and a suitable material model. It is also suggested to model the viscoelastic response of the matrix and tow as there is experimental evidence that the snap-cure epoxy system used in this study exhibits strain rate dependency of the elastic modulus [23]. It is also suggested to develop a machine learning based data driven model for the virtual experimentation of the UD-NCF composite. The data driven models are computationally very efficient and reduce the modelling efforts by eliminating the need for designing and developing RVEs [199]. The developed framework in this research work can be used as a data generator for generating data needed for developing the data driven model.

5.2.3 Future constitutive model development

A strain rate-dependent invariant-based pre-peak constitutive model has been developed and implemented in LS-DYNA that can predict the strain rate-dependent elastic-inelastic deformation response of UD FRPs. The next steps should include the following:

- Perform validation tests for the off-axis tensile loading conditions at different strain rates.
- Develop and implement strain rate dependent physical based failure initiation models [138]. The existing data can be used for the model calibration and verification. However, additional off-axis tension and compression testing is required to validate the failure initiation models.
- Develop and implement a post-peak damage evolution model for capturing the intralaminar damage [12]. Some initial experimentation has been performed for the fiber kinking mode to characterize the damage evolution (not reported in the thesis). However, further experimentation is required, especially for the fiber rupture mode.
- Develop a traction separation law for the Mode I and Mode II interlaminar delamination. The experimental data is available; however, the traction separation laws need to be derived to model delamination in UD-NCF composite structures.
- After completing the above steps, the material model should be validated at the component level by simulating axial compression, three point bend loading conditions and multiaxial loadings.
- Perform one simulation of a physical dynamic test with complete compression or tensile SHPB apparatuses to determine the robustness of the material model. It is also suggested to keep the data reduction scheme consistent with the experiments.

References

- [1] "The international council on clean transportation (ICCT)," Global PV figure data 20200527, 27 May 2020. [Online]. Available: <https://theicct.org/file/global-pv-figure-data-20200527xlsx-0>. [Accessed 25 November 2020].
- [2] "Fuel economy rollback sets the U.S. further behind the leaders," 08 May 2020. [Online]. Available: <https://www.aceee.org/blog-post/2020/05/fuel-economy-rollback-sets-us-further-behind-leaders>. [Accessed 25 11 2020].
- [3] S. Das, D. Graziano, V. K. Upadhyayula, E. Masanet, M. Riddle and J. Cresko, "Vehicle lightweighting energy use impacts in US light-duty vehicle fleet.," *Sustainable Materials and Technologies.*, vol. 8, pp. 5 - 13, 2016.
- [4] W. J. Joost, "Reducing vehicle weight and improving US energy efficiency using integrated computational materials engineering.," *The Journal of The Minerals, Metals & Materials Society* , vol. 64, no. 9, pp. 1032-1038, 2012.
- [5] P. Gopal Samy Dharmaraj, "Development of a non-crimp fabric carbon fiber/epoxy composite technology demonstrator.," MSc Thesis, University of Waterloo., Waterloo, 2020.
- [6] H. Mason, "Composites end markets: Automotive (2023)," 29 12 2022. [Online]. Available: <https://www.compositesworld.com/articles/composites-end-markets-automotive-2023>. [Accessed 09 07 2023].
- [7] JEC, "Lightweight and sustainable materials for automotive applications.," 20 12 2022. [Online]. Available: <https://www.jeccomposites.com/news/best-of-2022-porsche-gt4-race-car-sustainable-interior/>. [Accessed 09 07 2023].
- [8] A. Cherniaev, C. Butcher and J. Montesano, "Predicting the axial crush response of CFRP tubes using three damage-based constitutive models.," *Thin-Walled Structures*, vol. 129, pp. 349-364, 2018.
- [9] T. Achstetter, "Development of a composite material shell-element model for impact applications.," Doctoral dissertation, George Mason University, Fairfax, 2019.

- [10] T. Bru, "Material characterisation for crash modelling of composites.," Chalmers Tekniska Hogskola, Chalmers, 2018.
- [11] J. Wiegand, "Constitutive modelling of composite materials under impact loading.," PhD Thesis, Oxford University, Oxford, 2009.
- [12] S. T. Pinho, "Modelling failure of laminated composites using physically-based failure models.," PhD Thesis, Imperial College London, London, 2005.
- [13] P. Maimí, P. P. Camanho, J. A. Mayugo and C. G. Dávila, "A continuum damage model for composite laminates: Part II—Computational implementation and validation.," *Mechanics of Materials*, vol. 39, no. 10, pp. 909-919, 2007.
- [14] A. Byar, J. Pang, J. Iqbal, J. Ko and M. Rassaian, "Determination of ballistic limit for IM7/8552 using LSDYNA MAT261.," in *AIAA SciTech Forum.*, Kissimmee, 2018.
- [15] H. Körber, "Mechanical response of advanced composites under high strain rates. PhD Thesis," University of Porto, Porto, 2010.
- [16] J. D. Schaefer, B. T. Werner and I. M. Daniel, "Strain-rate-dependent failure of a toughened matrix composite.," *Experimental Mechanics*, vol. 54, no. 6, pp. 1111-1120, 2014.
- [17] H. Koerber and P. P. Camanho, "High strain rate characterisation of unidirectional carbon–epoxy IM7-8552 in longitudinal compression.," *Composites Part A: Applied Science and Manufacturing*, vol. 42, no. 5, pp. 462-470, 2011.
- [18] A. Gilat and J. D. Seidt, "Compression, tension and shear testing of fibrous composite with the split Hopkinson bar technique.," in *EPJ Web of Conferences*, Arcachon, 2018,.
- [19] L. A. Carlsson, D. F. Adams. and a. R. B. Pipes., *Experimental characterization of advanced composite materials.*, CRC Press, 2014.
- [20] E. A. Trejo Sandoval, "Characterizing the deformation response of a unidirectional non-crimp fabric for the development of computational draping simulation models," MASC Thesis, University of Waterloo, Waterloo, 2020.

- [21] H. H. N. Heß, "Structurally stitched NCF CFRP laminates. Part 1: Experimental characterization of in-plane and out-of-plane properties.," *Composites Science and Technology*, vol. 71, no. 5, pp. 549-568, 2011.
- [22] K. Vallons, G. Adolphs, P. Lucas, S. V. Lomov and I. Verpoest, "The influence of the stitching pattern on the internal geometry, quasi-static and fatigue mechanical properties of glass fibre non-crimp fabric composites.," *Composites Part A: Applied Science and Manufacturing*, vol. 56, pp. 272-279, 2014.
- [23] Y. Zeng, "Mechanical Characterization and Computational Modeling of Snap-cure Epoxy.," MASc Thesis, University of Waterloo, 2020.
- [24] L. Barcenas, S. S. Narayana, L. Khoun and P. & H. P. Trudeau, "Thermochemical and rheological characterization of highly reactive thermoset resins for liquid moulding.," *Journal of Composite Materials*, p. 00219983231181640, 2023.
- [25] T. A. Morley, R. Koeniger, S. Grunder, N. Jelic and R. Hueppi, "Fast curing high glass transition temperature epoxy resin system.". Washington, DC: U.S. Patent and Trademark Office Patent U.S. Patent No. 10,023,686., 17 07 2018.
- [26] J. Frank, "Composite manufacturing processes," [Online]. Available: http://www.materialseducation.org/educators/matedu-modules/docs/Composite_Manufacturing_Processes.pdf. [Accessed 26 12 2020].
- [27] R. W. Kim, C. M. Kim, K. H. Hwang and S. R. Kim, "Embedded based real-time monitoring in the high-pressure resin transfer molding process for CFRP.," *Applied Sciences*, vol. 9, no. 9, p. 1795, 2019.
- [28] M. A. Siddiqui, H. Koelman. and a. P. S. Shembekar., "High pressure RTM process modeling for automotive composite product development.," in *SAE Technical Paper*, Pune, India, 2017.
- [29] A. Cherniaev, Y. Zeng, D. Cronin and J. Montesano, "Quasi-static and dynamic characterization of unidirectional non-crimp carbon fiber fabric composites processed by HP-RTM.," *Polymer Testing*, vol. 76, pp. 365-375, 2019.
- [30] Z. Chen and L. a. X. Z. Peng, "Experimental characterization and numerical simulation of voids in CFRP components processed by HP-RTM.," *Materials*, vol. 15, no. 15, p. 5249, 2022.

- [31] H. & H. N. Heß, "Structurally stitched NCF CFRP laminates. Part 1: Experimental characterization of in-plane and out-of-plane properties.," *Composites Science and Technology*, vol. 71, no. 5, pp. 549-568, 2011.
- [32] A. P. Mouritz and B. N. Cox, "A mechanistic approach to the properties of stitched laminates.," *Composites part A: applied science and manufacturing*, vol. 31, no. 1, pp. 1-27, 2000.
- [33] H. Heß and N. Himmel, "Structurally stitched NCF CFRP laminates. Part 2: Finite element unit cell based prediction of in-plane strength.," *Composites Science and Technology*, vol. 71, no. 5, pp. 569-585, 2011.
- [34] M. Bodaghi, C. Cristóvão, R. Gomes and N. C. Correia, " Experimental characterization of voids in high fibre volume fraction composites processed by high injection pressure RTM.," *Composites Part A: Applied Science and Manufacturing*, vol. 82, pp. 88-89, 2016.
- [35] H. Koerber, J. Xavier and P. P. Camanho, "High strain rate characterisation of unidirectional carbon-epoxy IM7-8552 in transverse compression and in-plane shear using digital image correlation.," *Mechanics of Materials*, vol. 42, no. 11, pp. 1004-1019, 2010.
- [36] Q. Bing and C. T. Sun, "Modeling and testing strain rate-dependent compressive strength of carbon/epoxy composites.," *Composites Science and Technology*, vol. 65, no. 15 - 16, pp. 2481-2491, 2005.
- [37] H. Cui, D. Thomson, A. Pellegrino, J. Wiegand and N. Petrinic, "Effect of strain rate and fibre rotation on the in-plane shear response of $\pm 45^\circ$ laminates in tension and compression tests.," *Composites Science and Technology*, vol. 135, pp. 106-115, 2016.
- [38] A. Gilat, R. K. Goldberg and G. D. Roberts, "Strain rate sensitivity of epoxy resin in tensile and shear loading.," *Journal of Aerospace Engineering*, vol. 20, no. 2, pp. 75-89, 2007.
- [39] M. May, N. Ledford, M. Isakov, P. Hahn, H. Paul and S. Nagasawa, "The effect of strain rate on the orientation of the fracture plane in a unidirectional polymer matrix composite under transverse compression loading.," *Composites Part A: Applied Science and Manufacturing*, vol. 138, p. 106057, 2020.

- [40] L. G. Melin and L. E. Asp, "Effects of strain rate on transverse tension properties of a carbon/epoxy composite: studied by moiré photography.," *Composites Part A: Applied Science and Manufacturing*, vol. 30, no. 3, pp. 305-316, 1999.
- [41] H. Koerber, P. Kuhn, M. Ploeckl, F. Otero, P. W. Gerbaud, R. Rolfes and P. P. Camanho, "Experimental characterization and constitutive modeling of the non-linear stress–strain behavior of unidirectional carbon–epoxy under high strain rate loading," *Advanced Modeling and Simulation in Engineering Sciences*, vol. 5, no. 1, pp. 1-24, 2018.
- [42] G. P. de Araujo, M. V. Donadon, G. Salerno and R. D. C. M. Sales, "Temperature effects on the mechanical behaviour of PAEK thermoplastic composites subjected to high strain rates under compression loading.," *Composite Structures*, vol. 113299, p. 261, 2021.
- [43] X. Zhang, Y. Shi and Z. X. Li, "Experimental study on the tensile behavior of unidirectional and plain weave CFRP laminates under different strain rates.," *Composites Part B: Engineering*, vol. 164, pp. 524-536., 2019.
- [44] R. L. Sierakowski, "Strain rate effects in composites.," *Applied Mechanics Reviews*, vol. 50, no. 12, pp. 741-761, 1997.
- [45] H. M. Hsiao and I. M. Daniel, "Strain rate behavior of composite materials.," *Composites Part B: Engineering*, vol. 29, no. 5, pp. 521-533, 1998.
- [46] S. E. Groves, R. J. Sanchez, R. E. Lyon and A. E. Brown, "High strain rate effects for composite materials.," *ASTM Special Technical Publication*, vol. 1206, pp. 162-176, 1993.
- [47] N. Perogamvros, T. Mitropoulos and G. Lampeas, "Drop tower adaptation for medium strain rate tensile testing.," *Experimental Mechanics*, vol. 56, no. 3, pp. 419-436, 2016.
- [48] N. Taniguchi, T. Nishiwaki and H. Kawada, "Tensile strength of unidirectional CFRP laminate under high strain rate.," *Advanced Composite Materials*, vol. 16, no. 2, pp. 167-180, 2007.
- [49] A. Gilat, R. K. Goldberg and G. D. Roberts, "Experimental study of strain-rate-dependent behavior of carbon/epoxy composite.," *Composites Science and Technology*, vol. 62, no. 10-11, pp. 1469-1476, 2002.

- [50] T. Werling, G. Baumann, F. Feist, W. Sinz and C. Ellersdorfer, "On the dynamic electro-mechanical failure behavior of automotive high-voltage busbars using a split Hopkinson pressure bar.," *Materials*, vol. 21, no. 6320, p. 14, 2021.
- [51] K. Rouf, M. Worswick and J. Montesano, "Strain Rate Dependent Response of Non-Crimp Fabric Composites.," in *In Proceedings of the American Society for Composites - Thirty-fourth Technical Conference*, Atlanta, 2019.
- [52] T. Fíla, "Split Hopkinson pressure bar: Design parameters and prediction of the experiment output," in *24th International Conference Engineering Mechanics*, Svatka, Czech Republic, 2018.
- [53] S. Nemat-Nasser, J. B. Isaacs and J. E. Starrett, "Hopkinson techniques for dynamic recovery experiments.," in *Proceedings of the Royal Society of London. Series A: Mathematical and Physical Sciences*, 1991.
- [54] L. Ninan, J. Tsai and C. T. Sun, "Use of split Hopkinson pressure bar for testing off-axis composites.," *International Journal of Impact Engineering*, vol. 25, no. 3, pp. 291-313, 2001.
- [55] W. Chen, F. Lu and M. Cheng, "Tension and compression tests of two polymers under quasi-static and dynamic loading.," *Polymer Testing*, vol. 21, no. 2, pp. 113-121, 2002.
- [56] R. Gerlach, S. K. Sathianathan, C. Siviour and N. Petrinic, "A novel method for pulse shaping of Split Hopkinson tensile bar signals.," *International Journal of Impact Engineering*, vol. 38, no. 12, pp. 976-980, 2011.
- [57] Y. Zhou, Y. Wang, S. Jeelani and Y. Xia, "Experimental study on tensile behavior of carbon fiber and carbon fiber reinforced aluminum at different strain rate.," *Applied Composite Materials*, vol. 14, no. 1, pp. 17-31, 2007.
- [58] Y. Ou, D. Zhu, H. Zhang, Y. Yao, B. Mobasher and L. Huang, "Mechanical properties and failure characteristics of CFRP under intermediate strain rates and varying temperatures.," *Composites Part B: Engineering*, vol. 95, pp. 123-136, 2016.
- [59] C. R. Siviour and J. L. Jordan, "High strain rate mechanics of polymers: a review.," *Journal of Dynamic Behavior of Materials*, vol. 2, no. 1, pp. 15 - 32, 2016.

- [60] R. Gerlach, C. R. Siviour, N. Petrinic and J. Wiegand, "Experimental characterisation and constitutive modelling of RTM-6 resin under impact loading.," *Polymer*, vol. 49, no. 11, pp. 2728-2737, 2008.
- [61] J. Harding and L. M. Welsh, "A tensile testing technique for fibre-reinforced composites at impact rates of strain.," *Journal of Materials Science*, vol. 18, no. 6, pp. 1810-1826, 1983.
- [62] J. L. Tsai and C. T. Sun, "Strain rate effect on in-plane shear strength of unidirectional polymeric composites.," *Composites Science and Technology*, vol. 65, no. 13, pp. 1941-1947, 2005.
- [63] ASTM D 3518/D 3518M - 94, *Standard test method for in-plane shear response of polymer matrix composite materials by tensile test of a 45 laminate.*, 2001.
- [64] ASTM D 5379/D 5379M - 05, *Shear properties of composite materials by the v-notched beam method.*, 2005.
- [65] ASTM D7078-05, *Shear properties of composite materials by v-notched rail shear method.*, 2005.
- [66] T. Yokoyama and K. Nakai, "Impact compressive failure of a unidirectional carbon/epoxy laminated composite in three principal material directions.," in *Proceedings of DYMAT 2009 Conference*, Brussels, Belgium, 2009.
- [67] M. V. Hosur, J. Alexander, U. K. Vaidya and S. Jeelani, "High strain rate compression response of carbon/epoxy laminate composites.," *Composite Structures*, vol. 52, no. 3-4, pp. 405 - 417, 2001.
- [68] M. Ploeckl, P. Kuhn and H. Koerber, "Characterization of unidirectional carbon fiber reinforced polyamide-6 thermoplastic composite under longitudinal compression loading at high strain rate.," in *EPJ Web of Conferences*, Lugano, Switzerland, 2015.
- [69] M. Ploeckl, P. Kuhn, J. Grosser, M. Wolfahrt and H. Koerber, "A dynamic test methodology for analyzing the strain-rate effect on the longitudinal compressive behavior of fiber-reinforced composites.," *Composite Structures*, vol. 180, pp. 429-438, 2017.
- [70] J. Lienhard and W. Böhme, "Characterisation of resin transfer moulded composite laminates under high rate tension, compression and shear loading.," *Engineering Fracture Mechanics*, vol. 149, pp. 338-350, 2015.

- [71] K. Rouf, X. Liu and W. Yu, "Multiscale structural analysis of textile composites using mechanics of structure genome.," *International Journal of Solids and Structures*, vol. 136, pp. 89-102, 2018.
- [72] J. Montesano and F. Sharifpour, "Multi-Scale Continuum Mechanics Modelling of Fibre-Reinforced Polymer Composites.," in *W. Van Paepegem (Ed.), Modelling damage evolution in multidirectional laminates: micro to macro.*, Woodhead Publishing Series in Composites Science and Engineering, 2021, pp. 463-507.
- [73] C. S. Lopes, C. González, O. Falcó, F. Naya, J. Llorca and B. Tijs, "Multiscale virtual testing: the roadmap to efficient design of composites for damage resistance and tolerance.," *CEAS Aeronautical Journal*, vol. 7, pp. 607-619, 2016.
- [74] X. Liu, K. Rouf, B. Peng and W. Yu, "Two-step homogenization of textile composites using mechanics of structure genome.," *Composite Structures*, vol. 171, pp. 252-262, 2017.
- [75] J. Montesano and F. Sharifpour, "Modelling damage evolution in multidirectional laminates: micro to macro.," in *Multi-Scale Continuum Mechanics Modelling of Fibre-Reinforced Polymer Composites.*, Woodhead Publishing, 2021, pp. 463-507.
- [76] W. Yu, "An introduction to micromechanics.," *Applied Mechanics and Materials*, vol. 828, pp. 3-24, 2016.
- [77] S. B. R. Devireddy and S. Biswas, "Effect of fiber geometry and representative volume element on elastic and thermal properties of unidirectional fiber-reinforced composites.," *Journal of Composites*, pp. 1-12, 2014.
- [78] K. Rouf, X. Liu and W. Yu, "Multiscale structural analysis of textile composites using mechanics of structure genome.," *International Journal of Solids and Structures*, vol. 136, pp. 89-102, 2018.
- [79] G. Li, F. Sharifpour, A. Bahmani and J. Montesano, "A new approach to rapidly generate random periodic representative volume elements for microstructural assessment of high volume fraction composites.," *Materials & Design*, vol. 150, pp. 124-138, 2018.
- [80] A. Melro, "Analytical and numerical modelling of damage and fracture of advanced composites.," PhD thesis, Universidade do Porto, Portugal, 2011.

- [81] W. Voigt, "Ueber die Beziehung zwischen den beiden Elasticitätsconstanten isotroper Körper.," *Annalen der physik*, vol. 274, no. 12, pp. 573-587, 1889.
- [82] A. Reuss, "Calculation of the yield point of mixed crystals from plasticity conditions for single crystals," *Z Angew Math Mechanik*, vol. 9, pp. 49-58, 1929.
- [83] Z. Hashin and S. Shtrikman, "A variational approach to the theory of the elastic behaviour of multiphase materials.," *Journal of the Mechanics and Physics of Solids*, vol. 11, no. 2, pp. 127-140, 1963.
- [84] T. Mori and K. Tanaka, "Average stress in matrix and average elastic energy of materials with misfitting inclusions.," *Acta metallurgica*, vol. 21, no. 5, pp. 571-574, 1973.
- [85] Y. Benveniste, "A new approach to the application of Mori-Tanaka's theory in composite materials.," *Mechanics of materials*, vol. 6, no. 2, pp. 147-157, 1987.
- [86] B. Raju, S. R. Hiremath and D. R. Mahapatra, "A review of micromechanics based models for effective elastic properties of reinforced polymer matrix composites.," *Composite Structures*, vol. 204, pp. 607-619, 2018.
- [87] T. D. G. J. & B. Y. Chen, "Mori-Tanaka estimates of the overall elastic moduli of certain composite materials.," *ASME Journal of Applied Mechanics*, vol. 59, no. 3, pp. 539-546, 1992.
- [88] Y. H. Zhao, G. P. Tandon and G. J. Weng, "Elastic moduli for a class of porous materials.," *Acta Mechanica*, vol. 76, pp. 105-131, 1989.
- [89] G. P. Tandon and G. J. Weng, "The effect of aspect ratio of inclusions on the elastic properties of unidirectionally aligned composites.," *Polymer Composites*, vol. 5, no. 4, pp. 327-333, 1984.
- [90] H. Liu and L. C. Brinson, "A hybrid numerical-analytical method for modeling the viscoelastic properties of polymer nanocomposites.," *Journal of Applied Mechanics*, pp. 758-768, 2006.
- [91] Y. W. A. M. Li and E. M. Arruda, "A closed-form, hierarchical, multi-interphase model for composites—Derivation, verification and application to nanocomposites.," *Journal of the Mechanics and Physics of Solids*, vol. 59, no. 1, pp. 43-63, 2011.

- [92] H. A. Luo and G. J. Weng, "On Eshelby's inclusion problem in a three-phase spherically concentric solid, and a modification of Mori-Tanaka's method.," *Mechanics of Materials*, vol. 6, no. 4, pp. 347-361, 1987.
- [93] M. Barral, G. Chatzigeorgiou, F. Meraghni and R. Léon, "Homogenization using modified Mori-Tanaka and TFA framework for elastoplastic-viscoelastic-viscoplastic composites: Theory and numerical validation.," *International Journal of Plasticity*, vol. 102632, p. 127, 2020.
- [94] S. Koyama, S. Katano, I. Saiki and T. Iwakuma, "A modification of the Mori–Tanaka estimate of average elastoplastic behavior of composites and polycrystals with interfacial debonding.," *Mechanics of Materials*, vol. 43, no. 10, pp. 538-555, 2011.
- [95] J. Aboudi, "Generalized effective stiffness theory for the modeling of fiber-reinforced composites," *International Journal of Solids and Structures*, vol. 17, no. 10, pp. 1005-1018, 1981.
- [96] J. Aboudi, "Micromechanical analysis of the strength of unidirectional fiber composites.," *Composites Science and Technology*, vol. 33, no. 2, pp. 79-96, 1988.
- [97] J. Aboudi, "Micromechanical characterization of the non-linear viscoelastic behavior of resin matrix composites.," *Composites Science and Technology*, vol. 38, no. 4, pp. 371-386, 1990.
- [98] Z. Sun, X. Zhao, X. Wang and J. Ma, "Predicting the elastic properties of sisal fiber reinforced polypropylene composites by a new method based on generalized method of cells and laminate analogy approach.," *Composites Science and Technology*, vol. 91, no. 4, pp. 45-49, 2014.
- [99] J. Aboudi, "Damage in composites—modeling of imperfect bonding.," *Composites Science and Technology*, vol. 28, no. 2, pp. 103-128, 1987.
- [100] B. Y. Low, S. D. Gardner, C. U. Pittman Jr and R. M. Hackett, "A micromechanical characterization of graphite-fiber/epoxy composites containing a heterogeneous interphase region.," *Composites Science and Technology*, vol. 52, no. 4, pp. 589-606, 1994.
- [101] R. Hill, "A self-consistent mechanics of composite materials.," *Journal of the Mechanics and Physics of Solids*, vol. 13, no. 4, pp. 213-222, 1965.

- [102] T. Sabiston, M. Mohammadi, M. Cherkaoui, J. Lévesque and K. Inal, "Micromechanics for a long fibre reinforced composite model with a functionally graded interphase.," *Composites Part B: Engineering*, Vols. 188-199, p. 84, 2016.
- [103] J. Aboudi, S. Arnold and B. Bednarczyk, *Micromechanics of composite materials: a generalized multiscale analysis approach.*, Oxford: Butterworth-Heinemann, 2013.
- [104] T. Sabiston, M. Mohammadi, M. Cherkaoui, J. Levesque and K. Inal, "Micromechanics based elasto-visco-plastic response of long fibre composites using functionally graded interphases at quasi-static and moderate strain rates.," *Composites Part B: Engineering*, vol. 100, pp. 31- 43, 2016.
- [105] E. Ghossein and M. Lévesque, "Homogenization models for predicting local field statistics in ellipsoidal particles reinforced composites: Comparisons and validations.," *International Journal of Solids and Structures*, 58, 91-105., vol. 58, pp. 91-105, 2015.
- [106] P. P. Castañeda, "The effective mechanical properties of nonlinear isotropic composites.," *Journal of the Mechanics and Physics of Solids*, vol. 39, no. 1, pp. 45-71, 1991.
- [107] M. M. Zhou and G. Meschke, "Strength homogenization of matrix-inclusion composites using the linear comparison composite approach.," *International Journal of Solids and Structures*, vol. 51, no. 1, pp. 259-273, 2014.
- [108] J. J. Espadas-Escalante, N. P. van Dijk and P. Isaksson, "A study on the influence of boundary conditions in computational homogenization of periodic structures with application to woven composites.," *Composite Structures*, vol. 160, pp. 529-537, 2017.
- [109] W. Yu, "A unified theory for constitutive modeling of composites.," *Journal of Mechanics of Materials and Structures*, vol. 11, no. 4, pp. 379-411, 2016.
- [110] F. Edgren and L. Asp, "Approximate analytical constitutive model for non-crimp fabric composites.," *Composites Part A: Applied Science and Manufacturing*, vol. 36, no. 2, pp. 173-181, 2005.
- [111] R. Olsson, E. Marklund and N. Jansson, "Testing of carbon/epoxy NCF strength under mixed in-plane loading.," in *Proceedings of ECCM-15 Conference.*, Vanice, Italy, 2012.
- [112] J. C. Halpin, *Primer on Composite Materials Analysis, (Revised).*, CRC Press., 1992.

- [113] S. Drapier and M. R. Wisnom, "Finite-element investigation of the compressive strength of non-crimp-fabric-based composites.," *Composites Science and Technology*, vol. 59, no. 8, pp. 1287-1297, 1999.
- [114] E. Marklund, L. E. Asp and R. Olsson, "Transverse strength of unidirectional non-crimp fabric composites: Multiscale modelling.," *Composites Part B: Engineering*, vol. 65, pp. 47-56, 2014.
- [115] Y. Cao, Y. Feng, W. Wang, D. Wu and Z. Zhu, "Estimation of lamina stiffness and strength of quadriaxial non-crimp fabric composites based on semi-laminar considerations.," *Applied Sciences*, vol. 6, no. 9, p. 267, 2016.
- [116] A. González, E. Graciani and F. París, "Prediction of in-plane stiffness properties of non-crimp fabric laminates by means of 3D finite element analysis.," *Composite Science and Technology*, vol. 68, no. 1, pp. 121-131, 2008.
- [117] G. Ernst, M. Vogler, C. Hühne and R. Rolfes, "Multiscale progressive failure analysis of textile composites.," *Composites Science and Technology*, vol. 70, no. 1, pp. 61-72, 2010.
- [118] M. Lidgett, "Multi-scale modelling of polymer composite materials at high rates of strain.," PhD Thesis, University of Nottingham, Nottingham, UK, 2012.
- [119] V. Singh, R. Larsson, R. Olsson and E. Marklund, "A micromechanics based model for rate dependent compression loaded unidirectional composites.," *Composites Science and Technology*, vol. 232, p. 109821, 2023.
- [120] D. Shi and X. Xiao, "An enhanced continuum damage mechanics model for crash simulation of composites.," *Composite Structures*, vol. 185, pp. 774-785, 2018.
- [121] B. Khaled, "Experimental characterization and finite element modeling of composites to support a generalized orthotropic elasto-plastic damage material model for impact analysis.," Doctoral dissertation, ProQuest Dissertations Publishing, Tucson, Arizona, 2019.
- [122] "Macromechanics of lamina," [Online]. Available: https://www.efunda.com/formulae/solid_mechanics/composites/comp_lamina_principal.cfm. [Accessed 10 05 2021].

- [123] L. W. Meyer and M. Mayer, "New strain rate dependent material model for fiber reinforced composites.," in *In Time Dependent Constitutive Behavior and Fracture/Failure Processes, Volume 3: Proceedings of the 2010 Annual Conference on Experimental* , New York, 2011.
- [124] C. Hoffarth, "A generalized orthotropic elasto-plastic material model for impact analysis.," PhD Thesis, ProQuest Dissertations Publishing, Tucson, Arizona, 2016.
- [125] M. Vogler, R. Rolfes and P. P. Camanho., "Modeling the inelastic deformation and fracture of polymer composites–Part I: plasticity model.," *Mechanics of Materials*, vol. 59, pp. 50-64, 2013.
- [126] C. T. Sun and K. J. Yoon., "Elastic-plastic analysis of AS4/PEEK composite laminate using a one-parameter plasticity model.," *Journal of Composite Materials*, vol. 26, no. 2, pp. 293-308, 1992.
- [127] P. Kelley, "Solid Mechanics Part II: Engineering Solid Mechanics – Small Strain," [Online]. Available: http://homepages.engineering.auckland.ac.nz/~pkel015/SolidMechanicsBooks/Part_II/index.html. [Accessed 27 12 2020].
- [128] J. Lubliner, *Plasticity theory.*, Courier Corporation., 2008.
- [129] R. K. Goldberg, K. S. Carney, P. DuBois, C. Hoffarth, B. Khaled, S. Rajan and G. Blankenhorn, "Incorporation of damage and failure into an orthotropic elasto-plastic three-dimensional model with tabulated input suitable for use in composite impact problems.," in *LS DYNA International Conference*, 2016.
- [130] S. W. Tsai and E. M. Wu, "A general theory of strength for anisotropic materials.," *Journal of composite materials*, vol. 5, no. 1, pp. 58-80, 1971.
- [131] W. Tan and B. Liu, "A physically-based constitutive model for the shear-dominated response and strain rate effect of Carbon Fibre Reinforced composites.," *Composites Part B: Engineering*, vol. 193, p. 108032, 2020.
- [132] S. V. Thiruppukuzhi and C. T. Sun, "Models for the strain-rate-dependent behavior of polymer composites.," *Composites Science and Technology*, vol. 61, no. 1, pp. 1-12, 2001.
- [133] P. Perzyna, "Fundamental problems in viscoplasticity. Advances in applied mechanics.," *Advances in applied mechanics.*, vol. 9, pp. 243-377, 1966.

- [134] S. A. Capasciutti de Oliveira and M. Vicente Donadon, "A 3D progressive failure model for crushing simulations in composite structures.," *International journal of crashworthiness*, vol. 27, no. 2, pp. 591-613, 2022.
- [135] S. Li, "The maximum stress failure criterion and the maximum strain failure criterion: their unification and rationalization.," *Journal of Composites Science*, vol. 4, no. 4, p. 157, 2020.
- [136] A. Puck and H. Schürmann, "Failure analysis of FRP laminates by means of physically based phenomenological models.," *Composites science and technology*, vol. 62, no. 12-13, pp. 1633-1662, 2002.
- [137] S. T. Pinho, G. M. Vyas and P. Robinson, "Material and structural response of polymer-matrix fibre-reinforced composites: Part B.," *Journal of Composite Materials*, vol. 47, no. 6-7, pp. 679-696, 2013.
- [138] P. P. Camanho, A. Arteiro, A. R. Melro, G. Catalanotti and M. Vogler, "Three-dimensional invariant-based failure criteria for fibre-reinforced composites.," *International Journal of Solids and Structures*, vol. 55, pp. 92-107, 2015.
- [139] R. M. Christensen, "The world wide failure exercise II examination of results.," *Journal of Reinforced Plastics and Composites*, vol. 32, no. 21, pp. 1668-1672, 2013.
- [140] M. J. Hinton, A. S. Kaddour and P. D. Soden, *Failure criteria in fibre reinforced polymer composites: The world-wide failure exercise.*, Elsevier Ltd., 2004.
- [141] J. D. Schaefer, B. T. Werner and I. M. Daniel, "Strain-rate-dependent failure of a toughened matrix composite.," *Experimental Mechanics*, vol. 54, pp. 1111-1120, 2014.
- [142] C. Pohl, M. Toenjes, C. Liebold, M. Ploeckl, H. Koerber, L. A. Gray and K. Drechsler, "Numerical prediction of composite damage behavior: A modeling approach including the strain-rate-dependent material response.," *Composite Structures*, vol. 115628, p. 292, 2022.
- [143] R. Talreja and C. V. Singh, *Damage and failure of composite materials.*, Cambridge University Press, 2012.
- [144] L. M. Kachanov, "On creep rupture time.," *Izv. Acad. Nauk SSSR, Otd. Techn. Nauk.*, vol. 8, pp. 26-31, 1958.

- [145] Y. N. Rabotnov, Creep problems in structural member., North-Holland, 1969.
- [146] J. Lemaitre, "A continuous damage mechanics model for ductile fracture.," *J Eng Mater Technol, Trans ASME*, vol. 83, no. 9, pp. 107-42, 107:42 (1985).
- [147] S. Murakami and N. Ohno, "A continuum theory of creep and creep damage.," Springer-Verlag, Berlin, 1981.
- [148] J. Lemaitre and J. L. Chaboche, *Mechanics of solid materials.*, Cambridge: Cambridge university press, 1994.
- [149] F. K. Chang and K. Y. Chang, "A progressive damage model for laminated composites containing stress concentrations.," *Journal of composite materials*, vol. 21, no. 9, pp. 834-855, 1987.
- [150] A. Matzenmiller, J. Lubliner and R. L. Taylor, "A constitutive model for anisotropic damage in fiber-composites.," *Mechanics of Materials.*, vol. 20, no. 2, pp. 125-152, 1995.
- [151] P. Ladeveze, "A damage computational approach for composites: Basic aspects and micromechanical relations," *Computational Mechanics*, vol. 17, no. 1-2, pp. 142-150, 1995.
- [152] S. T. Pinho, L. Iannucci and P. Robinson, "Physically-based failure models and criteria for laminated fibre-reinforced composites with emphasis on fibre kinking: Part I: Development.," *Composites Part A: Applied Science and Manufacturing*, vol. 37, no. 1, pp. 63-73, 2006.
- [153] W. Tan, B. G. Falzon, L. N. Chiu and M. Price, "Predicting low velocity impact damage and Compression-After-Impact (CAI) behaviour of composite laminates.," *Composites Part A: Applied Science and Manufacturing*, vol. 71, pp. 212 - 226, 2015.
- [154] H. Koerber, P. Kuhn, M. Ploeckl, F. Otero, P. W. Gerbaud, R. Rolfes and P. P. Camanho, "Experimental characterization and constitutive modeling of the non-linear stress–strain behavior of unidirectional carbon–epoxy under high strain rate loading.," *Advanced Modeling and Simulation in Engineering Sciences*, vol. 5, no. 1, pp. 1-24, 2018.
- [155] L. F. M. Leite, B. M. Leite, V. L. Reis, N. N. A. da Silveira and M. V. Donadon, "Strain rate effects on the intralaminar fracture toughness of composite laminates subjected to tensile load.," *Composite Structure*, vol. 201, pp. 455-467, 2018.

- [156] J. Hoffmann, H. Cui and N. Petrinic, "Determination of the strain-energy release rate of a composite laminate under high-rate tensile deformation in fibre direction.," *Composites Science and Technology*, vol. 164, pp. 110-119, 2018.
- [157] S. Boria, *Lightweight design and crash analysis of composites.*, Woodhead Publishing., 2016.
- [158] C. Liebold, A. Haufe, T. Klöppel and S. Hartmann, "Recent developments and trends for composite modeling in LS-DYNA.," *Fachkongress Composite Simulation*, 2015.
- [159] M. Osborne, "Single-element characterization of the LS-DYNA MAT54 material model.," PhD Thesis, 2013.
- [160] J. Reiner and R. Vaziri, "Progressive axial crushing of composite laminates: A comparison between LS-DYNA continuum damage models.," in *Proceedings of the American Society for Composites—Thirty-third Technical Conference.*, 2018.
- [161] Z. Hashin, "Failure criteria for unidirectional fiber composites.," *Journal of Applied Mechanics*, vol. 47, no. 2, pp. 329-334, 1980.
- [162] N. N. Hussain, S. P. Regalla and Y. V. D. Rao, "Techniques for correlation of drop weight impact testing and numerical simulation for composite GFRP crash boxes using Ls-Dyna.," *International Journal of Crashworthiness*, pp. 1-17, 2020.
- [163] E. L. Fasanella, M. S. Annett, K. E. Jackson and M. A. Polanco, "Simulating the response of a composite honeycomb energy absorber. II: Full-scale impact testing.," *Journal of Aerospace Engineering*, vol. 27, no. 3, pp. 437-441, 2014.
- [164] K. V. Williams, R. Vaziri and A. Poursartip, "A physically based continuum damage mechanics model for thin laminated composite structures.," *International Journal of Solids and Structures*, vol. 40, no. 9, pp. 2267-2300, 2003.
- [165] N. Zobeiry, A. Forghani, C. McGregor, S. McClennan, R. Vaziri and A. Poursartip, "Effective calibration and validation of a nonlocal continuum damage model for laminated composites.," *Composite Structures.*, vol. 173, pp. 188-195, 2013.

- [166] S. Rajan, C. Hoffarth, B. Khaled and L. Shyamsunder, "A User Guide for *MAT_COMPOSITE_TABULATED_PLASTICITY_DAMAGE in LS-DYNA®.," Arizona State University, 2020.
- [167] S. T. Pinho, L. Iannucci and P. Robinson, "Physically-based failure models and criteria for laminated fibre-reinforced composites with emphasis on fibre kinking: Part I: Development.," *Composites Part A: Applied Science and Manufacturing*, vol. 37, no. 1, pp. 63-73, 2006.
- [168] T. L. Anderson, *Fracture mechanics: fundamentals and applications.*, CRC Press, 2017.
- [169] P. Maimí, P. P. Camanho, J. A. Mayugo and C. G. Dávila, "A continuum damage model for composite laminates: Part I—Constitutive model.," *Mechanics of Materials*, vol. 39, no. 10, pp. 897-908, 2007.
- [170] R. Talreja, "Assessment of the fundamentals of failure theories for composite materials.," *Composites Science and Technology*, vol. 105, pp. 190-201, 2014.
- [171] A. P. Suratkar, "Damage in non-crimp fabric carbon fiber reinforced epoxy composites under various mechanical loading conditions.," PhD dissertation, University of Western Ontario, 2022.
- [172] K. Rouf, A. Suratkar, J. Imbert-Boyd, J. Wood, M. Worswick and J. Montesano, "Effect of Strain Rate on the Transverse Tension and Compression Behavior of a Unidirectional Non-Crimp Fabric Carbon Fiber/Snap-Cure Epoxy Composite.," *Materials*, vol. 14, no. 23, p. 7314, 2021.
- [173] A. D6856-03, *Standard Guide for Testing Fabric-Reinforced "Textile" Composite Materials*, 2008.
- [174] K. Rouf, M. J. Worswick and J. Montesano, "Strain Rate-Dependent Characterization of the In-Plane Shear Response of a Unidirectional Non-Crimp Fabric Carbon Fiber/Snap-Cure Epoxy Composite.," in *In Proceedings of the American Society for Composites - Thirty-Sixth Technical Conference on Composite Materials*, College Station, 2021.
- [175] A. D695, "Standard Test Method for Compressive Properties of Rigid Plastics," 2015.
- [176] G. Li, F. Sharifpour, A. Bahmani and J. Montesano, "A new approach to rapidly generate random periodic representative volume elements for microstructural assessment of high volume fraction composites.," *Materials & Design*, vol. 150, pp. 124-138, 2018.

- [177] K. Rouf, M. J. Worswick and J. Montesano, "A multiscale framework for predicting the mechanical properties of unidirectional non-crimp fabric composites with manufacturing induced defects.," *Journal of Composite Materials*, vol. 55, no. 6, pp. 741-757, 2020.
- [178] ZOLTEK, "www.zoltek.com," [Online]. Available: <https://zoltek.com/products/px35/>. [Accessed 30 June 2020].
- [179] C. T. Sun and R. S. Vaidya, "Prediction of composite properties from a representative volume element.," *Composites Science and Technology*, vol. 56, no. 2, pp. 171-179, 1996.
- [180] R. N. Haward and G. I. Thackray, "The use of a mathematical model to describe isothermal stress-strain curves in glassy thermoplastics.," *Proceedings of the Royal Society of London. Series A. Mathematical and Physical Sciences*, vol. 302, no. 1471, pp. 453-472, 1968.
- [181] M. C. Boyce, D. M. Parks and A. S. Argon, "Large inelastic deformation of glassy polymers. Part I: rate dependent constitutive model.," *Mechanics of materials*, vol. 7, no. 1, pp. 15-33, 1988.
- [182] C. P. Buckley and D. C. Jones, "Glass-rubber constitutive model for amorphous polymers near the glass transition.," *Polymer*, vol. 36, no. 17, pp. 3301-3312, 1995.
- [183] D. C. Drucker and W. Prager, "Soil mechanics and plastic analysis or limit design.," *Quarterly of Applied Mathematics*, vol. 10, no. 2, pp. 157-165, 1952.
- [184] G. R. Johnson and W. H. Cook, "A constitutive model and data for materials subjected to large strains, high strain rates, and high temperatures.," *In Proceedings of the 7th International Symposium on Ballistics*, vol. 21, no. 1, pp. 541-547, 1983.
- [185] R. Hill, "A theory of the yielding and plastic flow of anisotropic metals.," *Proceedings of the Royal Society of London. Series A. Mathematical and Physical Sciences*, vol. 193, no. 1033, pp. 281-297, 1948.
- [186] C. Sorini, A. Chattopadhyay and R. K. Goldberg, "Micromechanical modeling of the effects of adiabatic heating on the high strain rate deformation of polymer matrix composites.," *Composite Structures*, vol. 215, pp. 377-384, 2019.

- [187] Z. Pan, Z. Wu and J. Xiong, "Localized temperature rise as a novel indication in damage and failure behavior of biaxial non-crimp fabric reinforced polymer composite subjected to impulsive compression.," *Aerospace Science and Technology*, vol. 103, p. 105885, 2020.
- [188] N. Pournoori, G. C. Soares, O. Orell, S. Palola, M. Hokka and M. Kanerva, "Adiabatic heating and damage onset in a pultruded glass fiber reinforced composite under compressive loading at different strain rates.," *International Journal of Impact E*, vol. 147, p. 103728, 2021.
- [189] G. Ernst, "Multiscale analysis of textile composites: stiffness and strength.," Ph.D. thesis, Mitteilungen des Instituts für Statik und Dynamik der Leibniz-Universität, Hannover, 2009.
- [190] Q. S. Zheng and A. J. M. Spencer, "Tensors which characterize anisotropies," *International Journal of Engineering Science*, vol. 31, no. 5, pp. 679-693, 1993.
- [191] A. Dean, J. Reinoso, S. Sahraee and R. Rolfes, "An invariant-based anisotropic material model for short fiber-reinforced thermoplastics: coupled thermo-plastic formulation.," *Composites Part A: Applied Science and Manufacturing*, vol. 90, pp. 186-199, 2016.
- [192] B. Eidel, "Anisotropic inelasticity-modelling, simulation, validation.," Shaker, 2005.
- [193] J. Boehler, *Applications of Tensor Functions in Solid Mechanics.*, Vienna: Springer, 1987.
- [194] K. Rouf, M. J. Worswick and J. Montesano, "Effect of Strain Rate on the In-plane Mechanical Response of a Unidirectional Non-Crimp Fabric Carbon Fiber/Snap-Cure Epoxy Composite.," *In review*, 2023.
- [195] B. Eidel, "Anisotropic inelasticity-modelling, simulation, validation.," Shaker, 2005.
- [196] K. Rouf, M. J. Worswick and J. Montesano, "Experimentally verified dual-scale modelling framework for predicting the strain rate-dependent nonlinear anisotropic deformation response of unidirectional non-crimp fabric composites.," *Composite Structures*, vol. 303, p. 116384, 2023.
- [197] A. Dean, N. Safdar and R. Rolfes, "A Co-Rotational Based Anisotropic Elasto-Plastic Model for Geometrically Non-Linear Analysis of Fibre Reinforced Polymer Composites: Formulation and Finite Element Implementation.," *Materials*, vol. 12, no. 11, p. 1816, 2019.

- [198] K. Rouf, M. J. Worswick and J. Montesano, "Effect of Loading Rate on Mode II Interlaminar Fracture Toughness.," in *10th International Conference on Composites Testing and Model Identification*, Lille, 2021.
- [199] X. Liu, F. Gasco, J. Goodsell and W. Yu, " Initial failure strength prediction of woven composites using a new yarn failure criterion constructed by deep learning.," *Composite Structures*, vol. 111505, p. 230, 2019.
- [200] H.-A. Rami and a. J. Aboudi, "Formulation of the high-fidelity generalized method of cells with arbitrary cell geometry for refined micromechanics and damage in composites.," *International Journal of Solids and Structures*, vol. 47, pp. 3447-346, 2010.
- [201] R. Olsson, G. Lampeas, B. Ravindran and F. Izerhab, "Dynamic testing on unidirectional NCFcomposite-A comparison of test methods.," in *In 10th International Conference on Composites Testing and Model Identification*, Lille, 2021.
- [202] E. Sadeghpour, Y. Guo, D. Chua and V. P. Shim, "A modified Mori–Tanaka approach incorporating filler-matrix interface failure to model graphene/polymer nanocomposites.," *International Journal of Mechanical Sciences*, vol. 105699, p. 180, 2020.
- [203] Y. L. Li, C. P. Kohar, R. K. Mishra and K. Inal, "A new crystal plasticity constitutive model for simulating precipitation-hardenable al alloys.," *International Journal of Plasticity*, vol. 102759, p. 132, 2020.
- [204] A. Jain, "Micro and mesomechanics of fibre reinforced composites using mean field homogenization formulations: A review.," *Materials Today Communications.*, vol. 100552, p. 21, 2019.
- [205] H. M. Sertse, "Micromechanics based failure analysis of heterogeneous materials," Doctoral dissertation, Purdue University, 2017.
- [206] X. Liu, T. Tang, W. Yu and R. B. Pipes, " Multiscale modeling of viscoelastic behaviors of textile composites.," *International Journal of Engineering Science*, vol. 130, pp. 175-186, 2018.
- [207] Y. Zeng, "Mechanical characterization and computational modeling of snap-cure epoxy.," MASc Thesis, University of Waterloo, Waterloo, 2020.

Appendix A

Rouf, K., Suratkar, A., Imbert-Boyd, J., Wood, J., Worswick, M., & Montesano, J. (2021). Effect of strain rate on the transverse tension and compression behavior of a unidirectional non-crimp fabric carbon fiber/snap-cure epoxy composite. *Materials*, *14*(23), 7314.

“Accessible through the link below as well as the University of Waterloo’s Institutional Repository (UW Space)”

<https://www.mdpi.com/1996-1944/14/23/7314>

Appendix B

Rouf, K., Worswick, M., & Montesano, J. (2023). Effect of strain rate on the in-plane mechanical response of a unidirectional non-crimp fabric carbon fiber/snap-cure epoxy composite. Manuscript submitted (under review).

“Accessible through the University of Waterloo’s Institutional Repository (UW Space)”

Appendix C

Rouf, K., Worswick, M. J., & Montesano, J. (2021). A multiscale framework for predicting the mechanical properties of unidirectional non-crimp fabric composites with manufacturing induced defects. *Journal of Composite Materials*, 55(6), 741-757.

“Accessible through the link below as well as the University of Waterloo’s Institutional Repository (UW Space)”

<https://journals.sagepub.com/doi/pdf/10.1177/0021998320958189>

Appendix D

Rouf, K., Worswick, M. J., & Montesano, J. (2023). Experimentally verified dual-scale modelling framework for predicting the strain rate-dependent nonlinear anisotropic deformation response of unidirectional non-crimp fabric composites. *Composite Structures*, 303, 116384.

“Accessible through the link below as well as the University of Waterloo’s Institutional Repository (UW Space)”

<https://www.sciencedirect.com/science/article/pii/S0263822322011163>

Appendix E

Rouf, K., Worswick, M., & Montesano, J. (2023). An invariant-based constitutive model to capture the non-linear strain rate-dependent deformation response of fiber-reinforced composite materials: formulation and finite element implementation. Manuscript submitted (under review).

“Accessible through the University of Waterloo’s Institutional Repository (UW Space)”

Appendix F

Letter of Copyrights Permission

In accordance with the author rights policy of Elsevier, Sage and MDPI, individuals retain the right to include their article in a thesis/dissertation without the need for prior formal request. In the preparation of Chapter 3 and 4, the following journals/book chapter have been referred to as the original source, either in their entirety or in parts.

Rouf, K., Suratkar, A., Imbert-Boyd, J., Wood, J., Worswick, M., & Montesano, J. (2021). Effect of strain rate on the transverse tension and compression behavior of a unidirectional non-crimp fabric carbon fiber/snap-cure epoxy composite. *Materials*, 14(23), 7314.

Rouf, K., Worswick, M., & Montesano, J. (2023). Effect of strain rate on the in-plane mechanical response of a uni-directional non-crimp fabric carbon fiber/snap-cure epoxy composite. Manuscript submitted (under review).

Rouf, K., Worswick, M. J., & Montesano, J. (2021). A multiscale framework for predicting the mechanical properties of unidirectional non-crimp fabric composites with manufacturing induced defects. *Journal of Composite Materials*, 55(6), 741-757.

Rouf, K., Worswick, M. J., & Montesano, J. (2023). Experimentally verified dual-scale modelling framework for predicting the strain rate-dependent nonlinear anisotropic deformation response of unidirectional non-crimp fabric composites. *Composite Structures*, 303, 116384.

Rouf, K., Worswick, M., & Montesano, J. (2023). An invariant-based constitutive model to capture the non-linear strain rate-dependent deformation response of fiber-reinforced composite materials: formulation and finite element implementation. Manuscript submitted (under review).

Copyright permission has been duly granted for the following materials along with their respective right holders. The agreements have been established between the University of Waterloo (represented by Khizar Rouf) and the respective right holders, each assigned with unique license numbers or by written approvals:

Figure	Right Holder	Reference	License Number	License Date
1-1	International Council on Clean Transportation	"The international council on clean transportation " Global PV figure data 20200527, 27 May 2020. [Online]. Available: https://theicct.org/file/global-pv-figure-data-20200527xlsx-0 . [Accessed 25 November 2020].	By e-mail	2021-08-16
1-2	BMW Group	H. Mason, "Composites end markets: Automotive (2023)," 29 12 2022. [Online]. Available: https://www.compositesworld.com/articles/composites-end-markets-automotive-2023 . [Accessed 09 07 2023].	By e-mail	2023-07-17
2-1	Alberto Trejo	E. A. Trejo Sandoval, "Characterizing the deformation response of a unidirectional non-crimp fabric for the development of computational draping simulation models," MSc Thesis, University of Waterloo, Waterloo, 2020.	By e-mail	2023-07-09
2-2	MDPI	R. W. Kim, C. M. Kim, K. H. Hwang and S. R. Kim, "Embedded based real-time monitoring in the high-pressure resin transfer molding process for CFRP.," <i>Applied Sciences</i> , vol. 9, no. 9, p. 1795, 2019.	By e-mail	2023-07-10
2-4	Yu Zeng	Y. Zeng, "Mechanical Characterization and Computational Modeling of Snap-cure Epoxy.," MSc Thesis, University of Waterloo, 2020.	By e-mail	2023-07-09
2-5 a	Elsvier	Gilat, A., Goldberg, R. K., & Roberts, G. D. (2002). Experimental study of strain-rate-dependent behavior of carbon/epoxy composite. <i>Composites Science and Technology</i> , 62(10-11), 1469-1476.	1379459-1	
2-5 b	Elsvier	Koerber, H., Xavier, J., & Camanho, P. P. (2010). High strain rate characterisation of unidirectional carbon-epoxy IM7-8552 in transverse compression and in-plane shear using digital image correlation. <i>Mechanics of Materials</i> , 42(11), 1004-1019.	5584900763411	2023-07-09
2-5 c	Elsvier	Koerber, H., Xavier, J., & Camanho, P. P. (2010). High strain rate characterisation of unidirectional carbon-epoxy IM7-8552 in transverse compression and in-plane shear using	1379461-1	

		digital image correlation. <i>Mechanics of Materials</i> , 42(11), 1004-1019.		
2-6 a, b, c	Elsvier	Koerber, H., & Camanho, P. P. (2011). High strain rate characterisation of unidirectional carbon–epoxy IM7-8552 in longitudinal compression. <i>Composites Part A: Applied Science and Manufacturing</i> , 42(5), 462-470.	5584901107603	2023-07-09
2-8 a	eFunda engineering fundamentals	"Macromechanics of lamina," [Online]. Available: https://www.efunda.com/formulae/solid_mechanics/composites/comp_lamina_principal.cfm . [Accessed 10 05 2021].	By e-mail	2023-07-09
2-10	Cambridge University Presse	R. Talreja and C. V. Singh, Damage and failure of composite materials., Cambridge University Press, 2012.	84273	2023-07-09